Satellite Microwave Observations of Polar Lows

by
John M. Forsythe

Department of Atmospheric Science
Colorado State University
Fort Collins, Colorado

Colorado State University

Department of Atmospheric Science

Paper No. 525

SATELLITE MICROWAVE OBSERVATIONS OF POLAR LOWS

by

John M. Forsythe

Department of Atmospheric Science and the
Cooperative Institute for Research in the Atmosphere
Colorado State University
Fort Collins, Colorado 80523

Spring, 1993

Atmospheric Science Paper No. 525
CIRA Report No. 0737-5352-28

Research Supported by
NOAA Grant 90RAH00077

This paper was also submitted in partial fulfillment of the
requirements for the Degree of Master of Science.

ABSTRACT

Satellite microwave measurements of surface wind speed from the Special Sensor Microwave/Imager (SSM/I) and brightness temperature measurements from the Microwave Sounding Unit (MSU) are examined for four polar low cases. Polar lows span a variety of structures and often share features in common with tropical cyclones, such as the presence of a clear eye and a warm central core. Studies of tropical cyclones with the MSU have shown the presence of a warm core over the storm. This has been related to central pressure deficit and the wind field. This study explores the application of similar techniques to polar lows.

Isolated warm cores are found in two of the four polar lows studied. Warming of up to 3 K is noted. The possibility of effects other than temperature change in the air column as a cause for the brightness temperature changes is examined. Based on previous studies of cloud and precipitation effects at these frequencies, it is concluded that they can account for warming of up to 1 K. This leaves warming of up to 2 K over some of the polar lows. This is evidence that some polar lows do possess a warm core structure which can be detected by satellite. The warming is most pronounced over polar lows with well defined cloud bands.

Surface wind speed measurements from the SSM/I appear to resolve the wind field of the polar lows with less interference from precipitation than for tropical cyclones. The wind speed measurements are used to infer the central pressure of the polar lows. MSU brightness temperature anomalies are compared to the inferred pressure deficits, with little correlation noted. Sources of error in this comparison include poor fit of the wind model, storm asymmetry, and the possibility that the inner and outer circulation of the polar lows are decoupled.

The conclusion from this study is that satellite microwave observations of polar lows provide valuable information about these storms of the polar regions. The MSU

can resolve warming over the center of some polar lows and the SSM/I can detect the outer circulation. In the future, more observations of polar lows are needed to validate the satellite measurements and to allow for modelling of the effect of polar lows on microwave radiative transfer.

ACKNOWLEDGEMENTS

I would first like thank to thank my advisor, Professor Thomas Vonder Haar, for his guidance and support during this study. His assistance with my attendance at the 72nd Annual American Meteorological Society Meeting and the Workshop on Applications of New Forms of Satellite Data to Polar Lows Research is most appreciated. I would also like to thank my committee members, Professors William Gray and David Krueger. All were generous with their time and interest in this research.

Special thanks are extended to Professor Erik Rasmussen of the University of Copenhagen, Denmark. Professor Rasmussen sparked my interest in polar lows while he was a visiting scientist at the Cooperative Institute for Research in the Atmosphere (CIRA) in 1991. I had many valuable discussions with him regarding polar lows and I am grateful for his support which allowed me to attend the Polar Low Workshop in June, 1992.

Andy Jones was most generous with his time in introducing me to the computing facilities at CIRA. He was always helpful when it came to answering questions. Thanks are extended to Andy for allowing me to use his PORTAL system to process the satellite data.

Nan McClurg and Kelly Dean were both very helpful with questions I had about the computer system at CIRA. Deb Lubich graciously assisted me with obtaining MSU data and helped me process the data. The help of Joanne DiVico and Loretta Wilson in assistance with numerous logistical aspects of this research is greatly appreciated.

Thanks go to the NOAA / RAMM branch at CIRA for providing me with access to SSM/I and MSU data and to the National Snow and Ice Data Center for DMSP infrared imagery.

This work was supported by the National Oceanic and Atmospheric Administration under NOAA grant 90RAH00077.

TABLE OF CONTENTS

LIST OF TABLES

LIST OF FIGURES

Chapter 1

INTRODUCTION

Satellite remote sensing in the microwave portion of the spectrum has numerous applications in atmospheric science. These applications have steadily expanded since the first earth looking microwave radiometer was launched on the Soviet Cosmos 243 satellite in 1968. Among the atmospheric properties which can be remotely sensed using microwave techniques are temperature and water vapor profiles, surface wind speed, cloud liquid water, and precipitating clouds. Surface properties which have important effects on the atmosphere and can be sensed with microwave methods are soil moisture, snow cover, sea surface temperature, and sea ice.

The polar regions and the oceans suffer from a paucity of *in situ* observational data. Weather analysis and forecasting in the polar regions has benefitted greatly through the use of infrared satellite imagery from polar orbiting satellites. Such observations give a detailed view of cloud patterns but do not give more quantitative information on the conditions within and below the clouds. In the polar regions, such lack of data can cause dangerous storms to go undetected. There is a long history of accidents involving small fishing boats in the northern oceans (Businger and Reed, 1989a). A type of storm known as a polar low gives an example of the difficulties of forecasting in the polar regions. Physical characteristics of polar lows which can be retrieved from satellite data would be very useful to forecasters. Research into the characteristics of polar lows and factors affecting their genesis would be aided by better observations of these storms, and satellites seem to be the most efficient way to obtain such data in the polar regions. In addition, polar lows

may play important roles in the transfer of heat between the ocean and atmosphere and in the formation of deep ocean water.

1.1 Research Objective

This study will examine polar lows using microwave remote sensing of surface wind speed and tropospheric mean column temperature. Remote sensing of these parameters has previously been applied in studies of tropical cyclones. Polar lows have often been compared to tropical cyclones (Rasmussen (1989); Emanuel and Rotunno (1989)) due to their similar appearance in satellite imagery and formation over water. Whether the apparent similarity can be extended beyond appearance to the dynamics of each system raises some intriguing questions. In particular, the question of whether some polar lows are warm core systems, like the tropical cyclone, has been raised both on theoretical and observational grounds. Previous work on tropical cyclones with microwave techniques similar to those used in this study has revealed a strong relationship between the satellite measured warm core and central pressure and maximum winds (*e.g.* Velden, 1989; Kidder *et al.*, 1980). In this study, Microwave Sounding Unit (MSU) data from the *NOAA-10* and *NOAA-11* satellites will be examined for the presence of a warm core around four polar lows, with consideration being given to cloud and precipitation effects which could interfere with the warming signal. Warm cores which are detected will be compared to surface wind speeds at outer radii, these being determined from measurements of the Special Sensor Microwave Imager (SSM/I) on board the Defense Meteorological Satellite Program (DMSP) F8 satellite, in order see if a relationship can be found. Such a relationship, if it exists, would be of great use for research and analysis of polar lows.

1.2 Previous Satellite Microwave Observations of Temperature and Wind Speed in Storms

This study, which explores how remotely sensed microwave parameters may aid in the understanding of polar lows, was inspired by previous studies which used microwave techniques to examine tropical cyclones. A review of these techniques and their results will be given in order to examine their applicability to polar low research.

An early exploration into the utility of satellite microwave data for remote sensing of tropical cyclones was performed by Rosenkranz *et al.* (1976). Using the Scanning Microwave Spectrometer (SCAMS), brightness temperature measurements at 55.45 GHz over a tropical cyclone revealed the presence of a warm core of approximately 4 K amplitude. They also retrieved other parameters such as surface wind speed around the storm by using the 22.23 and 31.65 GHz channels of the SCAMS. In further work on the same storm, Grody *et al.* (1979) used 55.45 GHz brightness temperature measurements to retrieve midtropospheric tangential wind speed through thermal wind considerations.

A case study of Hurricane David by Grody and Shen (1982) examined the influence of this storm on each MSU channel. A result of significance for this study was that 53.74 GHz measurements showed contamination as a result of precipitation. At 53.74 GHz, brightness temperature decreases up to 5 K were measured over the hurricane in areas of heavy precipitation. The horizontal resolution of the MSU measurements was from between 100 and 200 km. This channel was shown to respond to the warm core of the hurricane despite the decreases in the warm anomaly caused by precipitation. The strongest response to the warm core was from 54.96 GHz measurements of the MSU, a frequency which receives most of its temperature signal from near 250 mb, which is close to the average level of maximum temperature anomaly in a tropical cyclone.

Kidder *et al.* (1978) applied the response of the SCAMS upper tropospheric temperature sounding channel to the warm anomaly of the tropical cyclone in order to estimate tropical cyclone central pressure and in turn outer radii wind speeds. The heart of the method was a linear regression between 55.45 GHz brightness temperature anomaly and central pressure as determined from aircraft measurements. Their regression relationship is shown in Figure 1.1. Note the high correlation coefficient of -0.859 for this relationship.

In continuing work with this method, Kidder *et al.* (1980) continued to explore the relationship between 55.45 GHz brightness temperature anomaly and surface pressure anomaly in tropical cyclones. They used mean temperature anomaly profiles developed from composites of tropical cyclones and a radiative transfer model to develop a relationship between brightness temperature anomaly and central pressure anomaly. The outer wind field could then be deduced through the gradient wind relationship. Their results indicated that radii of gale and storm force winds could be determined to within about 80 km.

Velden and Smith (1983) used the higher resolution Microwave Sounding Unit in a refinement of previous work with the SCAMS instrument. They also produced temperature profiles from the four microwave temperature sounding channels to allow them to examine temperature anomalies at the 250 mb level, near the average level of greatest temperature anomaly in a tropical cyclone. Their results showed the expected high correlation of high temperature anomaly with lower central pressure and higher maximum wind speed for three cases.

Velden (1989) and Velden *et al.* (1991) continued examination of the microwave derived temperature anomaly versus tropical cyclone parameters for Atlantic and Pacific storms. Plots of MSU derived 250 mb temperature anomaly versus surface pressure anomaly and maximum wind speed for North Atlantic tropical cyclones are given in Figure 1.2. The effect of stratifying the results by latitude, eye

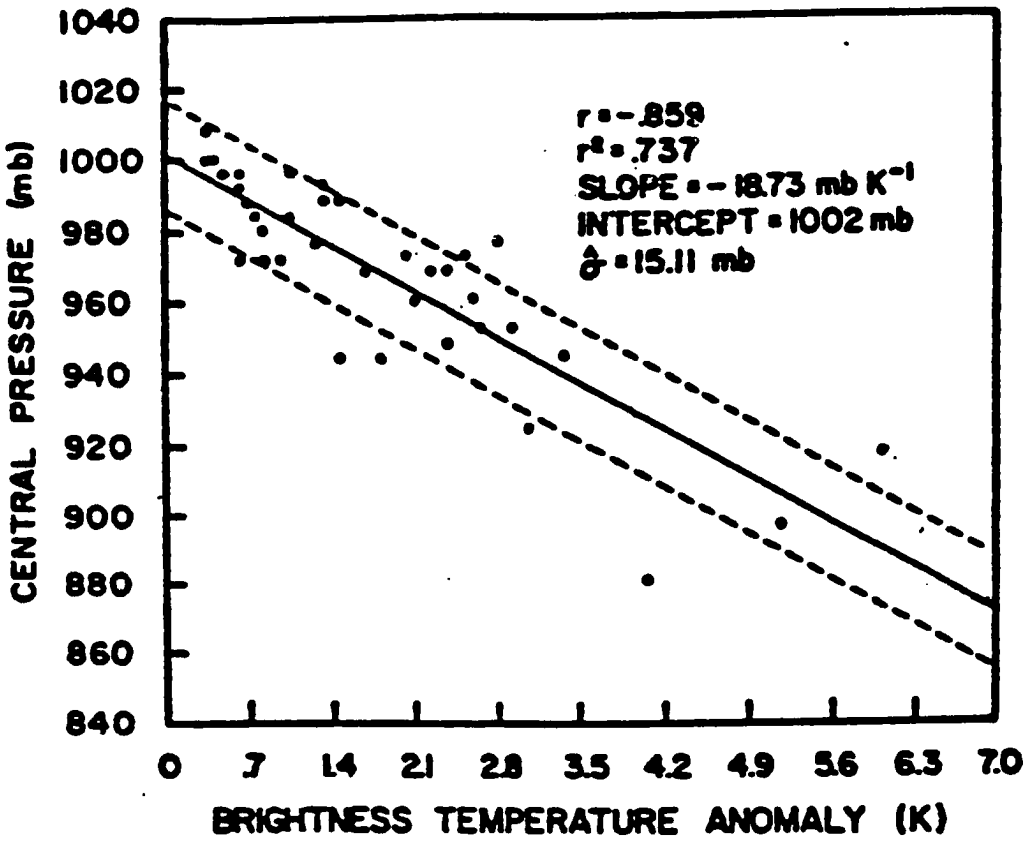

Figure 1.1: Central pressure of 36 tropical cyclones versus SCAMS 55.45 GHz temperature anomalies. The best fit linear regression and statistics are listed (from Kidder *et al.*, 1978).

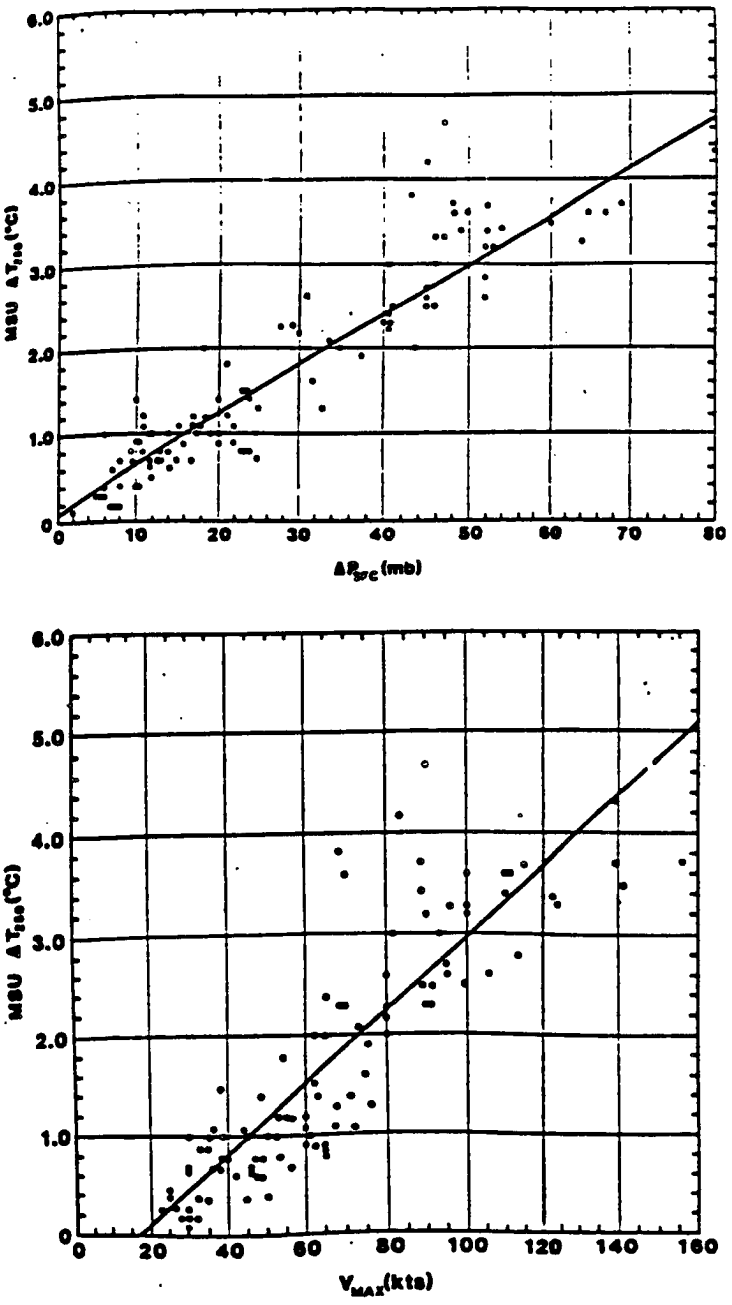

Figure 1.2: Top: MSU temperature anomaly at 250 mb versus surface pressure deficit. Bottom: MSU temperature anomaly at 250 mb versus maximum wind speed for North Atlantic tropical cyclones (from Velden, 1989).

size, and intensity tendency were discussed, with some improvements possible by including these considerations. Weakening storms were not always accompanied by a decrease in the warm core anomaly. This is due to the resolution limitation (100 to 200 km) of the MSU along with changes in the horizontal scale of the warming, as a large area of weak temperature anomaly could have the same effect on the remotely sensed temperatures as a small area with a strong temperature anomaly.

In an application of SSM/I data to tropical cyclones, Rappaport and Black (1989) applied SSM/I products to Hurricane Gilbert in an exploratory study. They noted that large areas of precipitation interfered with the ability of the SSM/I to resolve the wind field, particularly over the inner portion of the storm. As of the summer of 1992, SSM/I wind speed measurements were being used operationally by hurricane forecasters to aid in the determination of the radius of gale force wind around tropical systems.

Warming apparent in the 54.96 GHz channel of the MSU has been examined with respect to extratropical cyclogenesis in the North Atlantic (Velden, 1992). Preliminary results indicate that warming observed at this frequency, which has most of its signal from the upper troposphere, can be correlated with central pressure. Tropopause folding is a possible explanation for the warming observed with the MSU. Polar lows may have more than satellite signatures in common with rapidly deepening extratropical cyclones. According to Businger (1985), deep convection occurring at the time of most rapid deepening may be a common element for polar lows, comma clouds, and midlatitude cyclones.

The summary of results in this section indicate that satellite microwave measurements can be useful tools for diagnosing tropical storms and possibly midlatitude cyclones as well. Polar lows are another type of storm for which microwave measurements may hold promise. Previous work on polar lows with microwave measurements will now be discussed.

1.3 Previous Microwave Observations of Polar Lows with Satellites

Early investigations of polar lows with satellite data utilized infrared imagery from polar orbiting satellites (*e.g.* Forbes and Lottes, 1985). More recent studies at microwave frequencies have examined the temperature structure and surface wind speed structure for selected cases.

1.3.1 Satellite Temperature Soundings

The first study of a polar low using satellite soundings was performed by Steffensen and Rasmussen (1986). TOVS satellite sounding products, which employ the Microwave Sounding Unit as part of the retrieval, were used to examine the temperature structure of a polar low in the Norwegian Sea in December, 1981. Their interesting results showed a warm core at 500 and 850 mb. The TOVS temperature retrievals are shown in Figure 1.3. Warm cores were also seen at 850 and 500 mb at other times on the same day from other satellite overpasses. Steffensen and Rasmussen expressed hope for satellite sounder tracking of upper level cold pools which may be a precursor to polar low development.

In a study of an Antarctic subsynoptic-scale vortex, Warren and Turner (1989) noted the development of a 700 km scale mesoscale vortex in a baroclinic zone associated with decreasing 1000 to 500 mb thickness. They determined the thickness fields through satellite soundings, using an 80 km resolution inversion method. They speculated that the destabilization of the atmosphere associated with reduced thickness over the ocean was a key factor in the development of the mesoscale vortex.

Accurate satellite soundings in the polar regions are particularly difficult to obtain due to a number of factors. These include the presence of sea ice, low level temperature inversions, low clouds, and the difficult validation problem. Claud *et al.* (1992b) used a retrieval algorithm (the Improved Initialization Inversion - 3I) which has been specially modified for use in the polar regions. A major modification is the

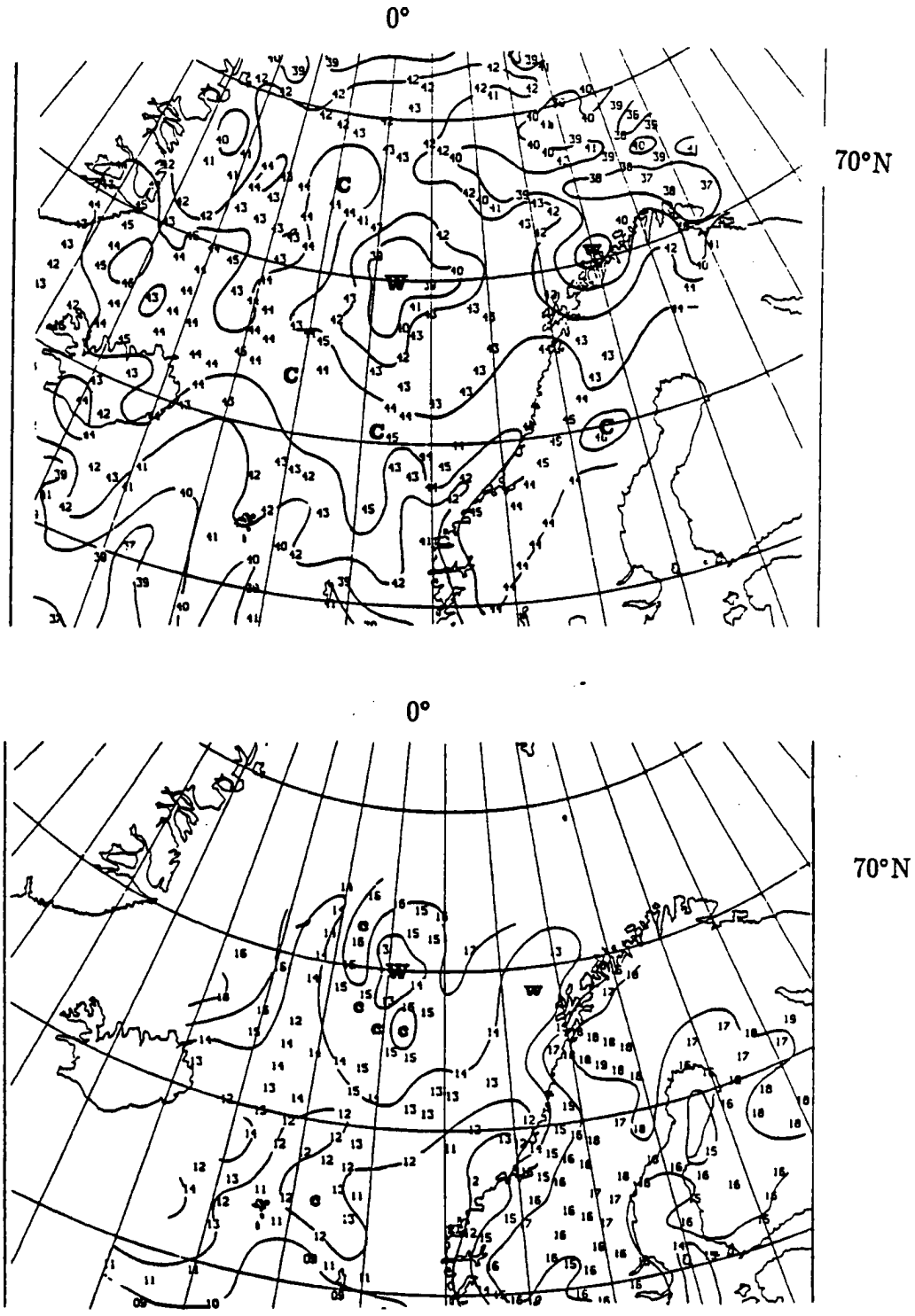

Figure 1.3: Top: 500 mb TOVS temperatures in negative degrees Celsius for December 11, 1981 0913 UTC . Note the warm area centered near 70° N, 0° W coincident with the location of a polar low. Bottom: 850 mb TOVS temperatures for the same date at 0317 UTC (from Steffensen and Rasmussen, 1986).

use of the MSU channels to determine the location of sea ice, which is radiatively similar to low clouds in the infrared channels. With the use of the 3I algorithm at 100 km resolution, the temperature of the lower stratosphere was determined. A polar low was located in a region of higher lower stratospheric temperatures. This implies a lowering of pressure at the surface. Whether this was a tropopause fold in the case of this polar low remains to be addressed. It is interesting to note in this regard that Shapiro *et al.* (1987) found a maximum of total columnar ozone, as deduced from the satellite-borne Total Ozone Mapping Spectrometer, over and west of a polar low.

Turner *et al.* (1992) used satellite soundings produced with the International TOVS processing package to compare satellite derived fields of temperature around a polar low with aircraft observations from Shapiro *et al.* (1987). None of the high resolution aircraft observations were used as a first guess in the retrieval. The results indicated that significant mesoscale detail could be obtained from the satellite soundings as compared to synoptic observations. Around the polar low, satellite soundings detected a warm core in the 1000-500 mb thickness field, shown in Figure 1.4. The aircraft observations detected this warm area as well. This is important validation of the ability of satellite sounders to detect the warm core in a polar low. Turner *et al.* (1992) interpreted the warm core as the result of a seclusion process in which warm air is isolated in the center of the system as cold air wraps around the base. The TOVS temperature retrieval nearest the center was biased up to 7° C too cold below 850 mb as compared to the aircraft data. Turner *et al.* (1992) attributed the cold bias to strong surface heat fluxes which modified the lowest layers. The initial guess available to the inversion scheme did not have this low level surface heating and it is not surprising that the lowest sounding channels could not detect it. They also speculated that cloud clearing in partly cloudy areas may not have been effective. Features in the satellite soundings and aircraft were mislocated up to

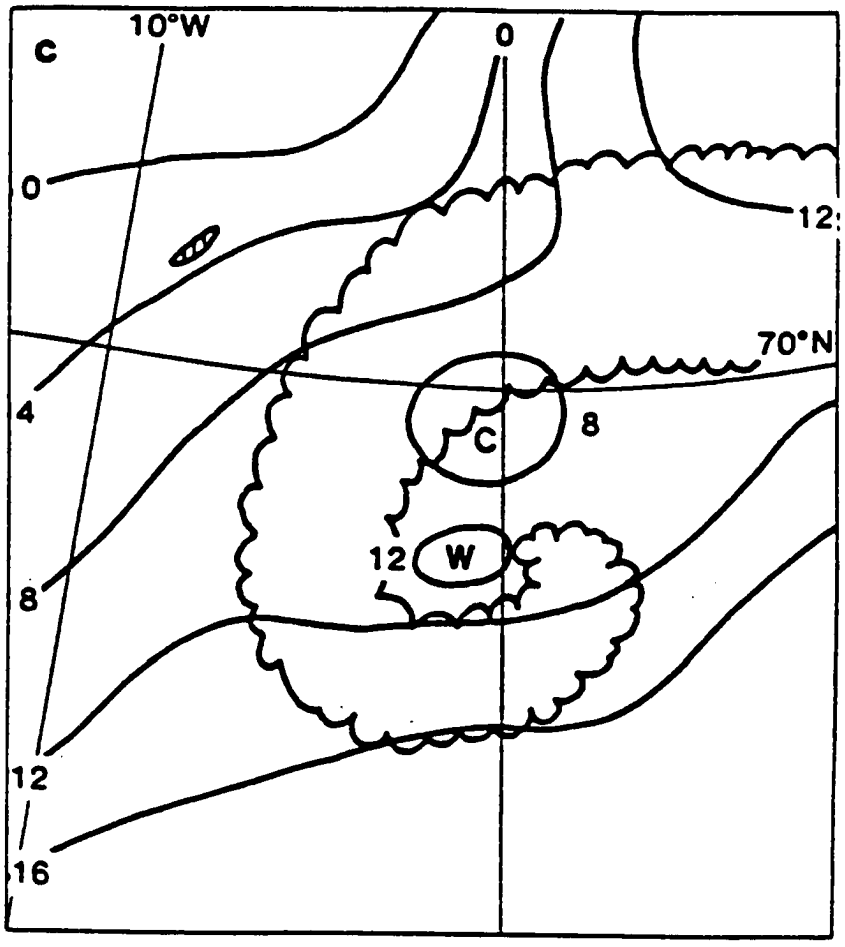

Figure 1.4: TOVS 1000-500 mb thickness fields (gpm/10 minus 500 m) at 40 m contours on February 27, 1984 at 1523 UTC around the polar low investigated by Shapiro *et al.* (1987). Note the warm seclusion in the clear area (from Turner *et al.*, 1992).

100 km. The lack of coincidence in location is not surprising in light of the greater than 100 km resolution of the MSU.

Of significance for this study, Turner *et al.* (1992) also examined fields of limb corrected MSU 53.74 GHz brightness temperatures around the polar low to assess the effect of cloud clearing. Their results did not show an isolated warm core in this data but they did show the effect of cloud clearing problems, as evidenced by cold temperatures in the satellite soundings with warmer temperatures in the microwave channels.

Satellite temperature soundings with the current NOAA satellites have demonstrated the ability to detect warm cores in some polar lows. This ability makes satellites an important tool for researching and possible monitoring and forecasting of polar lows.

1.3.2 Surface Wind Speed

Gloersen *et al.* (1989) was the first to use passive microwave radiometry to investigate surface wind speed and cloud liquid water around a polar low. Their algorithm used the 18 and 37 GHz frequencies of the Scanning Multichannel Microwave Radiometer (SMMR) and a regression against a limited tuning data set, which included wind observations from the polar low they were investigating. Their measurements were performed around a polar low which was investigated by aircraft (Shapiro *et al.*, 1987). The results showed that satellite microwave observations could be used to improve the detail in synoptic analyses and to interpolate between conventional wind speed observations.

Claud *et al.* (1991) were able to diagnose a sharp gradient in wind speed (from 5 to 25 m/s in 100 km) around a polar low in the Norwegian Sea. The strong gradient was validated by altimeter measurements of the GEOSAT satellite. Comparisons of SSM/I and GEOSAT wind speeds showed the SSM/I biased a few meters per second high as compared to the GEOSAT, although measurement time

differences of a few hours make the conclusions equivocable. Cloud liquid water amounts of 0.20kg/m^2 were returned over the clouds of the polar low with a well defined crescent shape present in the 85 GHz scattering index, which responds to deep convection (Petty and Katsaros, 1990).

A variety of parameters were derived by Claud *et al.* (1992a) from SSM/I and TOVS during a cold air outbreak and associated polar low. Surface wind speeds from the SSM/I were shown to agree well with synoptic analyses. They speculated on the effect that low level stability may have on the transfer of momentum from the atmosphere to the sea surface. Factors such as this may have the effect of decoupling the sea state from the wind speed. Cloud liquid water and the scattering index (Petty and Katsaros, 1990) from the 85 GHz channels gave an indication of the convective cloudiness associated with the polar low. The detection of a polar low is important because the determination of the existence of a polar low is a difficult forecasting problem, since polar lows are often unresolved by conventional observations. Integrated water vapor patterns were also derived from the SSM/I and compared to results obtained with TOVS through the 3I method, with similarities in large-scale features.

Rasmussen *et al.* (1992) investigated surface wind speeds around the much studied "Bear Island" polar low of 1982 using a two channel 37 GHz algorithm which they developed for the SMMR. Only the 37 GHz channels were used in their method in order to achieve the best possible resolution. Their results showed an area of gale-force winds in the same location where cloud streets in infrared satellite imagery suggested a cold air outbreak.

In summary, microwave remote sensing of polar lows is in its infancy. A number of case studies, including some new data presented in this paper, have revealed the utility of satellite microwave observations of polar lows. This is in spite of the horizontal resolution limitations of current satellite microwave instruments.

The application of new forms of satellite data to polar low research was the theme of a meeting of the European Polar Lows Working Group which was held in June, 1992 in Hvanneyri, Iceland (Rasmussen *et al.* (1993)).

Chapter 2

CHARACTERISTICS OF POLAR LOWS

The atmospheric disturbances which we now call polar lows have only become an object of study in their own right in the last 25 years. For years forecasters were aware of violent storms which developed suddenly in the polar regions. These small scale storms were difficult to detect and forecast due to their size, typical life cycle of two days or less, and occurrence in data sparse regions. Meteorological satellites have led to a better understanding of high latitude meteorology and better early detection of polar lows. For the forecaster, polar lows are still unresolved by operational models (Businger and Reed, 1989a), but the large scale environment which is conducive to polar low formation can be diagnosed by the models. There is still much to be learned about these storms and many of the basic issues regarding polar lows, such as the definition and how the dynamics operate, are still being discussed. Polar low formation and intensification has been discussed in terms of varying degrees of baroclinic and diabatic processes, with a spectrum of intermediate types possible (Craig and Cho, 1989).

2.1 Definition of a Polar Low

Businger (1985) lists the following typical characteristics of polar lows in the Norwegian Sea region, an area where polar lows have been extensively studied:

- Generally asymmetrical spiral cloud pattern
- Generally limited to the winter half of the year
- Dimensions of 200 to 500 km

- Below average temperatures at 500 mb; atmosphere conditionally unstable
- Often accompanied by convective showers or thunderstorms
- Circulation strongest near the surface
- Form poleward of jet streams
- Form over open water and fill over land
- Often form near a low level baroclinic zone such as an ice edge

It is likely that these features are also common in the Labrador Sea region, the source for the cases in this study. In order to discuss polar lows it is necessary to define a polar low. The definition of a polar low periodically comes up for review (*e.g.* Rasmussen and Lystad, 1987). A difficulty with defining a polar low is that polar lows frequently transcend the categories, for instance starting as a mass of convective clouds and then assuming the structure of a baroclinic wave.

A definition widely used at the current time comes from Businger and Reed (1989b). They define a polar low as

> "Any type of small synoptic- or sub-synoptic scale cyclone that forms in a cold air mass poleward of major jet streams or frontal zones and whose main cloud mass is largely of convective origin."

Rasmussen (1989) has modified the above definition to read

> "A polar low is a small scale synoptic or subsynoptic scale cyclone that forms in the cold air mass poleward of the main baroclinic zone and/or major secondary fronts. It will often be of a convective nature but baroclinic effects may be important."

Other definitions of polar lows have been proposed which are more specialized and include only a portion of the polar lows covered by the above definitions. For instance, Businger and Baik (1991) define a type of polar low which they call an arctic hurricane as

> "A polar low with symmetric signature and threshold winds greater than 25 m/s, in which surface fluxes play the dominant role in the structure and sustenance of the mature storm."

The analogy between polar lows and tropical cyclones is frequently made due to several similarities between the two systems. For instance, Rasmussen (1986) notes a proposed definition which defines a polar low as a warm core vortex consisting of deep cumulonimbus clouds.

2.1.1 Types of Polar Lows

The issue of how polar lows are formed and what physical mechanisms are important for their formation has led to various classifications of polar low types which fall under the broad definition given by Businger and Reed (1989b). These types differ in the importance of baroclinicity and surface fluxes of latent and sensible heat. The discussion of the roles of baroclinicity and surface fluxes has been a central theme in polar low research since Harrold and Browning's (1969) research.

Businger and Reed (1989a) define three types of polar low:

1) Short-Wave / Jet-Streak Type: A large mesoscale to small synoptic-scale comma shaped cloud pattern that develops in regions of enhanced baroclinicity and positive vorticity advection aloft. They generally occur over the oceans (Figure 2.1).

2) Arctic-Front Type: Polar lows formed along the ice margin, where outflows occur from the ice over the relatively warmer ice free water. They dissipate when not over water (Figure 2.2).

3) Cold-Low Type: Convective spirals which occur in the inner cores of old occlusions without any low-level baroclinic features. They do not necessarily occur in the polar regions, for example a cold-low investigated by Rasmussen and Zick (1987) occurred in the Mediterranean Sea.

As noted above, combinations of the two types can occur, for instance when an upper level trough crosses the ice edge.

2.2 Observations of Polar Lows

Our understanding of polar lows has increased over the past twenty years through case studies of polar lows. These studies have recently included the first research aircraft measurements of a polar low in the Norwegian Sea (Shapiro *et al.*, 1987). Other aircraft observations of polar lows have been performed in the Gulf of Alaska (Douglas *et al.*, 1991) and on the east coast of Greenland (Douglas *et al.*, 1990). This current total of about a half dozen polar lows investigated by aircraft (Table 2.1) will no doubt increase with future efforts, but it underscores a basic problem in polar low research, that of a lack of high spatial and temporal resolution measurements. Tropical cyclones, with which polar lows are often compared, have

Date	Location	Reference
Jan. 17, 1982	Pacific	Businger and Hobbs (1987) (comma cld.)
Feb. 10, 1982	Pacific	Businger and Hobbs (1987) (comma cld.)
Feb. 27, 1984	Norwegian Sea	Shapiro *et al.* (1987)
Feb. 29, 1984	Norwegian Sea	Rabbe (1987)
Mar. 13, 1985	Gulf of Alaska	Businger and Walter (1988) (comma cld.)
Mar. 4, 1987	Gulf of Alaska	Douglas *et al.* (1991)
Mar. 5, 1987	Gulf of Alaska	Douglas *et al.* (1991)
Dec. 1, 1987	Gulf of Alaska	Bond and Shapiro (1991)
Dec. 1, 1987	Gulf of Alaska	Bond and Shapiro (1991)
Mar. 17, 1989	East of Greenland	Douglas *et al.* (1990)
Mar. 18, 1989	East of Greenland	Douglas *et al.* (1990)

Table 2.1: Polar lows investigated by aircraft as of December, 1992.

a much more extensive data base. For instance, Weatherford (1987) had access to 750 aircraft measurements of tropical cyclones for use in composite studies.

The aircraft observations of polar lows have shown the existence of a circulation which is strongest at low levels with the warmest air near the center of the storm. The size of the disturbances (outermost closed isobar) ranged up to about

400 km. A warm core observed by observed by aircraft, evidenced by increased thickness near the storm center, is shown in Figure 2.3. It had a magnitude of 5 K in the layer from 1013 to 580 mb. The cases investigated by aircraft had maximum winds of 20 to 35 m/s and pressure deficits of 5 to 20 mb. The radius of maximum winds was about 100 km from the center.

Many case studies based on conventional observations of polar lows have been carried out. These studies have also found the existence of a warm core, *e.g.* Businger and Baik (1991). Surface pressure anomalies associated with polar lows have ranged up to 20 mb. Up to 35 mm of precipitation was reported by with a polar low by Rabbe (1987). Polar lows may consist of an intense inner core with attendant strong convection through the entire troposphere. Rasmussen *et al.* (1992) have documented the existence of "arctic instability lows" in areas of preexisting circulation. These are of a scale of less than 100 km. Økland (1987) has also documented an intense inner core within a vortex of larger dimension. Deep convective clouds in polar lows have been observed to reach up above 500 mb, based on infrared temperatures measured from satellites (*e.g.* Rabbe (1987); Nordeng and Rasmussen (1992)).

2.3 A Conceptual Polar Low

Based on our knowledge of polar lows, it is possible to construct a conceptual account of polar low weather. Heavy snow squalls, lightning, and rising temperatures to near 0° C occur as the storm center approaches. Winds may gust from gale to hurricane force and spray from the sea may encrust any exposed object such as a ship, creating a very hazardous situation. The rapid increase in wind speed is characteristic of polar lows (Rabbe, 1987). As the center of the storm passes, surface temperatures reach a maximum, surface pressure reaches a minimum, and the winds are reduced to 5-10 m / s. The clouds may break up but soon the winds change direction 180° and the weather is poor again until the storm is past. The

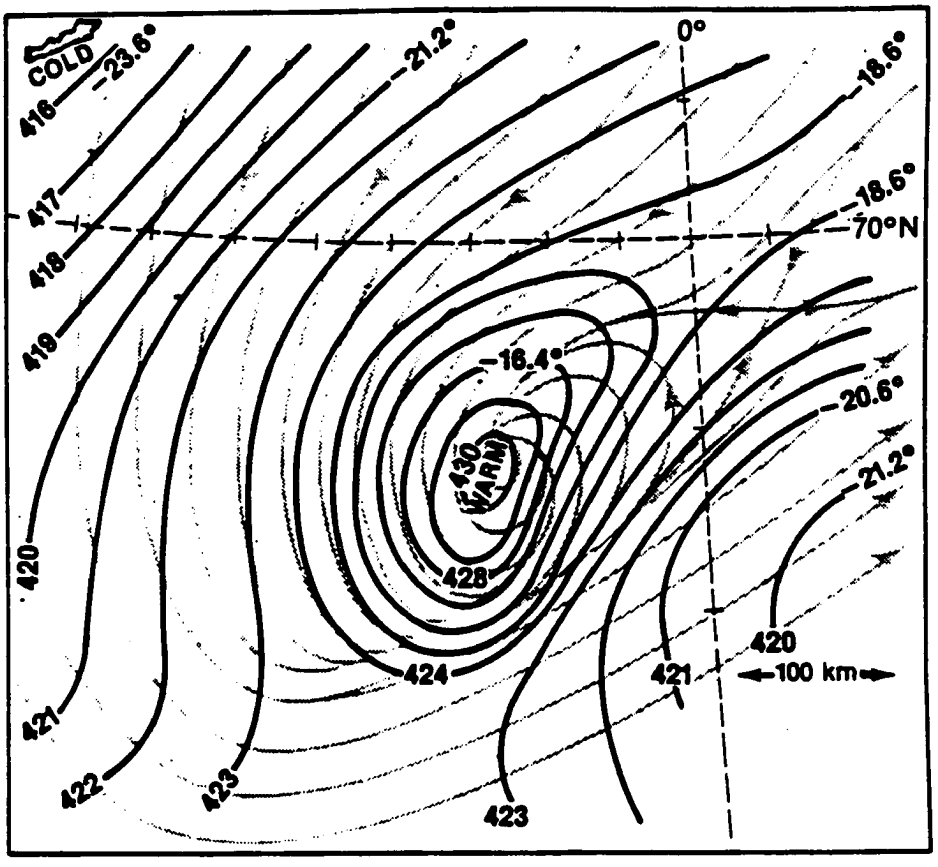

Figure 2.3: 1013 to 580 mb thickness contoured at 10 m intervals (heavy lines) with 956 mb streamlines (faint lines) for a polar low investigated by aircraft. Note the warm core of the polar low, as shown by the maximum in thickness near the polar low center (from Douglas and Shapiro, 1989).

entire storm may last on the order of six hours. Families of polar lows can occur, as documented by Rasmussen *et al.* (1992). Forecasting experience (Midtbø, 1986) has shown that polar lows often follow the steering winds in the 850-700 mb level.

A conceptual model of cloud pattern, streamlines, and temperature structure has been given by Douglas and Shapiro (1989) and is shown in Figure 2.4, along with an infrared satellite image of a polar low which fits the conceptual diagram. The degree of symmetry of the cloud bands of polar lows is quite variable, ranging from a comma shaped cloud shield to symmetric spirals which resemble tropical cyclones. Some polar lows have cloud free inner areas which can strikingly resemble the eye of a tropical cyclone (*e.g.* Rasmussen *et al.* (1992)), although whether the eye is caused by a descending eyewall circulation, as in a tropical cyclone, is not well established (Økland, 1989). An excellent review of polar lows is presented in Twitchell *et al.* (1989).

2.4 Climatological Occurrence of Polar Lows

Polar lows occur almost exclusively during the colder months of the year. Figure 2.4 shows histograms of polar low occurrence for regions near Norway and in the Bering Sea. Note the maxima in the winter months. Other preferred regions for polar low formation are the area east of Greenland and the Labrador Sea. Parker and Hudson (1991) present a climatology of polar low occurrence in Canadian waters.

Polar low occurrence in the Southern Hemisphere has been studied by Fitch and Carleton (1992). They point out the fact that although vortices similar to Northern Hemisphere polar lows exist in the Antarctic, a direct analogy is difficult due to a number of factors. These include the lack of occurrence of warm ocean water in close proximity to the sea ice boundary in the Antarctic, and the occurrence of katabatic winds in the Antarctic which may be involved in forcing mesoscale cyclogenesis.

2.5 Significance of a Warm Core in Polar Lows

As a portion of this study examines the ability of current satellite microwave sounding techniques to detect warm cores in polar lows, the implications of the presence of a warm core will be examined. Warm cores near the surface have been detailed in case studies of several polar lows using aircraft or conventional observations (*e.g.* Businger and Baik, (1991); Douglas *et al.*, (1991); Shapiro *et al.*, (1987); Rasmussen (1985)). As stated previously with respect to general characteristics of polar low occurrence, there are often below average temperatures at 500 mb when polar lows occur. Although polar lows may have a warm core near the surface, Douglas *et al.* (1991) state that layer thickness analyses such as from 1000 to 500 mb will not reveal the polar low structure because the layer consists of a shallow warm layer along with an upper layer of colder air. They state that satellite soundings do not have sufficient resolution to adequately describe the structure of the polar low. This statement is challenged by the work of Turner *et al.* (1992), which detailed the warm core of the polar low through satellite derived 1000 to 500 mb thickness fields. It is likely that the ability of satellite soundings to determine the thermal structure of a polar low is quite variable in light of the several types of polar lows previously discussed.

The mechanism responsible for the formation of warm cores in some polar lows has not been unequivocally determined, nor has the mechanism which initially forms polar lows. Subsidence, which is responsible for the strong warming in tropical cyclones, is not very effective in the polar atmosphere due to low water vapor mixing ratios in polar regions (Rasmussen, 1989), with warming possible only in the lowest layers. Theories for the development of a warm core have also included heating by cumulus convection or heating by strong sensible heat fluxes from the surface. These two theories are referred to as Conditional Instability of the Second Kind (CISK) and Air Sea Interaction Instability (ASII), respectively. It is likely that in individual

cases heating is caused by a combination of both processes (Van Delden, 1989a). In addition, the formation of a warm core in some polar lows by a seclusion process has been suggested (Shapiro *et al.* (1987); Turner *et al.* (1992)). Seclusion does not require diabatic heating but rather occurs as cold air wraps around the polar low and isolates warmer air near the center.

The seclusion process may be a feature which the polar low has in common with with some intense marine cyclones, also known as "bombs". Seclusion has been observed in high resolution modelling of an occluded marine cyclone which had a warm core (Kuo *et al.*, 1992). The warming noted in the marine cyclone did not occur from diabatic heating as in a tropical cyclone but rather formed as a result of warm but not tropical air from ahead of the low being pinched off by fast moving colder air. This warm core found in the marine cyclone formed in an entirely different manner than the warm core observed in the tropical cyclone. It is interesting to note that the seclusion process is only observed in ocean storms, with reduced surface friction possibly playing a role here (Kuo *et al.*, 1992). The warm cores observed in some polar lows may be the result of a combination of the processes discussed here.

The CISK hypothesis for polar lows was first put forward by Rasmussen (1979). CISK requires some type of preexisting disturbance for the feedback process to be initiated. It states that moisture convergence will enhance cumulus convection, which will then lower the ambient pressure through latent heating and increase the moisture convergence, leading to more upward motion and a positive feedback. The idea of CISK has been used to explain tropical cyclone intensification, where abundant moisture is available for latent heating. A criticism of the CISK hypothesis is that a reservoir of buoyant energy does not exist for convection to sustain itself (Emanuel and Rotunno, 1989), and therefore some additional surface energy input is needed. Craig and Cho (1988) note that the presence of a warm core in a polar low does not necessarily imply CISK.

The Air Sea Interaction Instability (ASII) theory (Emanuel and Rotunno, 1989) supplies the required energy input through strong surface fluxes of sensible and latent heat. These fluxes are present in the polar low environment due to strong winds and large temperature contrasts between the ocean surface and the boundary layer air, conditions which are presumably supplied by some initial disturbance. These surface fluxes lead to falling surface pressure and increased surface winds, forming a positive feedback. The presence of strong surface fluxes around polar lows has been well documented (Businger and Baik, 1991; Shapiro *et al.*, 1987). Total heat fluxes of approximately 1000 W/m^2 have been observed, comparable to values in tropical cyclones, with Bowen ratios of 1 or greater. The great flux of sensible heat relative to latent heat is a key difference between the environment of the polar low and the tropical cyclone, which typically has a Bowen ratio of 0.1.

The ASII and CISK processes require some type of pre-existing disturbance before they become active, for instance baroclinic instability or topographic forcing. It is also possible that the pressure field could adjust to some initial wind field in a manner which could develop a warm core. A warm core is postulated to form via the ASII process through the replacement the original cool column of air with warmer air from the surface. Sensible heat fluxes may contribute to the warming directly and also through destabilization of the lower layers, allowing convection and latent heating to occur over a deeper layer. Surface fluxes are the primary ingredient for in the ASII theory. The large temperature contrasts between the sea surface and the boundary layer air allow for strong sensible heat fluxes. Through use of an axisymmetric model designed for hurricanes, Emanuel and Rotunno (1989) were able to successfully simulate a polar low given a preexisting disturbance. The idea that polar lows may intensify through the ASII process has been supported by the modelling and observational work of Businger and Baik (1991). Their model determination of temperature deviation from the lateral boundary condition over

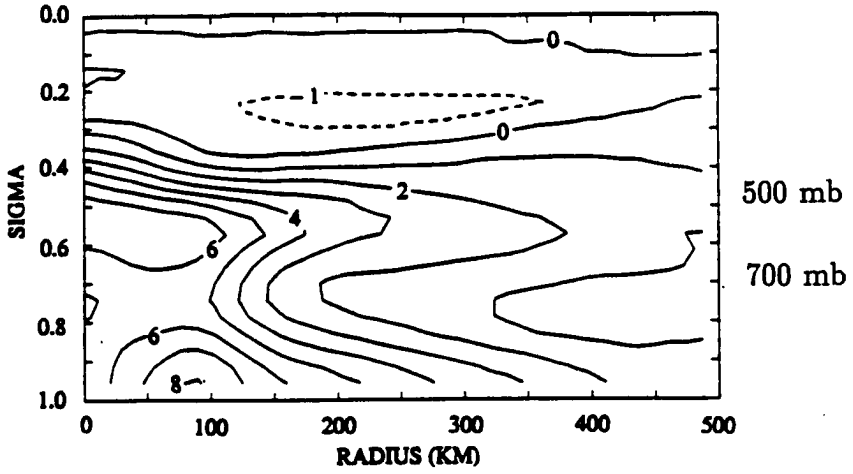

Figure 2.6: Cross section of temperature deviation from the model lateral boundary condition (contour interval 1° C) for a polar low (from Businger and Baik, 1991).

a mature polar low is shown in Figure 2.6. Note the warming near the center of the storm and the strong low level warming, due to sensible heat fluxes from the surface. This low level warming is not seen in tropical cyclone simulations.

The role of surface fluxes in rapidly intensifying marine cyclones has been investigated by (Kuo *et al.*, 1991). Modelling work revealed that strong surface fluxes are not necessary at the time of most rapid cyclone intensification. However, eliminating the surface fluxes in the period 24 hours before the most rapid deepening led to a reduced storm intensity. Apparently, surfaces fluxes of latent heat which occur before explosive development can be stored and released by the system at a later time. Surface sensible heat fluxes which occur before most rapid deepening can also aid the development at a later time through the formation of low level baroclinicity such as a coastal front. Surface fluxes can even become reversed and lead to weakening of the marine cyclone. Application of these results to polar lows is difficult due to the greater role of sensible heat and the shorter life cycle of the polar low as compared to the marine cyclone.

The effects of diabatic heating proportional to surface wind speed versus diabatic heating proportional to moisture convergence has been investigated numerically by Økland and Schyberg (1987). They note that sensible heating from the surface will occur at the same location as the corresponding flux while heating due to condensation can occur away from the source of the moisture. Their results showed that heating proportional to surface wind speed resulted in an area of downward motion at the center of the vortex, which may relate to the eyes observed in some polar lows, while heating proportional to moisture convergence led to intense upward motion at the center of the vortex. While the formation of an eye is a crucial step in the intensification of a tropical cyclone (Anthes, 1982), Rasmussen (1989) points out that the presence of a clear central area in a polar low does not necessarily imply that there are exceptionally low central pressures. Nordeng and Rasmussen (1992)

document a polar low with an exceptionally well-defined eye but a pressure deficit of only about 5 mb.

Økland (1987) has pointed out that heating by CISK is possible only if clouds in the central portion of the polar low are sufficiently deep, a typical value being tops at the 400 to 600 mb level. Deep clouds are more efficient at producing precipitation than shallow clouds and therefore would decrease the amount of evaporative cooling which is occurring. Heavy precipitation has been observed in the central areas of polar lows, as seen in Figure 2.7, where up to 35 mm was reported in a 12 hour period. Wilhelmsen (1986) examined 38 cases of gale producing lows near Norway and found a conditionally unstable lapse rate in the polar low environment in all cases. This is an indication that polar lows with strong winds are associated with deep convection.

Low level temperature inversions may also play a role in allowing deep convection to develop in the center of a polar low. Økland (1989) states that the presence of a low level inversion in the polar low environment allows air which has received strong surface fluxes to travel into the center to fuel deep precipitating convection, leading to the formation of a warm core. The lack of such an inversion is given as an explanation for the lack of polar low development in other cold air masses.

The development of a warm core in a polar low has been shown by Van Delden (1989a) to determine whether diabatic heating will cause intensification or weakening of the vortex. Intensification by diabatic heating can occur when the length scale of the heating is greater than the local Rossby radius of deformation. The presence of an initial circulation allows the Rossby radius of deformation to become smaller and allows balanced flow to occur on smaller scales. Van Delden (1989a) points out that a warm core cyclone has a greater deepening rate from diabatic heating than a cold core cyclone, which may fill under the effect of diabatic heating. The decreased inertial resistance to upper level outflow for a warm core

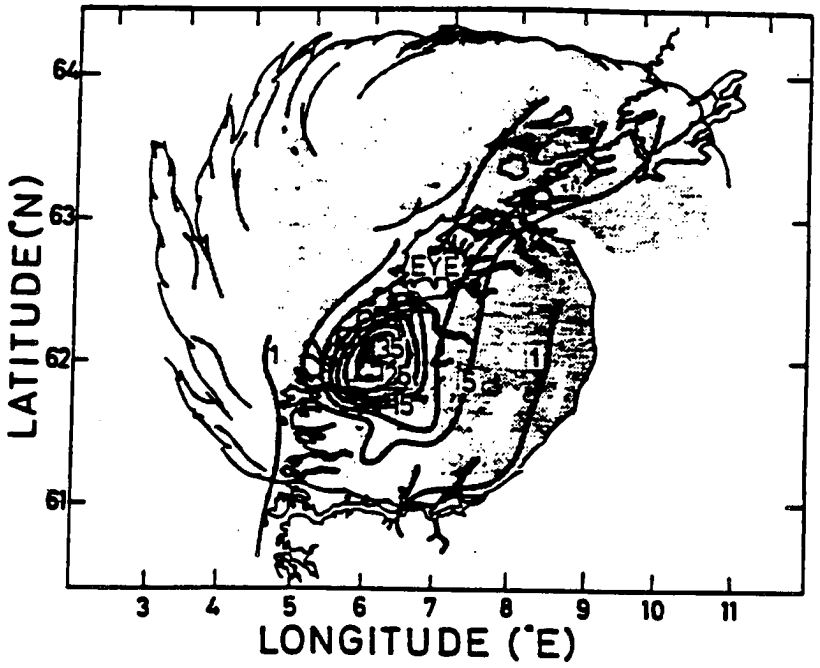

Figure 2.7: 12 hour precipitation totals (mm) from a polar low (from Rabbe, 1987).

cyclone is thought to be the reason for the enhanced deepening rates of the warm core system.

2.5.1 Relationship Between Temperature and Pressure Anomalies

Mean column temperature anomaly and surface pressure anomaly are related through the hydrostatic and ideal gas equations in the following form:

$$\Delta_P = P_{ENV}(1 - exp^{(\frac{gZ\Delta_T}{R\overline{T}^2})}) \tag{2.1}$$

where P_{ENV} is the environmental pressure, Δ_P is the pressure difference between the environment and an area whose mean column temperature differs by an amount Δ_T, g is the acceleration due to gravity, Z is the height of an undisturbed pressure level, R is the gas constant for dry air, and $\overline{T}$ is the average mean column temperature of the region. Δ_T is defined as positive when the area under consideration is warmer than the environment. The amount of pressure drop for one degree of mean column temperature increase is shown in Figure 2.8 as a function of a given height of a pressure surface which is undisturbed by the warming below. The amount of pressure decrease per degree of warming is also a function of the assumed mean temperature around the storm, shown as a family of lines for values from 230 K to 250 K (typical polar low and tropical cyclone mean column temperatures, respectively). The value ranges from 4 to 6 mb decrease per 1 K of mean column warming. For tropical cyclones, Velden and Smith (1983) report an approximate theoretical value of 5.5 mb per degree of warming while for polar lows Rasmussen *et al.* (1992) reports a value of 4 mb per degree of warming. This difference is due to the lower height of the tropopause in the polar atmosphere as well as different environmental temperatures.

As will be shown in section 4.2, The 53.74 GHz channel of the MSU is basically a measure of mean tropospheric temperature so temperature anomalies measured in this channel should be an indirect measure of pressure deficits over the storm in question. However, the resolution of the MSU is not high enough to resolve the

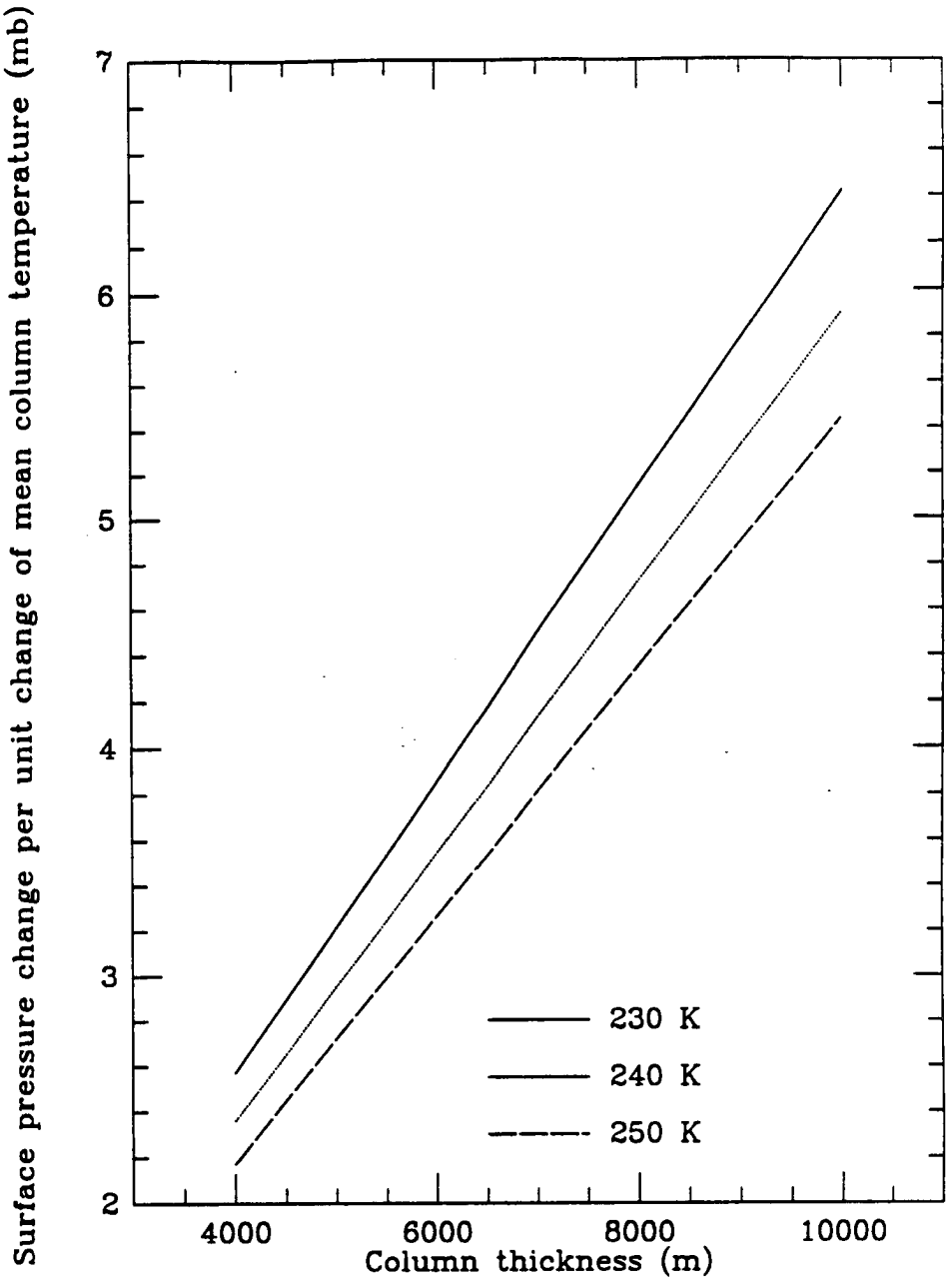

Figure 2.8: Hydrostatic pressure drop for a one degree increase in mean column temperature shown for mean column temperatures of 230, 240, and 250 K as a function of the depth of the layer which is being warmed.

strong warming in the eye and thus satellite techniques tend to underestimate the warming. Velden and Smith (1983) estimate that their temperature anomalies for tropical cyclones are too small by a factor of about 3. This is due to the poor resolution of the MSU, the shape of the weighting function versus the shape of the temperature anomaly with height, as well as the effects of precipitation in decreasing the brightness temperatures. The significance of satellite detected warm cores is that they indicate a pressure deficit associated with the polar low. This is important since infrared satellite imagery of a cloud spiral which resembles a polar low does not necessarily imply a surface circulation (Rasmussen, 1990). If a warm core is detected, it would be an indication of a pressure deficit associated with the storm.

We see that the question of whether a polar low has a warm core is important with respect to the issues of storm pressure deficit and deepening characteristics of the vortex. The remainder of this paper will examine principles of microwave remote sensing of temperature and wind speed and the application of these techniques to some polar lows.

Chapter 3

PASSIVE REMOTE SENSING WITH MICROWAVE RADIATION

3.1 Radiation at Microwave Frequencies

This study uses remotely sensed data in the microwave portion of the spectrum for the study of polar lows. This chapter will describe characteristics of microwave radiation and how microwave radiances at SSM/I and MSU frequencies are affected by various atmospheric parameters.

The microwave region of the spectrum is not firmly defined (Ulaby *et al.*, 1981), but a convention is that it extends from 0.3 to 300 GHz (1 mm to 1 m). In this study, thermal emission from O_2 molecules is used to infer mean tropospheric temperature. Thermal emission is described by the Planck function. The Planck function expresses radiance L_λ as a function of wavelength and temperature for a blackbody:

$$L_\lambda = \frac{2hc^2}{\lambda^5}\left(\frac{1}{e^{hc/\lambda kT} - 1}\right) \tag{3.1}$$

where h is Planck's constant, equal to 6.63 X 10$^-$34 J s, ν is the frequency, k is Boltzmann's constant of 1.38 x 10$^-$23 J/K, and T is the absolute temperature and λ is the wavelength. A blackbody is one that absorbs all incident radiation and emits at the maximum amount given by Planck's function. According to Kirchoff's Law, a body in local thermodynamic equilibrium is as good of an absorber as it is an emitter:

$$\alpha_\lambda = \epsilon_\lambda \tag{3.2}$$

where α_λ is the absorptance at some wavelength and ϵ_λ is the emittance at that wavelength. The Planck function can be replaced by simpler approximations for certain

portions of the spectrum. Fortunately, an approximation known as the Rayleigh-Jeans approximation works well for the low frequency part of the microwave spectrum employed in this study, where $h\nu/kT << 1$. For conditions where $\lambda T > 0.77$ m K, the Rayleigh-Jeans approximation can be used with an error of less than 1% (Ulaby *et al.*, 1986). Using the Rayleigh-Jeans approximation, the microwave radiance is linearly proportional to temperature:

$$L_\lambda = 2kc\lambda^{-4}T \tag{3.3}$$

A plot of the Planck Function and the Rayleigh-Jean's approximation is shown in Figure 3.1. The Rayleigh-Jeans approximation works well for the low frequency part of the microwave spectrum because radiance is nearly linearly proportional to frequency in this region, as can be seen in Figure 3.1. For some applications with the 85 GHz SSM/I frequencies, it is advisable to employ the full Planck function rather than the Rayleigh-Jeans approximation. This is because errors from using this approximation may exceed the instrument accuracy of 1.5 K (Jones and Vonder Haar, 1989).

In the microwave portion of the spectrum, radiance in Equation 3.3 can be divided by the terms multiplying the temperature and the resulting expression for temperature is called the brightness temperature. Brightness temperature is linearly proportional to radiance. The brightness temperature T_B of an object in thermodynamic equilibrium is related to the physical temperature T_S by the emissivity ϵ,

$$T_B(\nu, \theta, P) = \epsilon(\nu, \theta, P)T_S \tag{3.4}$$

where the frequency, polarization, and viewing angle dependence of emissivity is indicated by the terms ν, θ, and P.

The polarization of microwave radiation is defined according to two components of the electric field and their relationship to the plane of incidence. The

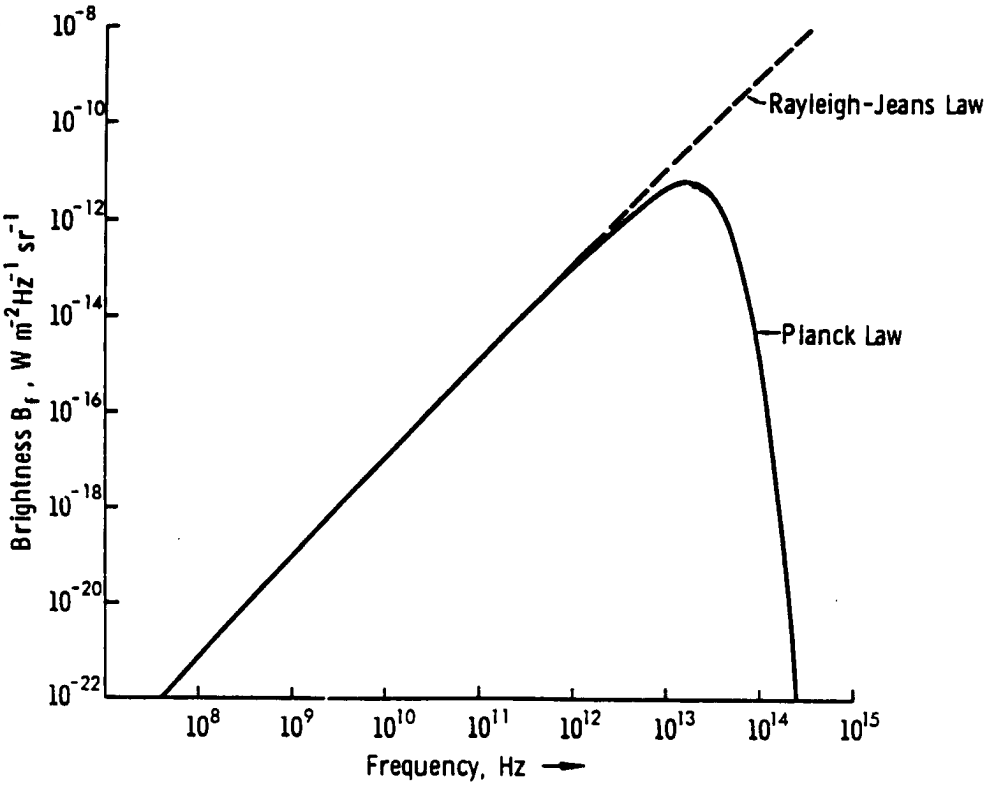

Figure 3.1: The Planck function and the Rayleigh-Jeans approximation (from Ulaby *et al.*, 1981).

plane of incidence of radiation is defined as the plane which contains the incident, reflected, and transmitted propagation vectors of electromagnetic radiation impinging on a surface. The vertically polarized component of the electric field lies in the plane of incidence of radiation while the horizontally polarized component is perpendicular to the plane of incidence.

3.1.1 Radiative Transfer

An understanding of microwave radiative transfer is necessary to interpret remotely sensed data. The radiance received at a satellite is a function of many surface and atmospheric variables. Since a part of this study examines the ability of the MSU to detect warm cores associated with polar lows, factors not related to temperature which could cause a warm core to be detected must be taken into account. These factors include water vapor content, both frozen and liquid clouds and precipitation, and changes at the surface. The effect of these processes is described by the radiative transfer equation. The general form of the radiative transfer equation will now be presented along with some more simplified forms.

It is necessary to first define a few terms which will appear in the radiative transfer equation. Volume coefficients for total extinction, absorption, and scattering are given by σ_e, σ_a, and σ_s, respectively. The extinction coefficient is the sum of the absorption and scattering coefficients:

$$\sigma_e = \sigma_a + \sigma_s \tag{3.5}$$

The single scatter albedo, ϖ, is defined as the ratio of energy lost by scattering to total energy lost:

$$\varpi = \frac{\sigma_s}{\sigma_e} \tag{3.6}$$

Another useful quantity is the optical thickness $\delta(r_1, r_2)$ between two points r_1 and r_2, defined as

$$\delta(r_1, r_2) = \int_{r_1}^{r_2} \sigma_e dr \tag{3.7}$$

and the transmittance between two points r_1 and r_2, τ, defined as

$$\tau(r_1, r_2) = e^{-\delta(r_1, r_2)} \tag{3.8}$$

The formal solution of the radiative transfer equation for the radiance at a point r is given by (Ulaby *et al.*, 1981)

$$L(r) = L(0)e^{\delta(0,r)} + \int_0^r \sigma_e(r')J(r')e^{-\delta(r',r)}dr' \tag{3.9}$$

Where $L(r)$ is the radiance at point r. Equation 3.9 says that the radiance received at a point r is the sum of that emanating from the the boundary ($r = 0$) plus the contribution from the material between point 0 and point r. The effective source function $J(r)$ is composed of an absorption source function J_a and a scattering source function J_s. The effective total source function is related to the individual source functions through the single scatter albedo (Ulaby *et al.*, 1981):

$$J = (1 - \varpi)J_a + \varpi J_s \tag{3.10}$$

The scattering source function may be replaced by a scattered radiometric temperature T_{SCAT} through the use of the Rayleigh-Jeans approximation and a scattering phase function. The scattering phase function weights the radiance incident from a direction into another direction. We can now replace the radiances by the blackbody equivalent radiometric temperature, T_{AP}, and the radiative transfer equation for propagation in a direction r may be written as (Ulaby *et al.*, 1981)

$$T_{AP}(r) = T_{AP}(0)e^{-\delta(0,r)} + \int_0^r \sigma_e(r') \left[(1 - \varpi)T(r') + \varpi T_{SCAT}(r')\right] e^{-\delta(r',r)}dr' \tag{3.11}$$

where $T(r')$ is the physical temperature at point r. This is a general form of the radiative transfer equation for an emitting surface and a scattering and emitting atmosphere. Some of the complexity in the radiative transfer equation stems from the fact that the scattered radiometric temperature is a function of the apparent

temperature at a point r, which is itself a function of the scattered radiometric temperature.

A simplification which can be made under some circumstances at microwave frequencies, such as clear skies, is that scattering is negligible. The effects of scattering and its occurrence at frequencies used in this study will be examined in a later section. If we assume no scattering the single scatter albedo ϖ is equal to zero and the radiative transfer equation takes the simplified form

$$T_{AP}(r) = T_{AP}(0)e^{-\delta(0,r)} + \int_0^r \sigma_a(r')T(r')e^{-\delta(r',r)}dr' \tag{3.12}$$

Note that the extinction coefficient has been replaced by the absorption coefficient.

A common practice in satellite meteorology is to employ plane parallel geometry to refer the vertical coordinate to a unit length. The distance along a path dr is related to the vertical depth dz by

$$dr = dz \sec\theta \tag{3.13}$$

where θ is the zenith angle, or the angle of incidence at the surface as measured from the vertical. Plane parallel geometry implies that the temperature and absorption coefficients are functions of height only.

As implied by 3.12, the apparent temperature sensed by a satellite for a scatter free atmosphere is the sum of a surface contribution and an atmospheric contribution. The upward emitted atmospheric component T_{UP} is given by

$$T_{UP}(\nu,\theta) = \sec\theta \int_0^\infty \sigma_a(z)T(z)e^{-\delta(z,\infty)\sec\theta}dz \tag{3.14}$$

Note that the integration can extend to ∞ for satellite applications since the absorption coefficients are equal to zero for free space.

The downward emitted component T_{DN} is given by the sum of downward atmospheric emission and cosmic background emission:

$$T_{DN}(\nu,\theta) = \sec\theta \int_0^\infty \sigma_a(z)T(z)e^{-\delta(0,z)\sec\theta}dz + T_{COS} \tag{3.15}$$

The cosmic background radiation T_{COS} has the constant value of 2.7 K and is independent of frequency and zenith angle at microwave frequencies used in this study (Ulaby *et al.*, 1981). The reflected sky component T_{SC} is given by the downward sky component T_{DN} weighted by some angular surface reflection distribution, which varies depending on surface roughness.

The blackbody equivalent temperature sensed by a satellite radiometer from a horizontally stratified atmosphere is given by the sum of atmospheric emission, surface emission, and surface reflection , with the two surface components depleted according to the transmittance of the intervening atmosphere:

$$T_{AP}(\nu,\theta,P) = T_{UP}(\nu,\theta,P) + \tau(0,\infty)\,[T_B(\nu,\theta,P) + T_{SC}(\nu,\theta,P)] \tag{3.16}$$

3.1.2 Surface Emittance and Reflectance

The surface components of the radiative transfer equation will now be discussed. Changes in these quantities are used to retrieve wind speed at the ocean surface and they can also present a source of noise to retrieval of other parameters such as sea surface temperature (Milman, 1987).

It is simplest to begin with a description of the reflectance and emittance for a specular surface (height variations small relative to wavelength). For example, a specular condition may describe a calm mirror-like sea. The specular reflectivities, the ratio of the amount of energy incident to the amount reflected, at horizontal or vertical polarization for an air / water interface are computed through the Fresnel formulae (Ulaby *et al.*, 1986):

$$\rho(\nu,\theta,h) = \left[\frac{\cos\theta - \sqrt{\epsilon_w - \sin^2\theta}}{\cos\theta + \sqrt{\epsilon_w - \sin^2\theta}}\right]^2 \tag{3.17}$$

$$\rho(\nu,\theta,v) = \left[\frac{\epsilon_w\cos\theta - \sqrt{\epsilon_w - \sin^2\theta}}{\epsilon_w\cos\theta + \sqrt{\epsilon_w - \sin^2\theta}}\right]^2 \tag{3.18}$$

where ϵ_w is the complex part of the dielectric constant of water.

Since microwaves penetrate sea water to only about 1 cm depth (Ulaby *et al.*, 1986), through energy conservation for a specular sea surface we approach the relation

$$\epsilon_{\nu,p} + \rho_{\nu,p} = 1 \tag{3.19}$$

Since the reflectivity at each polarization can be determined from 3.17 and 3.18, the brightness temperature of a given specular sea surface can be determined.

For a specular sea surface at a given frequency, 3.16 takes the form

$$T_{AP}(\theta, H, P) = \tau(\theta, H)\left\{[1 - \rho(\theta, P)]\, T_S + \rho(\theta, P) T_{DN}(\theta)\right\} + T_{UP}(\theta, H) \tag{3.20}$$

The approximation of a specular surface has been made when remote sensing of atmospheric variables is desired, for example Grody (1976).

The description of surface reflectance and emittance becomes more complicated for a non-specular surface. Reflection from a rough surface can be expressed in terms of a bidirectional reflectance function. This is a function which relates the amount of incident radiance at a particular polarization at a particular angle to that reflected at a particular polarization and a particular angle. Such functions may be unknown or very complicated for the case of a rough sea surface and approximations are used in modelling these effects. The general form of the emittance of a rough surface is given by (Ulaby *et al.*, 1986):

$$\epsilon(\theta, P) = 1 - \frac{1}{4\pi \cos\theta} \int_{\Omega} [\sigma^{\circ}{}_{vp}(\mathbf{n}_s, \mathbf{n}_i) + \sigma^{\circ}{}_{hp}(\mathbf{n}_s, \mathbf{n}_i)]\, d\Omega \tag{3.21}$$

The coefficients σ° are scattering coefficients which are function of many variables, such as the slope distribution and the viewing geometry. Incoming and outgoing directions and polarizations are indicated by the subscripts and $\mathbf{n_i}$ terms. The reflected temperature contribution T_{SC} is given by

$$T_{SC}(\theta, P) = \frac{1}{4\pi \cos\theta} \int_{\Omega} [\sigma^{\circ}{}_{pv}(\mathbf{n}_s, \mathbf{n}_i) + \sigma^{\circ}{}_{ph}(\mathbf{n}_s, \mathbf{n}_i)]\, T_{DN}(\mathbf{n}_s) d\Omega \tag{3.22}$$

Modelling work to approximate the effects of surface roughness will be discussed in section 3.4.

3.2 Absorption and Emission by Gases at Microwave Frequencies

Atmospheric gases such as water vapor and oxygen absorb and emit radiation at certain frequencies, know as absorption lines. The radiation emitted by the atmosphere is randomly polarized or unpolarized (Ulaby *et al.*, 1981) while that from the surface is polarized. These frequencies of absorption and emission lines are due to energy transitions between the distinct energy levels of the molecule. Although the absorption occurs at distinct frequencies, the absorption lines are broadened in the atmosphere due to collisions and interactions with other components in the atmosphere. In the microwave region of the spectrum, pressure broadening arising from collisions between molecules is the most important cause of line broadening (Ulaby *et al.*, 1981). This means that absorption lines become broader at lower altitudes in the atmosphere. Description of the absorption line shape for various gases has been pursued both theoretically and experimentally, for example Rosenkranz (1975) and Liebe *et al.* (1977). The gaseous absorption coefficient σ_a referred to previously can be approximated through these types of models. The absorption coefficients can be employed in radiative transfer models to determine transmittance characteristics of the atmosphere. Figure 3.2 gives the transmittance in the microwave region for a tropical, standard, and polar atmosphere, where each atmosphere has a specified integrated water vapor amount. At the frequencies employed in this study, gaseous absorption by O_2 and water vapor are of primary importance. The essential features to note for the frequencies used in this study are the strong O_2 absorption region centered at 60 GHz and the weak water vapor absorption near 22 GHz. Note also that the transmittance for a polar atmosphere is greater than that for a tropical or standard atmosphere due to less water vapor. The general decrease in transmittance with increasing frequency is termed the water vapor absorption continuum.

Absorption bands are used for temperature sounding of the atmosphere. Early work on remote sensing of atmospheric temperature profiles is discussed by Staelin (1969) and Waters *et al.* (1975).

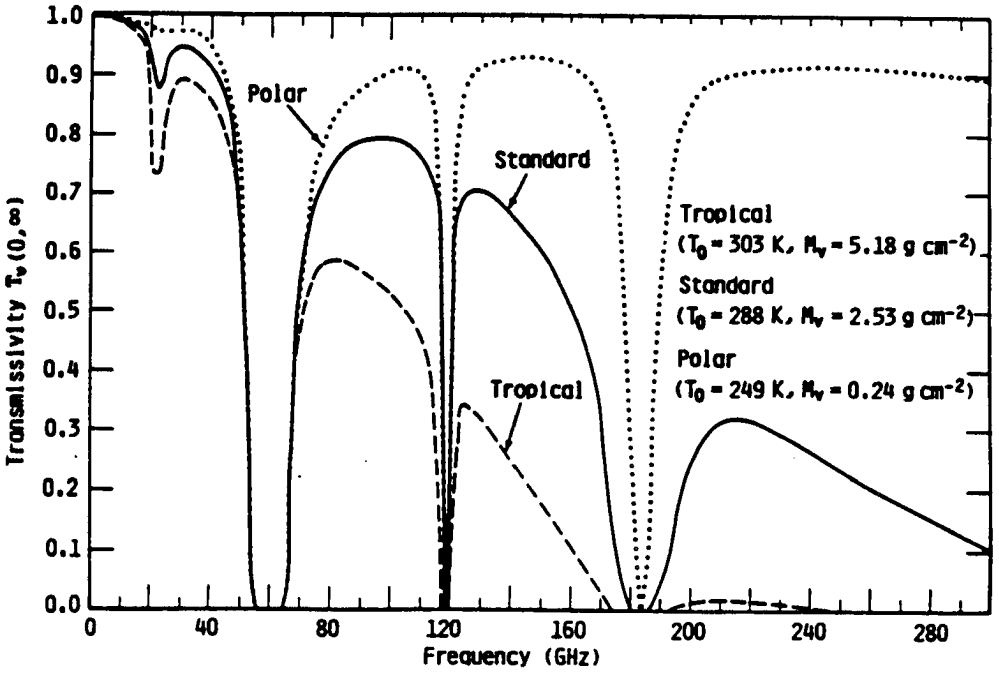

Figure 3.2: Atmospheric transmittance for a tropical, standard, and polar atmosphere (from Ulaby *et al.*, 1986).

The contribution of each level of the atmosphere to the radiance received by a satellite is determined by a weighting function. The weighting function $W(\nu, \theta, z)$ for a satellite temperature sounding channel for a plane parallel atmosphere at some altitude z is given by (Ulaby *et al.*, 1981)

$$W(\nu, \theta, z) = \sigma_a(z) e^{-\delta(z,\infty)\sec\theta} \sec\theta \tag{3.23}$$

The weighting functions for the MSU channels are illustrated in Figure 4.7.

There are three necessary characteristics for an absorbing gas to be used in atmospheric temperature sounding. These characteristics are (Spencer *et al.*, 1990):

1) The absorption is due to uniformly mixed gases whose absorption increases uniformly with pressure.

2) The absorption of other variable atmospheric constituents is small as compared to the uniformly mixed gas.

3) The effects due to surface emissivity changes are small as compared to the brightness temperature changes due to temperature changes.

The first criterion is met for O_2 in the atmosphere (Staelin, 1969). The other two factors will be examined in more detail for the interpretation of results for the polar low cases.

3.3 Effect of Hydrometeors at Microwave Frequencies

From Figure 3.2, which shows the transmittance of the atmosphere at microwave frequencies, we see that the atmosphere at microwave frequencies is mostly transparent with respect to gaseous absorption except for a few absorption bands previously mentioned. The presence of hydrometeors, cloud droplets and precipitation, has a major effect on microwave radiances at these frequencies. This section will examine the properties of hydrometeors at the frequencies of interest and their effect on microwave radiances.

Cloud name	Liquid water density (gm^{-3})	Mode radius of distribution (μm)
Cirrostratus, midlat.	0.10	40.0
Low-lying stratus	0.25	10.0
Fog layer	0.15	20.0
Fair weather cumulus	0.50	10.0
Cumulus congestus	0.80	20.0

Table 3.1: Some properties of standard cloud models (adapted from Ulaby *et al.*, 1981).

The scattering and extinction efficiencies of spherical particles can be determined what is known as Mie theory. These efficiencies are expressed in infinite series form. In Mie theory, the radiative properties of spherical particles are determined by a size parameter, in the atmosphere equal to the circumference of the particle divided by the wavelength of incident radiation, and the complex index of refraction of the particle, which accounts for absorption in the particle. These terms determine the amount of scattering and absorption of radiation for a given particle size distribution.

At microwave frequencies, the dependence of scattering and extinction efficiencies on particle size distribution can be eliminated through a truncation of the infinite series by what is known as the Rayleigh approximation. This approximation is justified when the product of the size parameter and the complex index of refraction of the water phase (liquid or ice) is sufficiently small (Ulaby *et al.*, 1981). When the Rayleigh approximation is valid, the extinction and scattering efficiencies have the useful property that they are a function only of the integrated droplet liquid water content and not of the droplet size distribution.

Some typical properties of precipitating and nonprecipitating clouds are listed in Table 3.1. There is little observational data on cloud properties in polar lows, so it is difficult to assign typical cloud properties to clouds in polar lows. From airborne radar measurements in a polar low, Shapiro *et al.* (1987) found reflectivities of up

to 45 dBZ in a 2 km deep layer near the surface, comparable in magnitude to reflectivities in tropical cyclones, although the vertical extent of the high reflectivity area was less.

Microwave remote sensing of hydrometeors can be divided into emission or scattering based methods (Spencer *et al.*, 1989). Emission based methods typically rely on low frequency channels below 30 GHz while scattering based methods use higher frequencies. The modelled response of the SSM/I frequencies to emission and scattering for a Marshall-Palmer droplet size distribution can be seen in Figure 3.3. The top plot shows the volume scattering coefficient as a function of rain rate. Note the large response of the 85 GHz channels to scattering while the 19 GHz channels show little response. Note also that the importance of scattering due to ice increases as frequency increases. The middle box shows the volume absorption coefficient for the same frequencies. Note that for all frequencies the absorption due to ice is much less than the absorption due to water. This is a feature of the microwave region where the absorption due to ice is roughly two orders of magnitude less than the absorption due to water. From this feature stems a most useful property of microwaves for remote sensing - their ability to penetrate ice clouds such as thin cirrus. Scattering affects the microwave radiances in precipitating ice clouds and can be used as an indirect measurement of precipitation below (Spencer *et al.*, 1989). The bottom panel shows the single scatter albedo at these frequencies. Note the very high values for ice clouds as compared to water clouds. Single scatter albedos approaching unity mean that radiation from below the ice layer is depleted, and since there are no other sources to replace it, low brightness temperatures result.

The response of the SSM/I frequencies to integrated cloud liquid water contents with scattering neglected are given in Figure 3.4. Note that the polarization difference decreases as the cloud water content increases.

Since microwave frequencies are sensitive to precipitation sized hydrometeors, brightness temperature-rain rate relationships have been developed for SSM/I

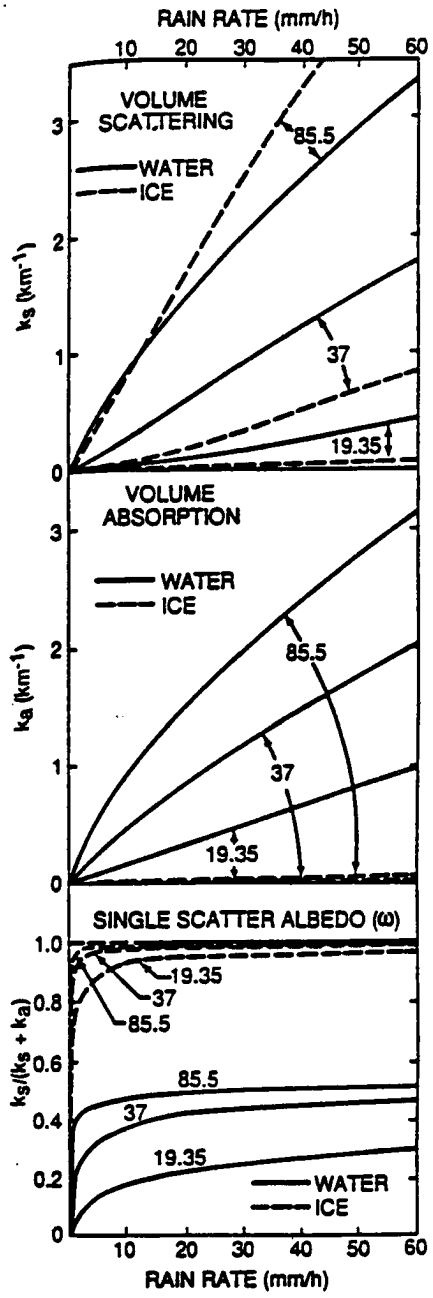

Figure 3.3: Mie volume scattering coefficients (top), volume absorption coefficients (middle) and single scattering albedos (bottom) of water and ice spheres at SSM/I frequencies for a Marshall-Palmer size distribution (from Spencer *et al.*, 1989).

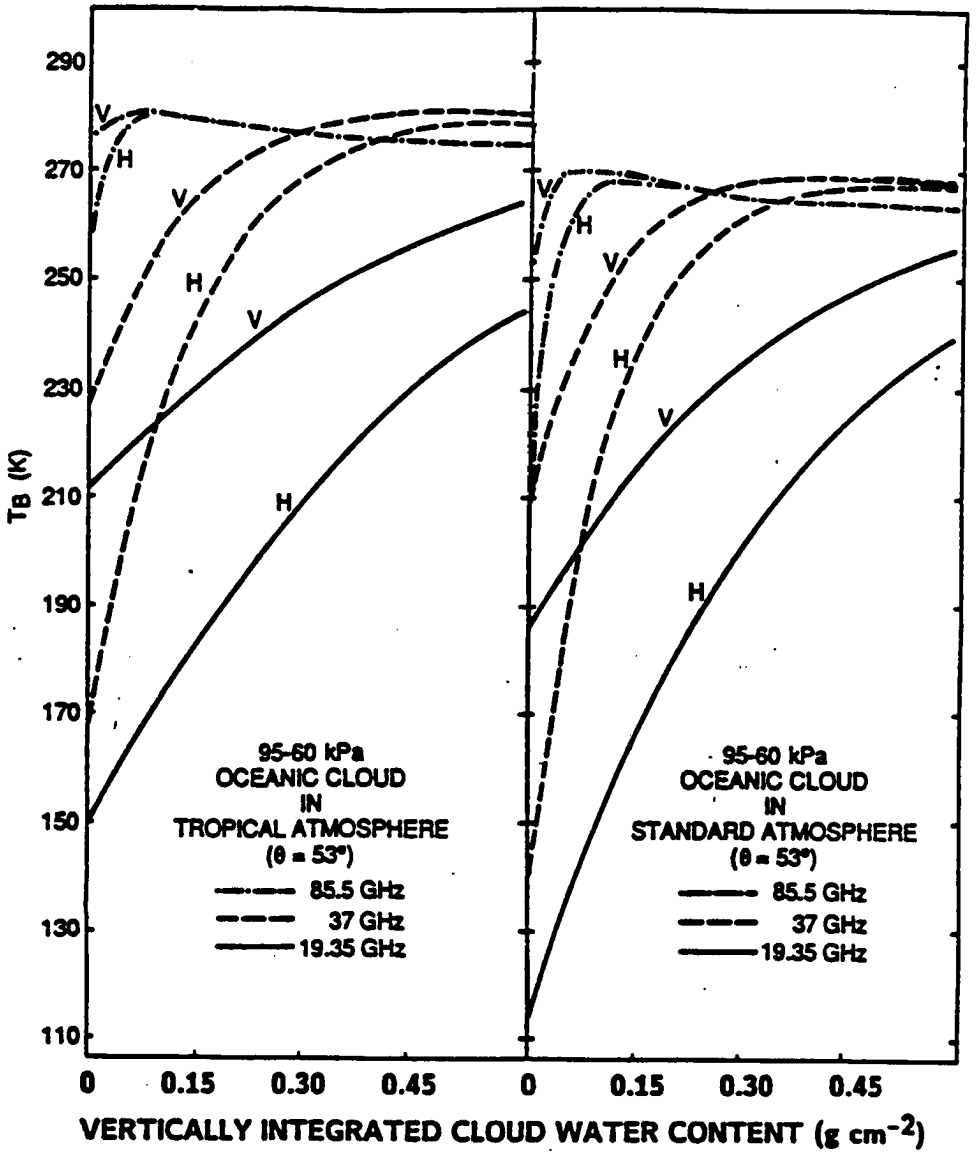

Figure 3.4: Modelled brightness temperatures at SSM/I frequencies assuming Rayleigh absorption as a function of integrated cloud water content for a tropical and standard atmosphere. Scattering is neglected (from Spencer *et al.*, 1989).

frequencies. An example is shown in Figure 3.5. These relationships are not unique due to vertical and horizontal variability in precipitating clouds. Note that precipitation over land causes brightness temperature decreases while over ocean the brightness temperatures increase up to a point and then decreases. The increase over water is due to the higher emissivity of a layer of water droplets than the ocean surface at microwave frequencies. Even though the physical temperature of the precipitation may be lower than the surface, the higher emissivity leads to brightness temperature increases up to a point until the colder physical temperature of the precipitation causes the brightness temperatures to decrease. Scattering is also a factor in brightness temperature decreases. Since land has a high background emissivity, precipitating clouds cause brightness temperatures to decrease over land.

An example of modelled effects of cloud water and precipitation on the MSU channels is presented in Figure 3.6. This modelling was performed to assess the effect of tropical cyclone conditions on the MSU channels. Scattering was neglected, a Marshall-Palmer droplet size distribution was assumed, and the Rayleigh approximation was used to compute absorption coefficients. The cloud was assumed to exist from the sea surface to 300 mb. It can be seen that the MSU 50.30 GHz channel shows increases in brightness temperature for both precipitating and non-precipitating clouds while the sounding channels are less affected and show a few degrees of cooling. Note that these results are for a deep cloud without an ice phase. Ice aloft would cause even larger brightness temperature decreases due to scattering. Comparisons of MSU 53.74 GHz brightness temperatures with clear column brightness temperatures computed from nearby radiosondes showed that satellite observed brightness temperatures over the storm could be 2-3 K lower than clear column values, with up to a 5 K decrease possible for conditions near the tropical cyclone center (Grody and Shen, 1982).

A concern in using microwave sounding frequencies over precipitating regions is that brightness temperatures will be reduced due to cloudiness and precipitation.

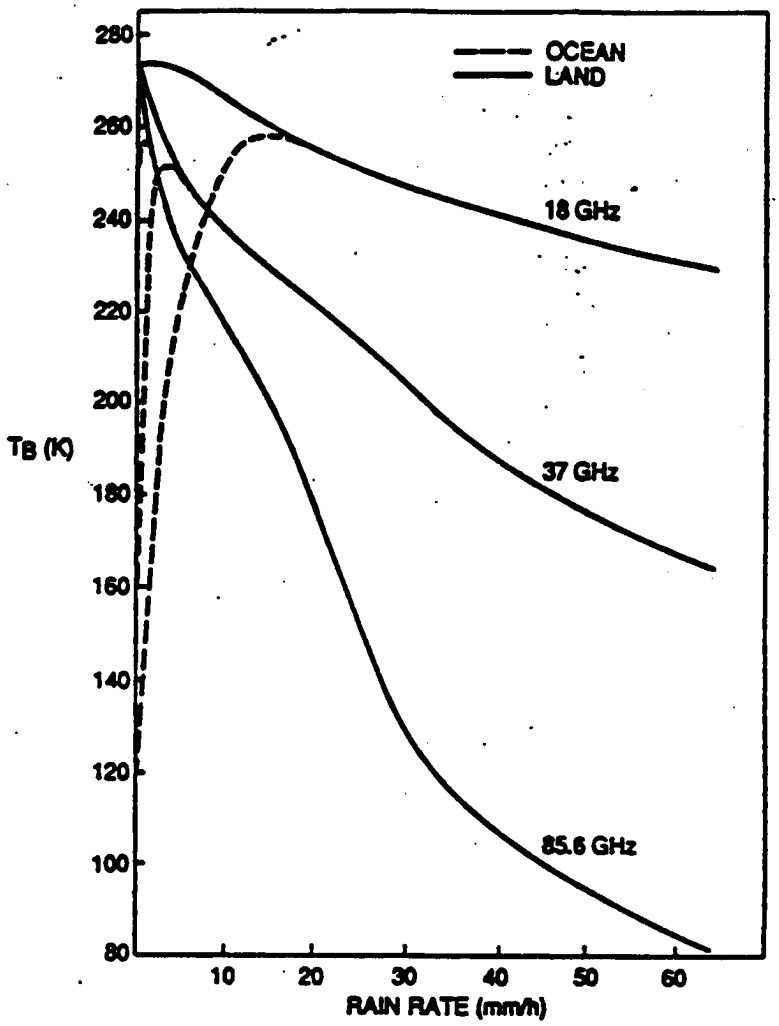

Figure 3.5: Modelled brightness temperature-rain rate relationship at SSM/I frequencies for ocean and land backgrounds. Note that precipitation causes brightness temperatures to decrease over land while they initially increase over the ocean and then decrease as the rain rate increases (from Spencer *et al.*, 1989).

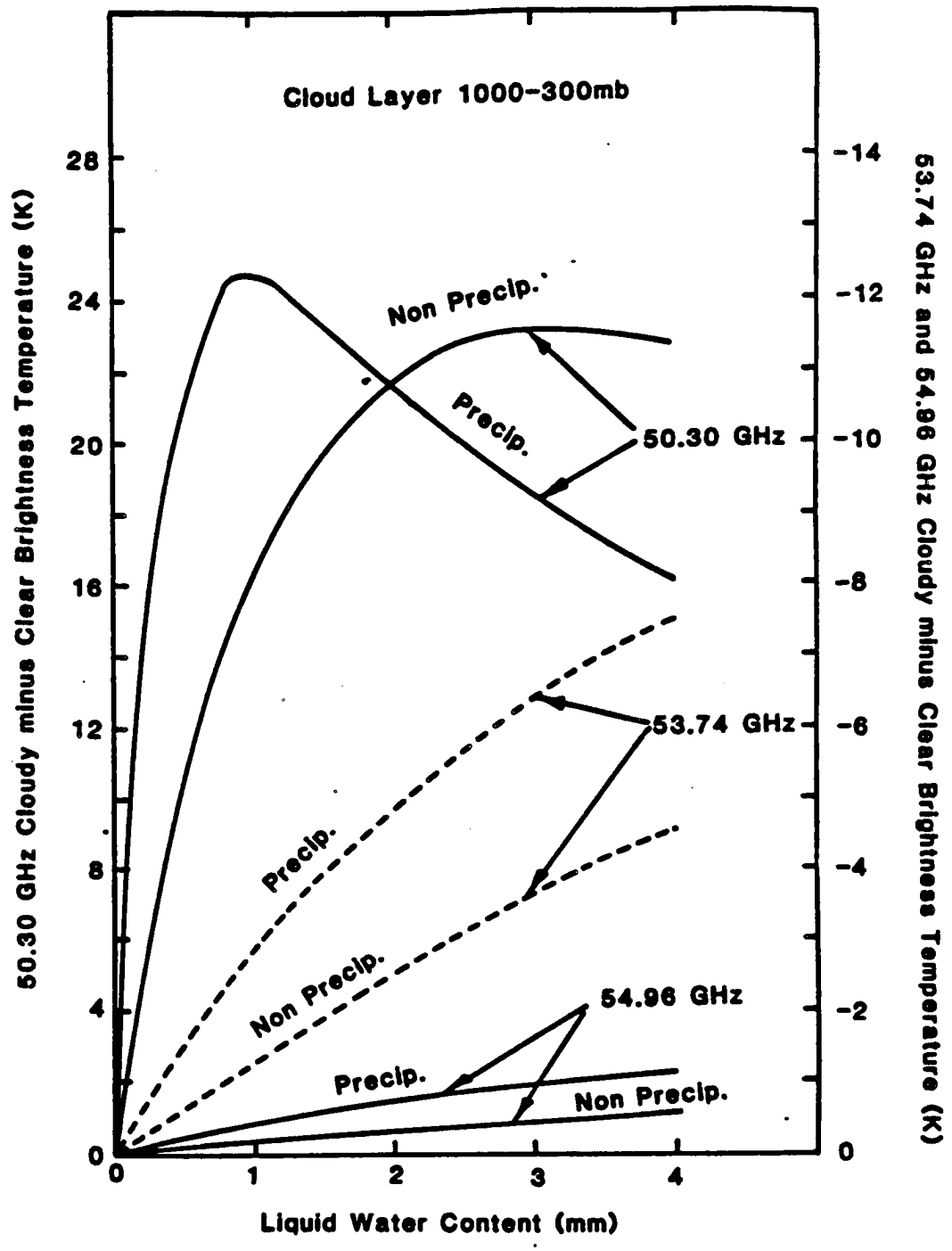

Figure 3.6: Simulated liquid water effects at MSU frequencies. Note the different signs on the vertical axes. See text for details (from Grody and Shen, 1982).

This is especially true in tropical areas with high liquid water contents and deep clouds. Procedures have been developed to screen out MSU brightness temperatures which have been affected due to precipitating clouds over land (Chenggang and Timchalk, 1988).

In summary, over the ocean cloud liquid water causes brightness temperatures to increase while liquid precipitation causes brightness temperatures to rapidly increase and then decrease. Ice particles decrease brightness temperatures due to scattering, with the effect becoming stronger at higher frequencies. Temperature sounding channels are much less sensitive to precipitation and liquid water effects. The effect of hydrometeors is dependent on the position of the peak of the weighting function with respect to the cloud (Legleau, 1989). These general results will be used to interpret brightness temperature changes at MSU frequencies over polar lows which may not be due to air temperature changes in the column.

3.4 Ocean Surface Effects at Microwave Frequencies

As illustrated by the radiative transfer equation, surface characteristics can have an effect on microwave radiation received at a satellite. The surface emits its own radiation and reflects radiation emitted from above the surface by the atmosphere. Surface emittance and reflectance change with many surface parameters. This allows opportunities in remote sensing of surface features through microwave radiometry. Over land, microwave remote sensing has been used to determine snow cover, soil moisture, and surface type (Hollinger, 1989). Since this study concentrates on polar lows, which spend the majority of their time over a water surface, only the effects of the ocean surface on microwave radiative transfer will be discussed. Microwave remote sensing of land parameters is complicated due to many variable surface types and their spatial inhomogeneity.

It is important to note that the microwave effects of geophysical processes are a function of the frequency, polarization, and local viewing angle of the satellite.

For the SSM/I this is fixed at 53° although there may be some slight along scan variation in this angle (Hollinger, 1991), thought to be primarily due to spacecraft altitude variations. As an example of the effect of viewing angle, the brightness temperature at four frequencies for a specular sea surface at vertical and horizontal polarization as a function of viewing angle is given in Figure 3.7. In this case the salinity has been fixed at 36 ppt and the sea temperature at 293 K. These brightness temperatures are computed through the use of the Fresnel equations. Note that for vertical polarization the emissivity increases until Brewster's angle is reached and then decreases rapidly while for horizontal polarization the emissivity decreases as viewing angle increases. At Brewster's angle there is no reflection of the vertically polarized component and thus the reflected horizontal component is completely polarized. Brewster's angle for an air - water interface can be found by setting the reflectivity of the surface in Equation 3.18 equal to zero. This gives Brewster's angle as the inverse tangent of the complex index of refraction of water at that frequency and temperature.

The following independent geophysical parameters can affect the microwave signature of the ocean surface:

Salinity

Sea Surface Temperature

Surface Pollution

Roughness of Surface

Foam

Their effects on microwave remote sensing will be now briefly discussed.

3.4.1 Geophysical Factors Not Directly Related to Wind Speed

1) Ocean Salinity

Since salinity effects are negligible above 4 GHz (Ulaby *et al.*, 1986), they can be ignored at the SSM/I and MSU frequencies.

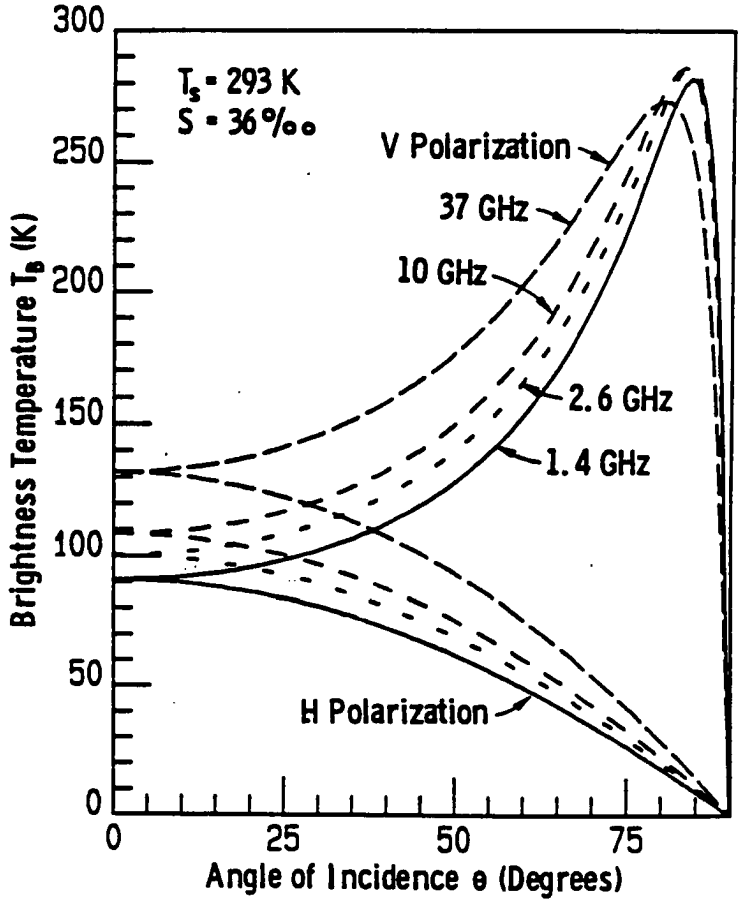

Figure 3.7: The brightness temperature of a specular sea surface at four microwave frequencies for vertical and horizontal polarization. The sea surface temperature and salinity are specified at 293 K and 36 parts per thousand, respectively (from Ulaby *et al.*, 1986).

2) Sea Surface Temperature

The amount of radiation emitted from the sea surface changes with temperature due to thermal emission and changes in emissivity. An example of the change of sea surface emissivity with temperature and viewing angle is given for 37 GHz in Figure 3.8.

3) Surface Pollution

Research has been performed on oil slick detection with microwave techniques. An oil slick over ocean water can affect the emissivity of the sea surface in two ways (Ulaby *et al.*, 1986). An oil covered surface may have a different emissivity than that of sea water and it may also damp out the smaller wave structures, leading to less surface roughness than an oil free surface.

3.4.2 Wind Effects

The final two geophysical factors affecting the microwave signature of the sea surface, surface roughness and foam, form the basis for remote sensing of surface wind speed. Satellite based passive microwave measurement of wind speed over the ocean was first suggested by Williams (1969). This suggestion was prompted by laboratory observations of increased microwave brightness temperature over a tank of water which was agitated to produce foam. Since this study employs measurements of surface wind speed derived from microwave measurements, the physical basis of how surface wind speed can be derived from such measurements from satellites will be explored. It should be noted that rigorous determination of the microwave properties of the sea surface remains an open problem (Guissard and Sobieski, 1987). Several attempts have been made to model the effect of surface wind on microwave radiation, for example Schluessel and Luthardt (1991), Petty (1990), Guissard and Sobieski (1987), Wentz (1983), and Wilheit (1979a).

In order to discuss the effects of surface wind speed on microwave brightness temperature, it is important to define surface wind speed. Since wind acts on the

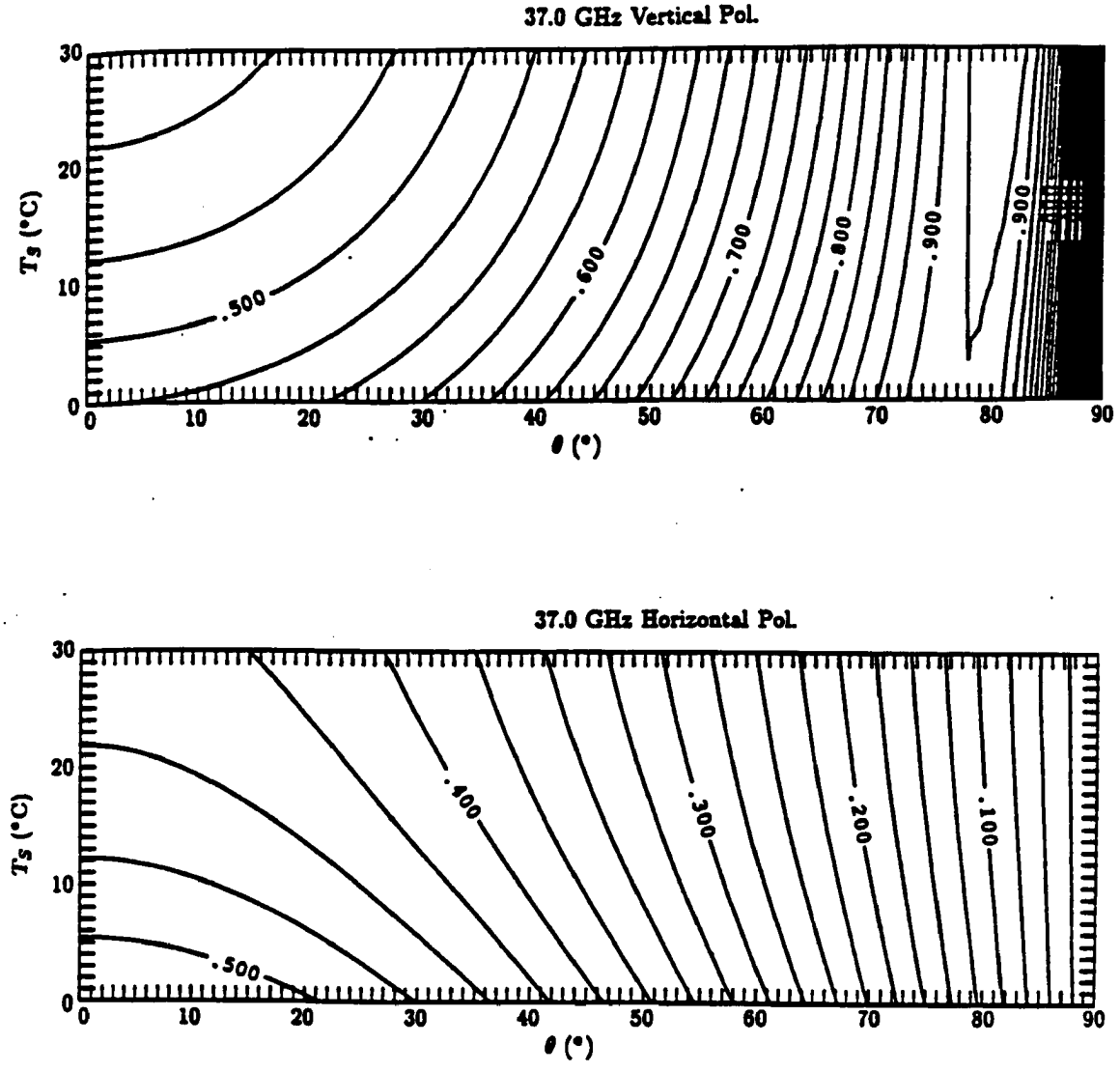

Figure 3.8: Emissivity of the sea surface as a function of sea surface temperature and viewing angle for horizontal and vertical polarization at 37 GHz (from Petty, 1990).

water surface through wind stress, this is the quantity which actually affects the sea surface. Retrieved measurements of surface wind speed are usually referenced to some height between 10 and 20 m above the surface. This is a typical anemometer height aboard a ship. Droplet loading from precipitation and sea spray can also decrease the wind speed in the lowest levels (Pielke and Lee, 1991). The surface wind speed values reported later in this study are referenced to 19.5 m above sea level.

Characteristics of the atmosphere such as stability (Glazman, 1991; Wilheit, 1979b) can affect the transfer of momentum to the sea and the relationship between wind speed and sea state. This makes the retrieval of surface wind speed via passive microwave methods a nontrivial problem. Additional complications are caused by the state of development of the sea, which affects the amount of whitecapping (Glazman, 1991), and possibly ocean currents, which can affect the growth of small waves depending on their relative velocity vector (Elachi, 1987). The remaining sections of this chapter will examine how the microwave signature of the ocean at SSM/I frequencies is affected by surface wind speed through the processes of surface roughening and foam generation.

The first process through which surface winds create a signal which can be detected with passive microwave measurements is through roughening of the sea surface. This has two effects on the microwave signature of the sea. Roughening can change the emissivity of the sea and roughening can also change the the amount of radiation which is reflected back from the atmosphere to a satellite receiver. These two effects will be discussed in more detail for SSM/I frequencies.

Change in Emitted Radiation due to Roughening

The problem of determining the change in surface surface emissivity with surface roughening can be approximated as a geometric optics problem, where one integrates the Fresnel relations over the distribution of surface slopes. Each slope

in the distribution is treated as a specular surface. The geometric optics approach ignores the effect of surface curvature and wave structure comparable in size to a wavelength (Wilheit, 1979a). In this approach it is assumed that the scales of roughness are large as compared to the wavelength of radiation. Applicability of the geometric optics theory improves with decreasing microwave wavelength (Petty, 1990). Stogryn (1967) was the first to take the geometric optics approach for modelling microwave characteristics of a rough sea surface. An important unknown is the reflectance function which is related to the slope distribution (Ulaby *et al.*, 1986). A widely used expression for the distribution of surface slopes with wind speed has been given by Cox and Munk (1954). They arrived at expressions for this distribution based on photographs of sun glitter. Wilheit (1979a) modified this expression to include a frequency dependency, where less of the variance was used at frequencies below 35 GHz. By specifying a distribution of slopes as a function of wind speed, the emittance and reflectance of the sea as a function of wind speed can be determined through such a model. The apparent temperature of the sea from Stogryn's (1967) model at 19.4 GHz for three wind speeds and a plane surface are shown in Figure 3.9 and Figure 3.10 for vertical and horizontal polarizations, respectively. The brightness temperature indicated is a combination of upward atmospheric emission, surface emission, and reflected atmospheric emission.

Petty (1990) used a geometric optics model to examine the relative contribution of surface emittance and reflected atmospheric radiation from wind roughening for the SSM/I. The emissivity of the sea was determined by integrating the Fresnel equations over a weighted distribution of surface slopes with the Cox and Munk (1954) form of sea surface variance. The change in emissivity of the sea surface due solely to roughening could then be determined as a function of sea surface temperature, viewing angle, and sea slope variance. A linear regression of the data was then performed. A sample result for a sea surface temperature of 275 K, frequencies of 19,

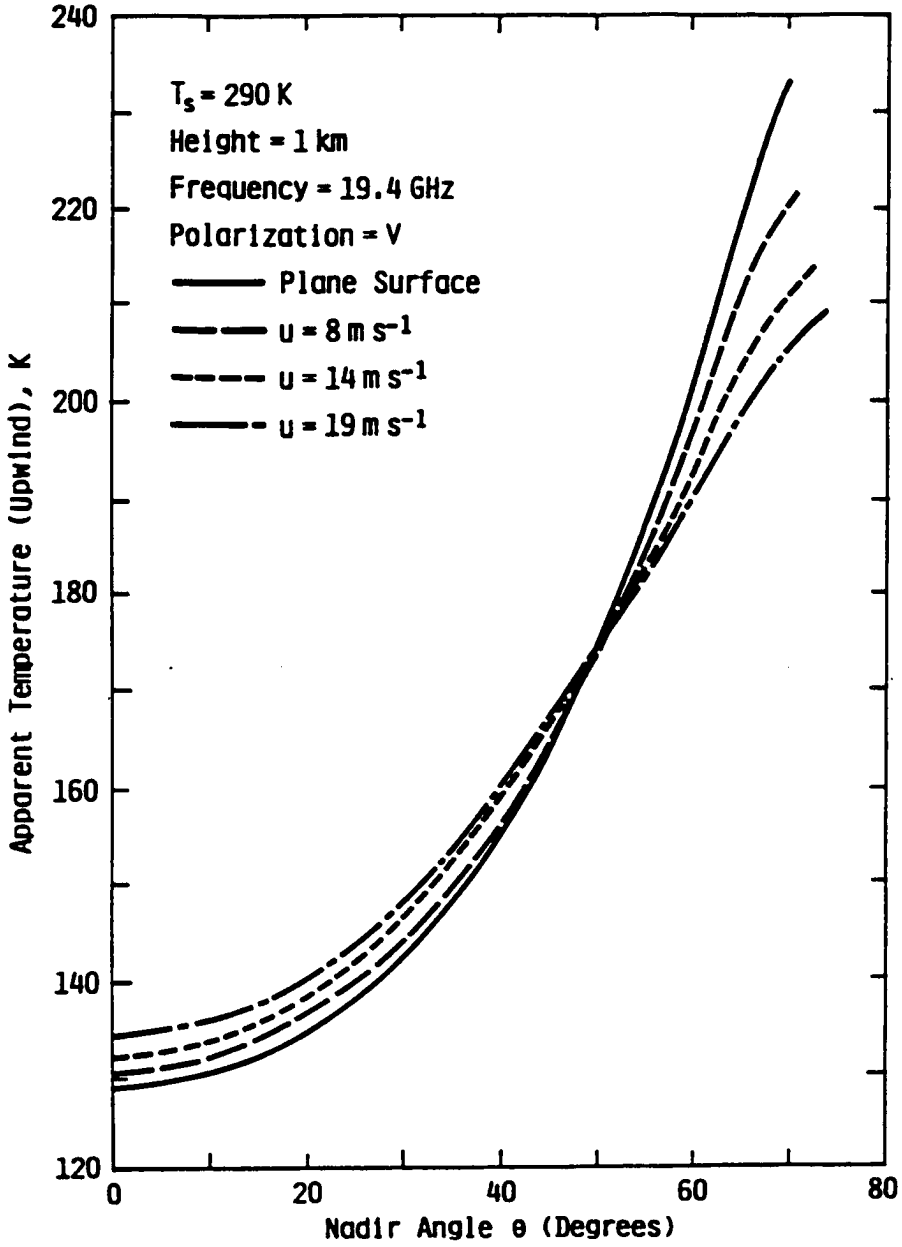

Figure 3.9: Modelled brightness temperature of the sea surface at vertical polarization at 19 GHz as a function of viewing angle at several wind speeds (from Ulaby *et al.*, 1986).

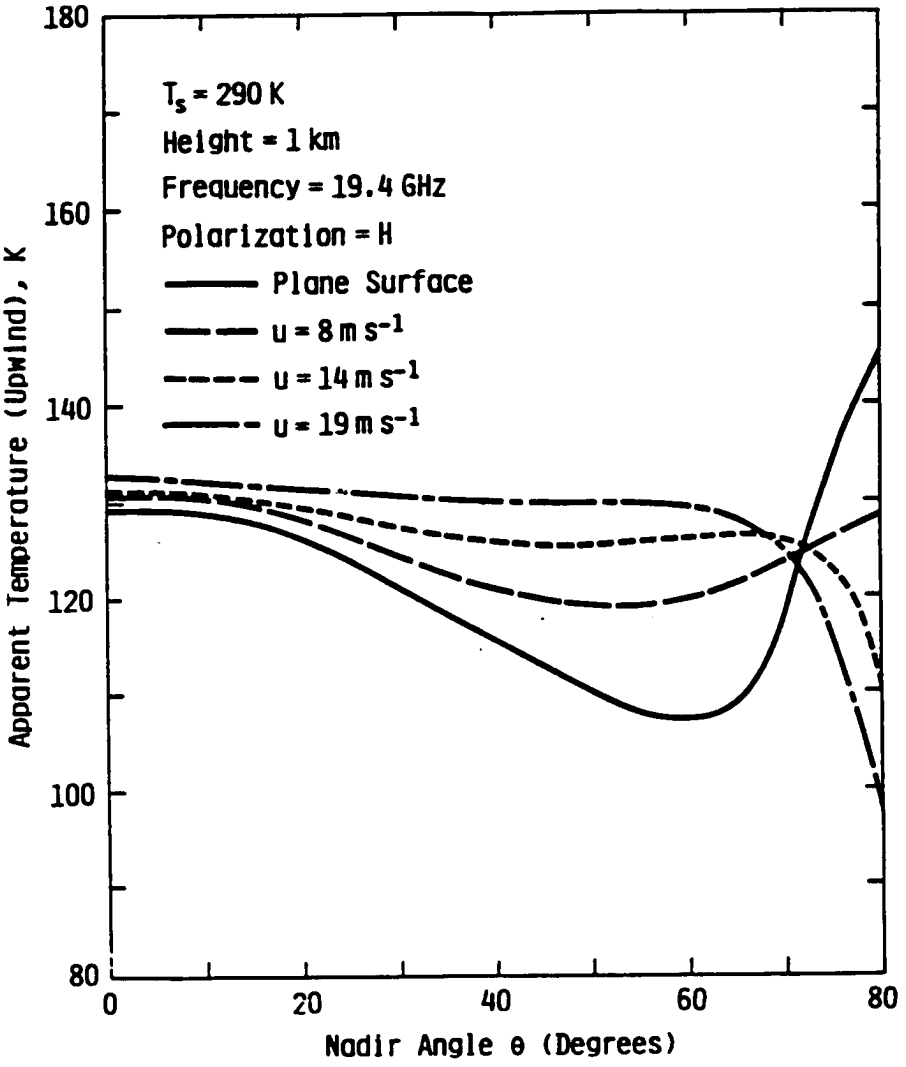

Figure 3.10: Modelled brightness temperature of the sea surface at horizontal polarization at 19 GHz as a function of viewing angle at several wind speeds (from Ulaby *et al.*, 1986).

37, and 85 GHz, vertical and horizontal polarization, and the SSM/I viewing angle is given in Figure 3.11. The results show that the horizontally polarized component of radiation due only to increasing surface emittance will increase with surface roughening while the vertically polarized component of radiation will decrease.

Hollinger (1971) used a tower to measure emitted microwave radiation from a foam free sea surface. Foam free does not mean that measurements were performed in calm seas but rather that the field of view of the radiometer was narrow so that foam patches could be excluded. An example of measurements of the change in brightness temperature for 19.34 GHz horizontal polarization is shown in Figure 3.12 as a function of wind speed, with positive values of Δ_{TB} indicating an increase in brightness temperature. Note that the reflected component is less with decreasing frequency due to less atmospheric emission at longer wavelengths.

Change in Reflected Radiation due to Roughening

The change of the diffusely reflected component of microwave radiation with surface roughness has often been overlooked (Petty, 1990). It was frequently modelled simply as a reflection from a specular surface while the surface emissivity was allowed to change due to roughening (Stogryn, 1972). The specular surface approximation has also been used when atmospheric variables were the subject of interest (Grody, 1976). Wentz (1983) made an attempt to parametrize the reflected sky radiation component by multiplying the specular component by a wind speed dependent component. This improvement has been further refined by Guissard and Sobieski (1987), who noted that the reflected contribution is a function of surface roughness and also the opacity of the atmosphere.

Petty (1990) examined the reflected component at SSM/I frequencies. Instead of modifying the reflectivity of the surface, the effective zenith angle of the downward sky component was allowed to vary while the reflectivity was set equal to one minus the wind roughened emissivity. The reflected brightness temperature was

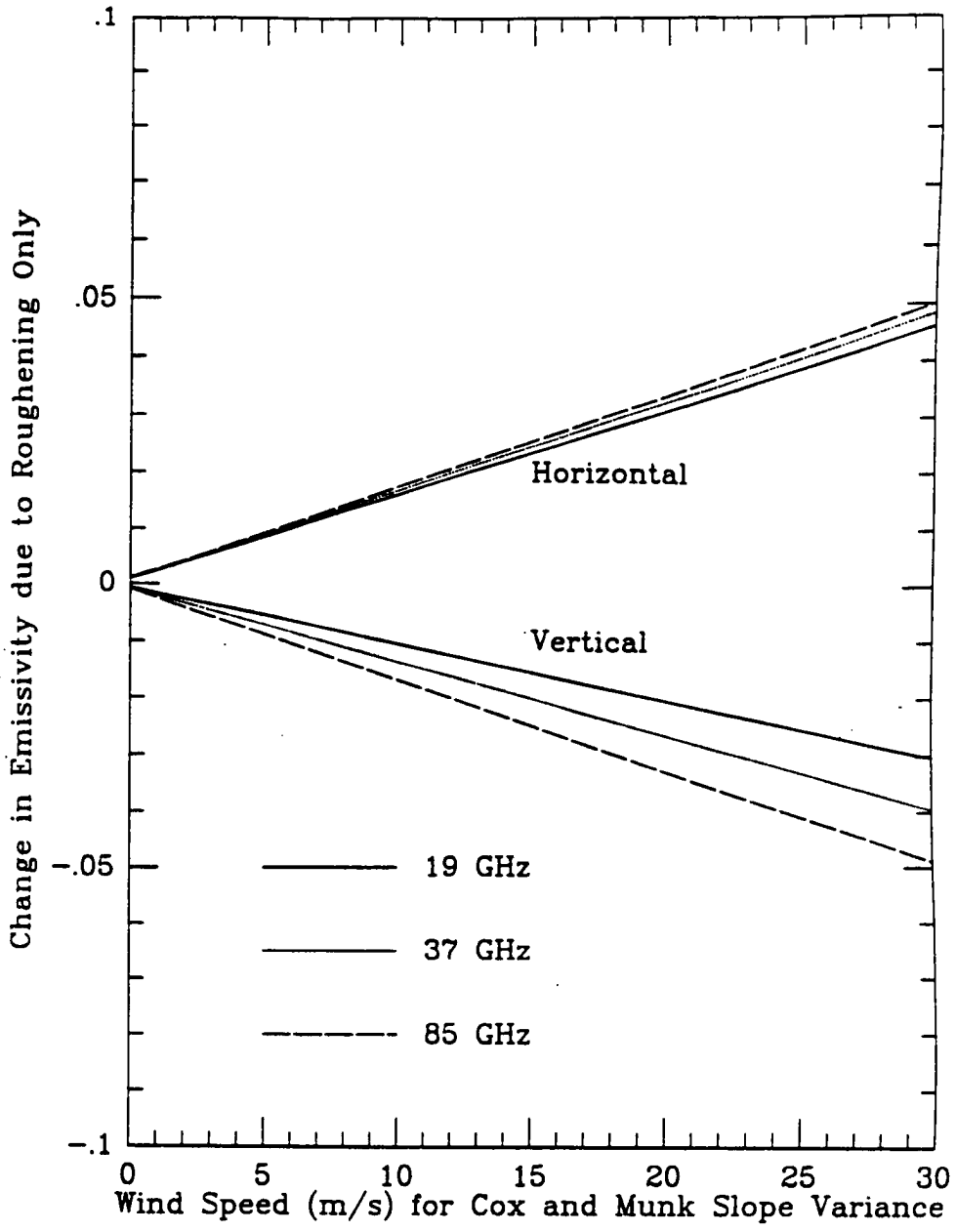

Figure 3.11: Change in the emissivity of the sea surface solely due to roughening from a Cox and Munk slope variance at SSM/I frequencies and polarization. Horizontally polarized emissivity increases while vertically polarized emissivity decreases. Based on the linear regression in Petty (1990).

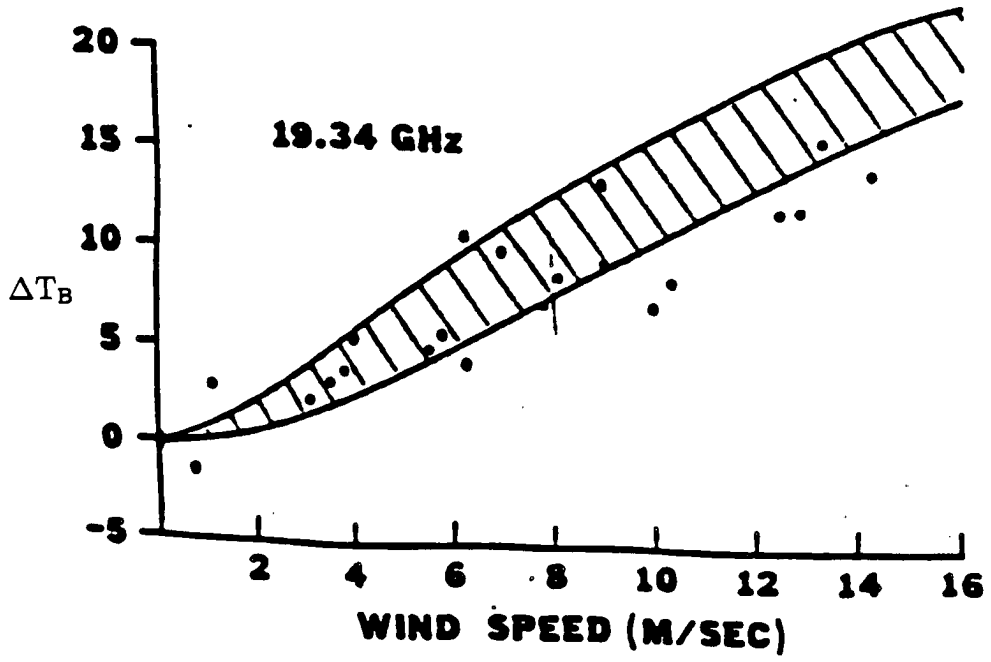

Figure 3.12: Measurements in foam free water (points) of the change in horizontally polarized brightness temperature at 19.34 GHz (from Hollinger, 1971).

simulated for a set of atmospheres, surface temperatures, and surface roughnesses. Results indicated that the reflected radiation component due to a roughened surface at horizontal polarization could be around 10 K different from that using the specular reflection method.

It has been suggested (Wentz, 1992) that a wind direction dependence of microwave radiance may be detectable through passive microwave radiometry. Such a dependence could enter through an anisotropy in the slope probability distribution, anisotropic height distribution of capillary waves, and a positional dependence of foam occurrence with respect to wave geometry. Wentz (1992) has detected such a signal as a residual error in wind speed retrieval. Previous studies (Wilheit, 1979b) suggest that any wind direction dependence has less of an effect on the microwave radiances than that of a 2 m/s change in wind speed, for a 50° viewing angle.

Another possible impact on surface roughness and therefore wind speed determination has been suggested by Olson (1987). This is the effect that rain drop impacts may have on roughening the surface. This may be a moot point in passive microwave remote sensing of the sea surface since the wind signal from the surface would be replaced by emission from the overlying precipitation. When the surface signal is reduced to a value less than the instrument noise, accurate wind speed retrievals are not possible (Goodberlet *et al.*, 1989). Droplet effects on the sea surface may be more important for active microwave remote sensing of surface wind speed (*e.g.* Moore *et al.*, 1979).

An example of the effects of surface roughness at 19 GHz horizontal polarization for wind speeds of 4 and 14 m/s is given in Figure 3.13, which is based on a geometric optics model. It can be seen that the surface contribution increases with incidence angle and wind speed while the reflected contribution increases to a point and then decreases. The surface contribution to the radiance measured at the satellite for horizontal polarization increases for increasing wind speeds, corresponding

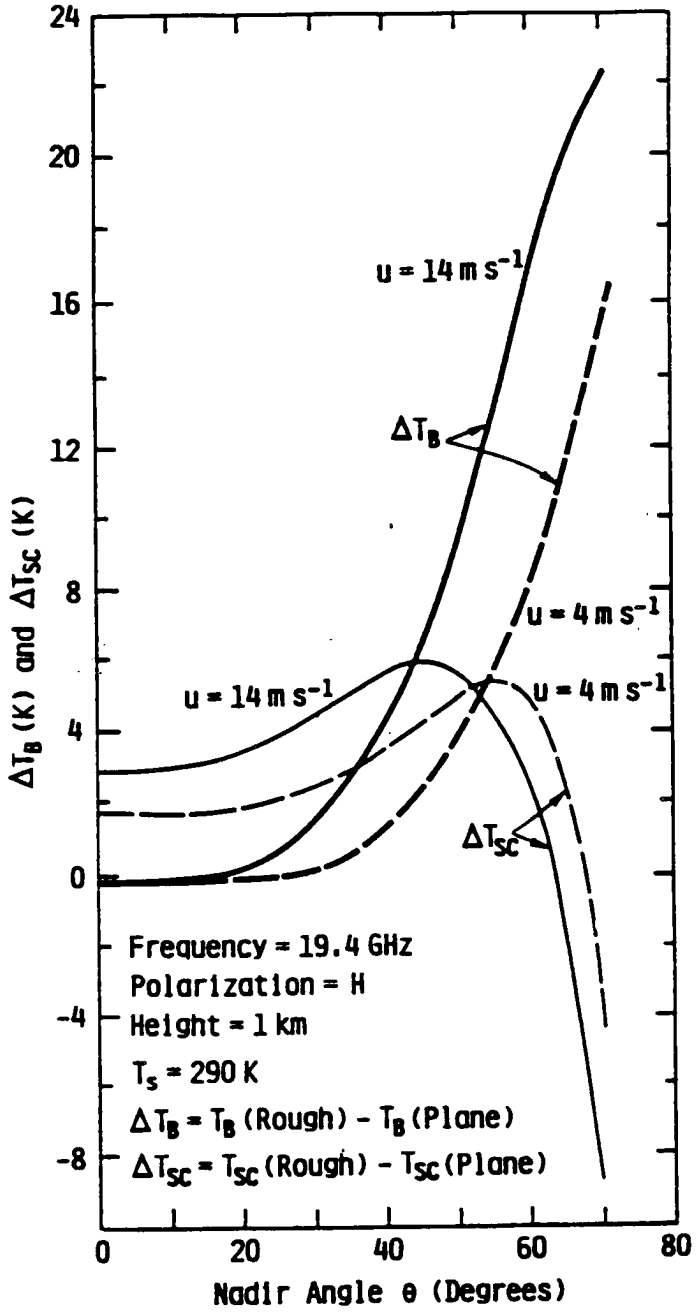

Figure 3.13: Relative contributions of the surface and reflected sky emissions at 19.4 GHz horizontal polarization. ΔT_B indicates the change in surface emission and ΔT_{SC} is the change in radiation scattered from the surface (from Ulaby *et al.*, 1986).

to increasing surface emissivity. Along with the foam contribution to be discussed next, these factors form the physical basis for microwave remote sensing of sea state.

Sea Foam

Foam on the sea surface has an important effect on passive microwave measurements. For SSM/I frequencies at vertical and horizontal polarization, patches of foam on the sea surface serve to increase the emissivity of the the sea surface over that of a foam free surface. As with surface roughness effects, the relationship between surface wind speed, foam coverage, and microwave radiance is difficult to quantify.

"Foam" is a term which is used rather loosely in microwave remote sensing. Under the general heading of foam, there exist mixtures of air and water which have different microwave properties and different dependencies on wind speed (Smith, 1988; Ross and Cardone, 1974). Variable properties of foam such as bubble density and thickness can affect the microwave emissivity of foam (Smith, 1988). In a statistical sense, foam may be considered isotropic (Stogryn, 1972). The rise velocity of bubbles is influenced by water temperature (Monaghan and Ó Muircheartaigh, 1980), adding an additional complication to the lifetime of foam once it is formed. The ratio of foam streaks to whitecaps increases as wind speed increases (Ross and Cardone, 1974), and these two components may have different emissivities and different effects on sea surface emissivity (Wentz, 1983). Field studies of foam in the past have relied on visible photographs of the foam cover on the sea. It is not clear whether the visible foam coverage seen on a photograph is the same as the microwave coverage (Petty, 1990). The term foam can be used explicitly to describe the ensemble properties of air-water mixtures on the ocean surface or as a term to describe all residual sea surface emissivity changes which are not accounted for by surface roughness models (Petty, 1990).

The foam coverage at the ocean surface generally increases as surface wind speed increases. Measurements at 19.35 GHz have shown that foam starts to form when surface wind speed increases above 7 m/s (Nordberg *et al.*, 1971). From empirical techniques, the form of the increase appears to follow the 10 m wind speed raised to between the 3rd and 4th power (Monaghan and Ó Muircheartaigh, 1980). For a 20 m/s wind, this empirical description gives a foam coverage of about 11 %. In modelling the fraction of the sea covered by foam , Wilheit (1979a) set the foam fraction to zero at wind speeds below 7 m/s.

There have been several field measurements of the brightness temperature of foam at frequencies below 37 GHz. By using an antenna with a small field of view and flying at low altitudes, spikes were recognized in brightness temperature measurements and these were matched up with patches of foam on the sea surface. An example is shown in Figure 3.14.

By accounting for the reflected sky contribution, the emissivity of sea foam can be estimated. Smith (1988) observed that the 37 GHz vertically polarized emissivity of foam was greater than the 19 GHz vertically polarized emissivity which was in turn greater than the 37 GHz horizontally polarized emissivity. The values determined were 0.82, 0.73, and 0.67, respectively. Stogryn (1972) has parameterized the frequency and viewing angle dependence of foam emissivity.

Now that the principal effects of surface wind speed on microwave brightness temperatures at SSM/I frequencies have been discussed, we can look at some modelling results for change in brightness temperature as a function of wind speed. Figure 3.15 gives the modelled response of the low frequency SSM/I channels as a function of wind speed for a surface temperature of 294 K and a midlatitude atmosphere (Schluessel and Luthardt, 1991). This includes parameterized foam and surface roughening effects. While these are simulated results, they do show some significant features of the effect of surface wind on microwave brightness temperatures. The greater sensitivity of the horizontally polarized channels is evident in

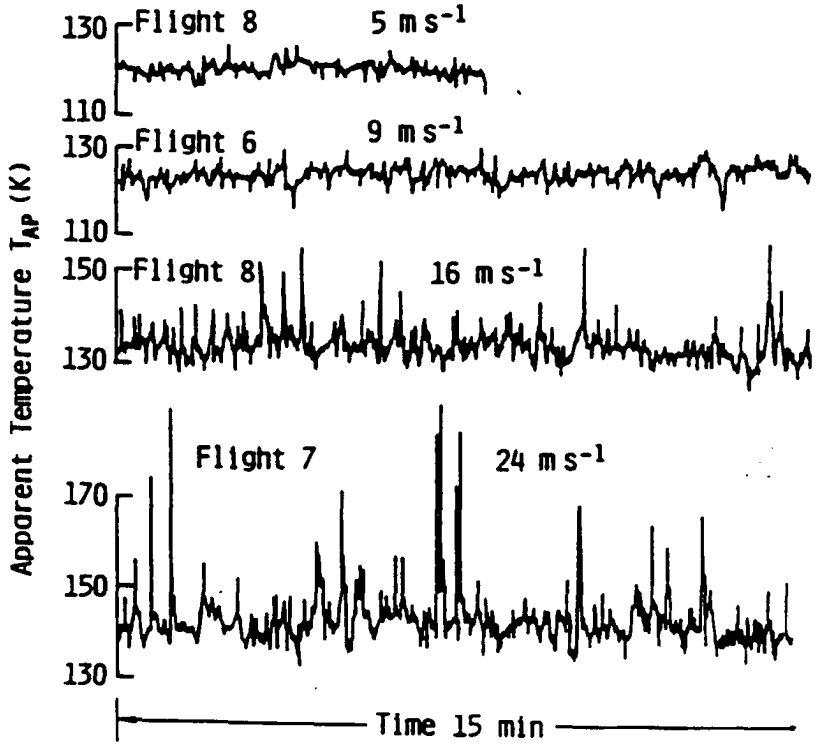

Figure 3.14: Time records of the nadir apparent temperature at 19.35 GHz from aircraft measurements. The spikes are due to foam patches (from Ulaby *et al.*, 1986).

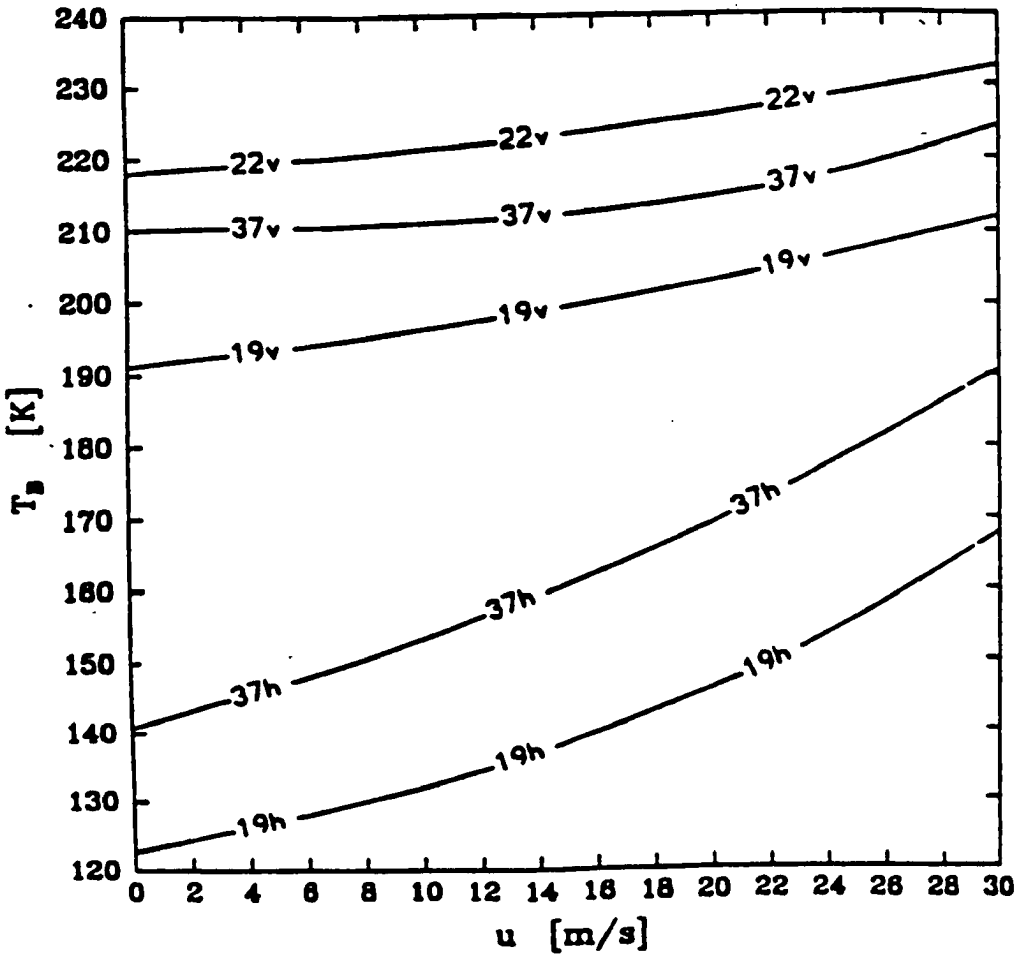

Figure 3.15: Simulated response of SSM/I brightness temperatures for a midlatitude summer situation (from Schluessel and Luthardt, 1991).

Figure 3.15. Although one might think that wind speed could easily be determined given the large response of the horizontally polarized channels, atmospheric effects also affect their response so that the wind speed signal can be lost. This is the reason that regression approaches like the global D-matrix have the lowest standard deviation when several channels and polarizations are used to separate the surface and atmospheric contributions to radiance.

Chapter 4

DATA AND ALGORITHMS

4.1 Special Sensor Microwave/Imager Instrument Description

The SSM/I instrument used in this study is a conically scanning linearly polarized seven channel total power passive microwave radiometer aboard the DMSP Block 5D-2 F8 satellite. The F8 satellite is in a sun synchronous near-polar orbit at an altitude on 833 km and was launched June 19, 1987 (Hollinger, 1989). A DMSP satellite with an SSM/I is shown in Figure 4.1. The F8 satellite has an ascending node equatorial crossing local time of 0613 A.M. with a period of 102 minutes.

The SSM/I measures microwave radiation at the frequencies, wavelengths, polarizations, and channel numbers listed in Table 4.1. The 3 dB (half power)

Channel number	ν, λ (GHz),(cm)	Polar-ization (H or V)	3 dB Effective field of view (km)	Sensitivity (K)	Accuracy (K)
1	19.35, 1.55	V	70 x 45	0.45	1.5
2	19.35, 1.55	H	70 x 45	0.42	1.5
3	22.235, 1.34	V	60 x 40	0.74	1.5
4	37.0, 0.81	V	38 x 30	0.37	1.5
5	37.0, 0.81	H	38 x 30	0.38	1.5
6	85.5, 0.35	V	16 x 14	0.69	1.5
7	85.5, 0.35	H	16 x 14	0.73	1.5

Table 4.1: SSM/I instrument characteristic (adapted from Jones and Vonder Haar, 1989).

effective field of view of the instrument yields the resolutions listed in Table 4.1. At the microwave frequencies of the SSM/I, the wavelength of the radiation is not negligible compared to the size of the parabolic reflector, which is 61 x 66 cm.

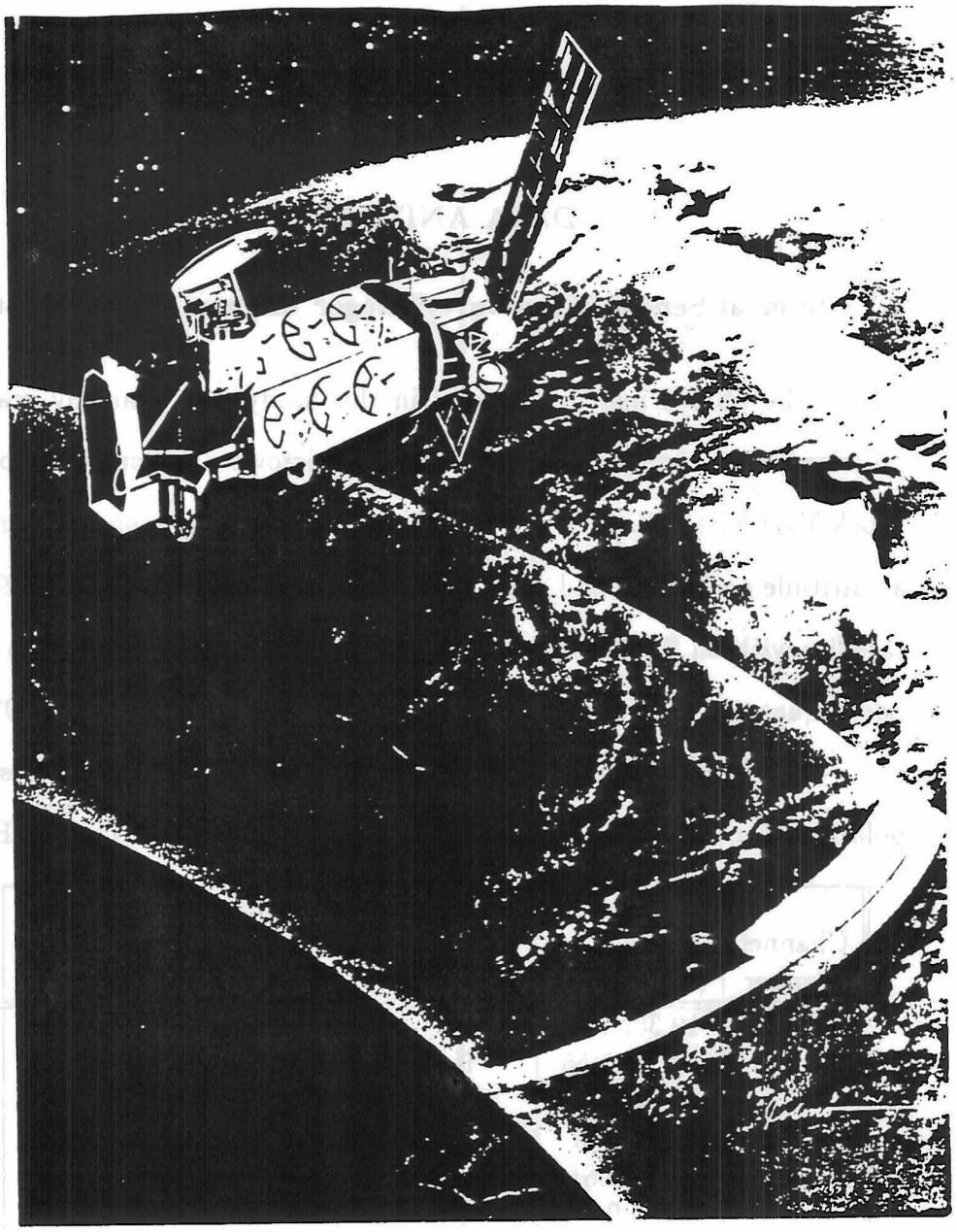

Figure 4.1: Drawing of DMSP Block 5D-2 satellite with an SSM/I (from Hollinger, 1989).

This means that lower frequencies have lower resolutions for a given antenna size. The sensitivity or noise equivalent temperature differential, which is the standard deviation of the radiometer output referenced to the incident energy on the aperture, is also given in Table 4.1. The values, which are for January 1989, show the low frequency channels used in this study to be extremely stable. Unfortunately, the 85 GHz vertically polarized channel had failed at the time of this study. The absolute accuracy , as best as it can be determined, is also given in Table 4.1.

As opposed to the Dicke radiometers of the MSU, the SSM/I is the first satellite microwave radiometer to use a total power design (Hollinger, 1989). The total power design gives a factor of two improvement in signal to noise as compared to a Dicke radiometer. The differences between the MSU and SSM/I radiometers are discussed by Westwater and Fedor (1991).

The SSM/I reflector and feedhorn rotate together at a rate of 31.6 revolutions per minute. On each scan, the SSM/I views two targets of known temperature, a hot body whose temperature is measured to be around 254 K and a cold view of space whose temperature is 2.7 K (Westwater and Fedor, 1991). This means scanning is not interrupted for calibration. There are occasionally missing groups of scan lines due to data transmission problems. The constant viewing angle means that corrections for a changing viewing angle do not have to be made, as opposed to the MSU. The SSM/I instrument apart from the satellite is shown in Figure 4.2. The SSM/I scans to the aft of the spacecraft in a 102° degree arc, at a 53° earth incidence angle which translates into a swath width of 1394 km. The 24 hour coverage of the SSM/I is illustrated in Figure 4.3 and the SSM/I scan geometry is shown in Figure 4.4. The higher resolution 85 GHz channels are sampled 128 times each scan line while the other channels are sampled 64 times every other scan line. As the sub - satellite track speed is 6.58 km/s, and the time interval between scan lines is 1.9 s, each scan line is separated by 12.5 km. The 85 GHz channels are

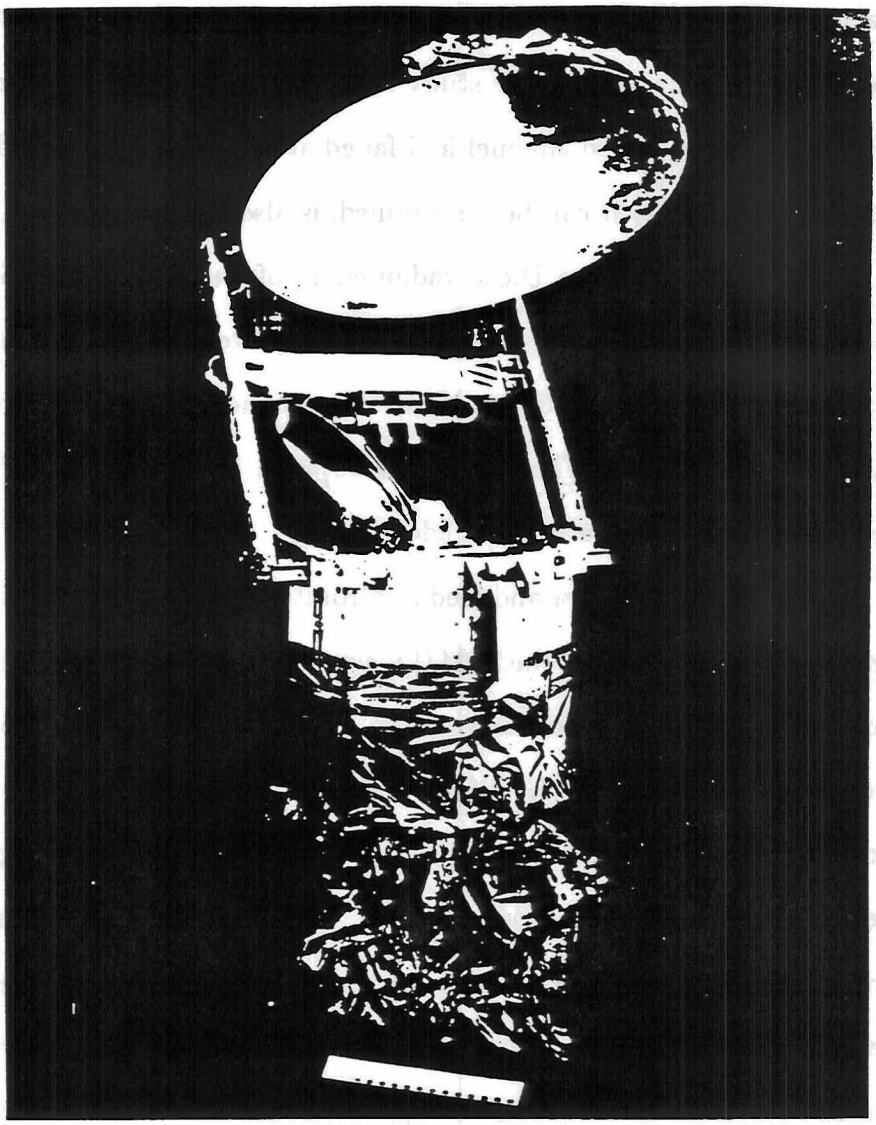

Figure 4.2: SSM/I in deployed position apart from satellite (from Hollinger, 1989).

sampled every 12.5 km while the other channels are sampled at 25 km increments. This means that the highest frequency channels are sampled at a rate close to their resolution while the lower frequency channels are oversampled.

Having considered the essential features of the SSM/I, it is worthwhile to briefly note a few reasons for choosing a few of the instrument parameters. The relative sensitivity of microwave observations from 1 to 40 GHz to various geophysical parameters is shown in Figure 4.5. This is a conceptual diagram but it shows that the low frequency SSM/I channels have maximum sensitivity to surface wind speed, cloud liquid water, and water vapor. Through examination of these sensitivities, as well as considering radiometer design constraints for each selected frequency, appropriate frequencies for the sensor mission have been chosen. Since the SSM/I is an imaging instrument, the SSM/I channels were chosen to be window channels which have a minimum of gaseous absorption in the atmosphere. The exception is Channel 3 which is located on a weak water vapor absorption line.

At the incidence angle of the SSM/I, 53°, measurements are not highly dependent on surface wind speed while at the same time they allow the wind speed to be determined. This can be seen by referring back to Figures 3.9 and 3.10, where it can be seen that the vertically polarized brightness temperature has a minimum in wind sensitivity near 50° while the horizontally polarized component has a maximum in the 50° to 60° region. An incidence angle of 49° was used for the predecessor to the SSM/I, the SMMR. Changes in the SSM/I incidence angle have been proposed to allow for greater swath width. Such proposed changes must consider the dependence of wind speed sensitivity on incidence angle.

4.2 Microwave Sounding Unit Instrument Description

The MSU is a part of NOAA's operational satellite sounding system, the TIROS-N Operational Vertical Sounder (TOVS) which includes other infrared and microwave instruments. It was first launched aboard the TIROS-N satellite in 1978

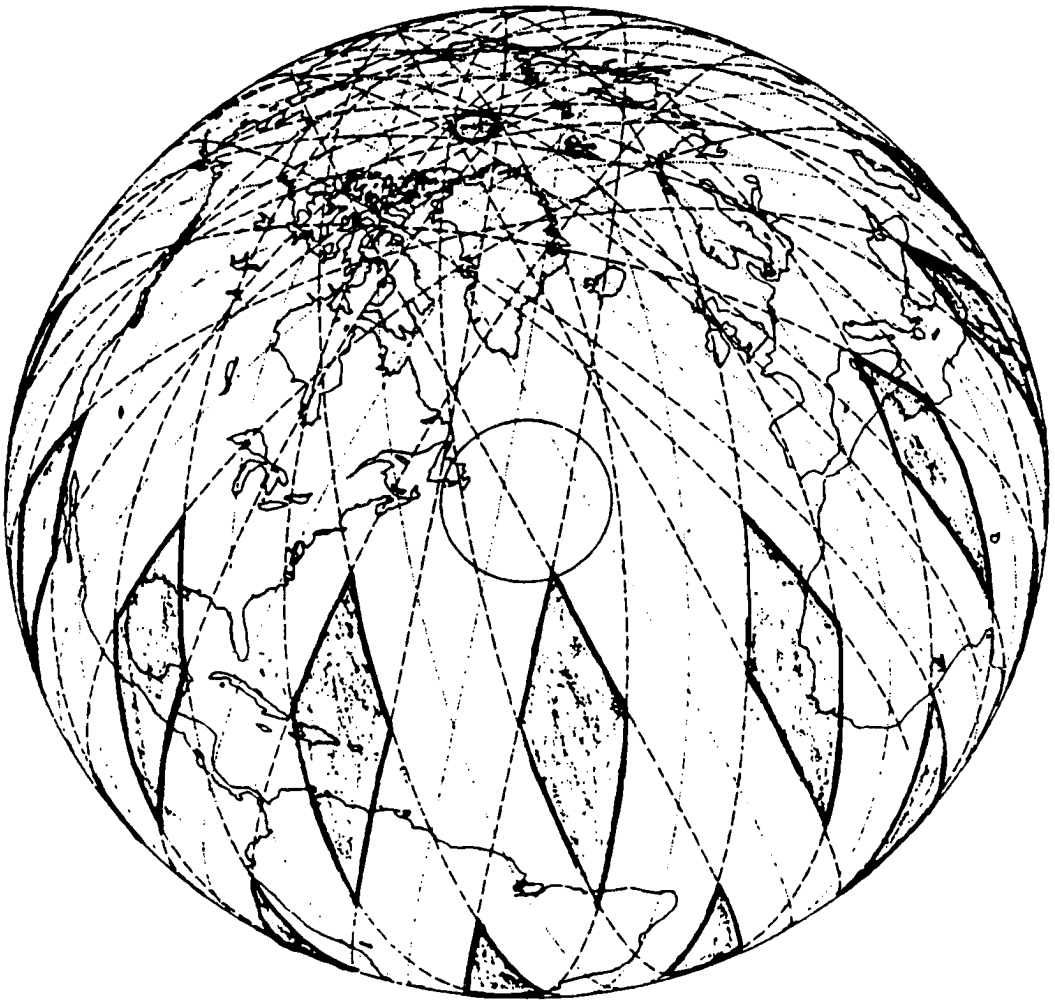

Figure 4.3: Coverage of the SSM/I in 24 hours (from Hollinger, 1989).

SCAN A	
SCENE STATIONS/SCAN	128
PIXELS/SCAN	576
SCAN B	
SCENE STATIONS/SCAN	128
PIXELS/SCAN	256
SCENE STATION/ORBIT	404,224
PIXELS/ORBIT	1,313,728

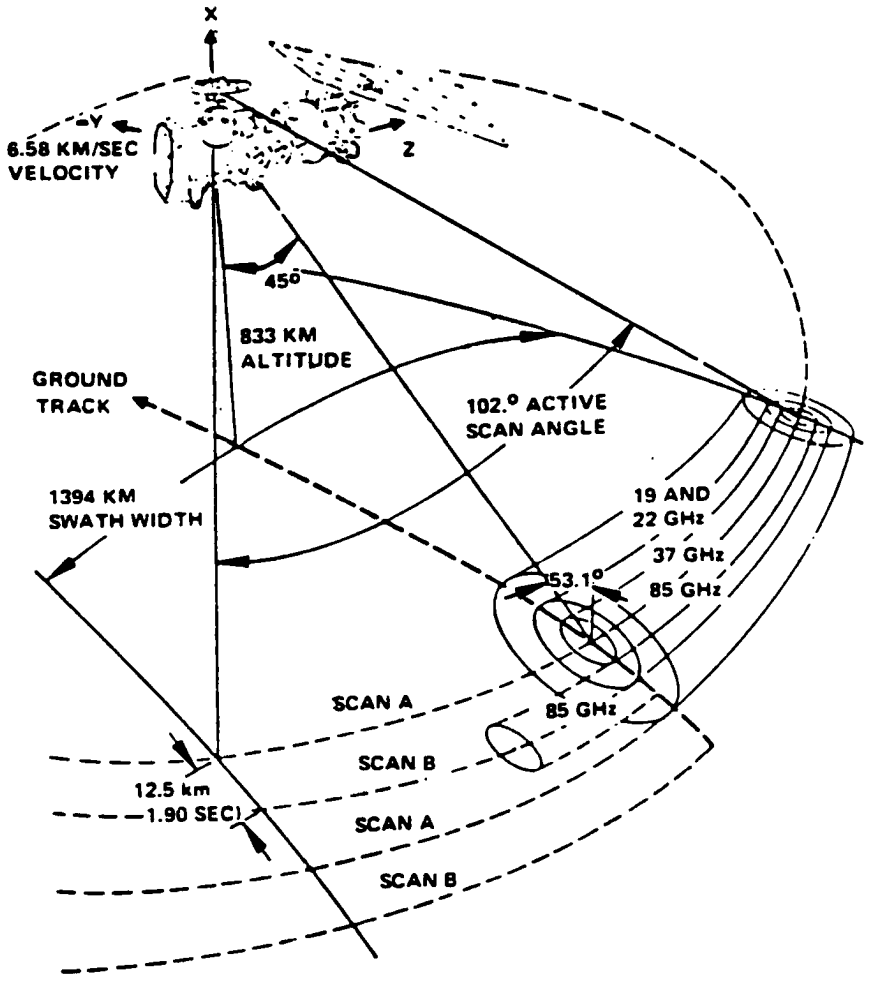

Figure 4.4: SSM/I conical scanning geometry (from Hollinger, 1989).

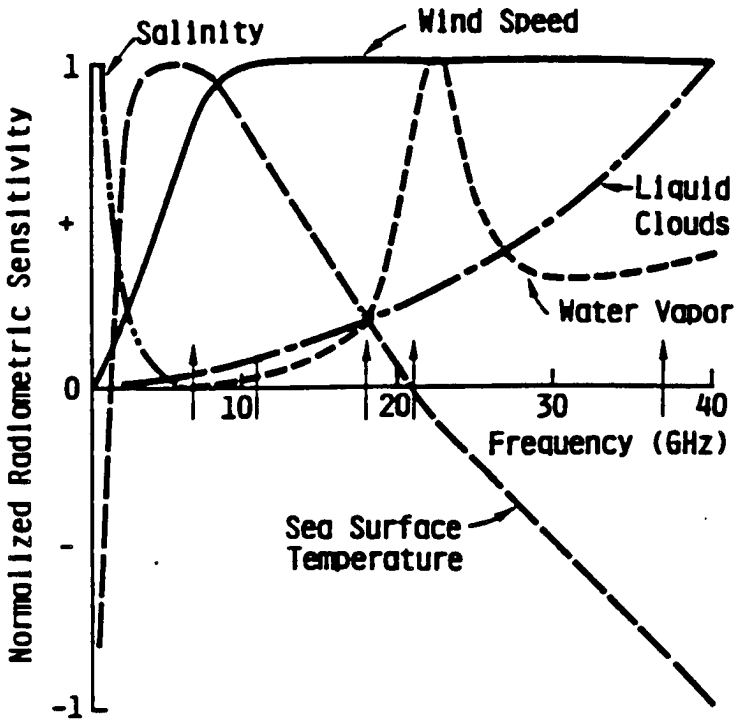

Figure 4.5: Relative sensitivity of microwave measurements to various geophysical parameters in the 1 to 40 GHz range (from Ulaby *et al.*, 1986).

and is aboard the NOAA series of polar orbiting satellites. A NOAA satellite is illustrated in Figure 4.6. The NOAA satellites are in a near-polar, sun-synchronous orbit at an altitude of 833 km, similar to the orbit of the DMSP F8 satellite. The orbital period is 102 minutes, resulting in 14.1 orbits per day. A detailed description of the NOAA satellites can be found in Schwalb (1978).

The Microwave Sounding Unit consists of four Dicke radiometers designed to sense atmospheric temperature by passively measuring microwave radiation on the wings of the 60 GHz oxygen absorption band. It can be viewed as a successor to the Scanning Microwave Spectrometer (SCAMS) which was aboard the Nimbus series of satellites. These channels sense radiant energy from successively higher levels in the atmosphere as the center of the 60 GHz oxygen absorption band is approached. The nadir and scan limit weighting functions shown in Figure 4.7 illustrate the relative contribution of each level to the total radiant energy. The weighting functions for surface emissivities of 0.5 and 1.0 are also shown for the 50.30 and 53.74 GHz channels. Grody (1983) calculates a 70 K possible increase in 50.30 GHz brightness temperature for a land versus sea background and only a 1.4 K possible increase in 50.30 GHz brightness temperature. These results are for a surface temperature of 285 K. As the MSU scans away from nadir, the weighting functions peak at higher levels due to the longer atmospheric path length. The weighting functions illustrate the fact that the MSU is a sounding instrument which is designed to respond to gaseous O_2 absorption. The 50.73 GHz channel is a window channel designed to determine surface emittance and to aid in temperature sounding.

Unlike the conical scan pattern of the SSM/I, the MSU is stepped through 11 scenes of earth, including a nadir view at the number 6 central scan position. The MSU has two scanning reflector antennas, one for the 50.30 and 53.74 GHz channels and the other for the 54.96 and 57.95 GHz channels. The MSU as it looks removed from the NOAA satellite is shown in Figure 4.8. The two reflectors are

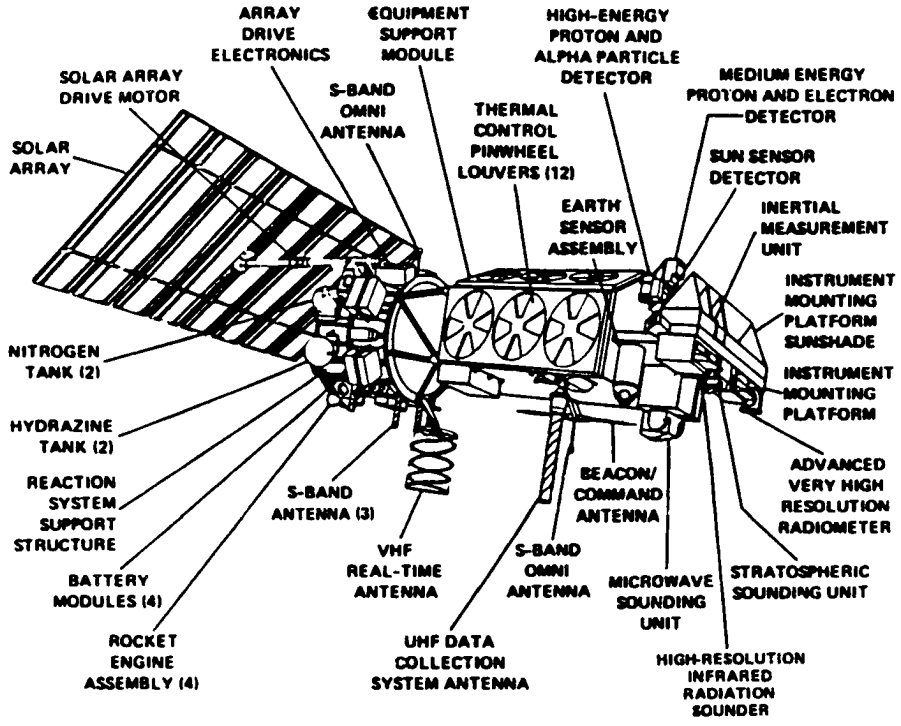

Figure 4.6: NOAA spacecraft. Location of MSU is indicated (from Schwalb, 1978).

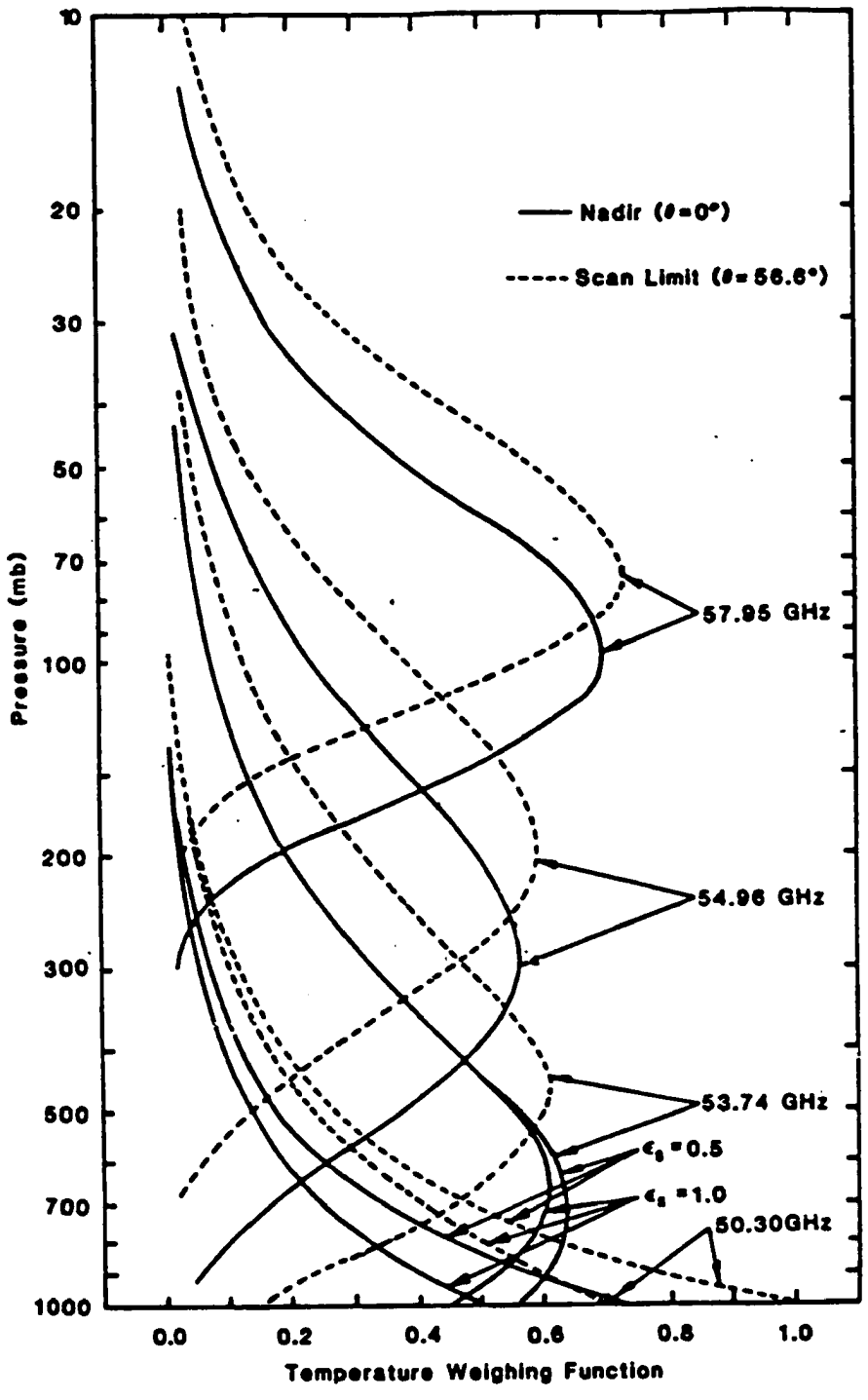

Figure 4.7: MSU weighting functions for nadir and scan limit positions. Channel 1 and 2 weighting functions are shown for surface emittances of 1.0 and 0.5 (from Grody and Shen, 1982).

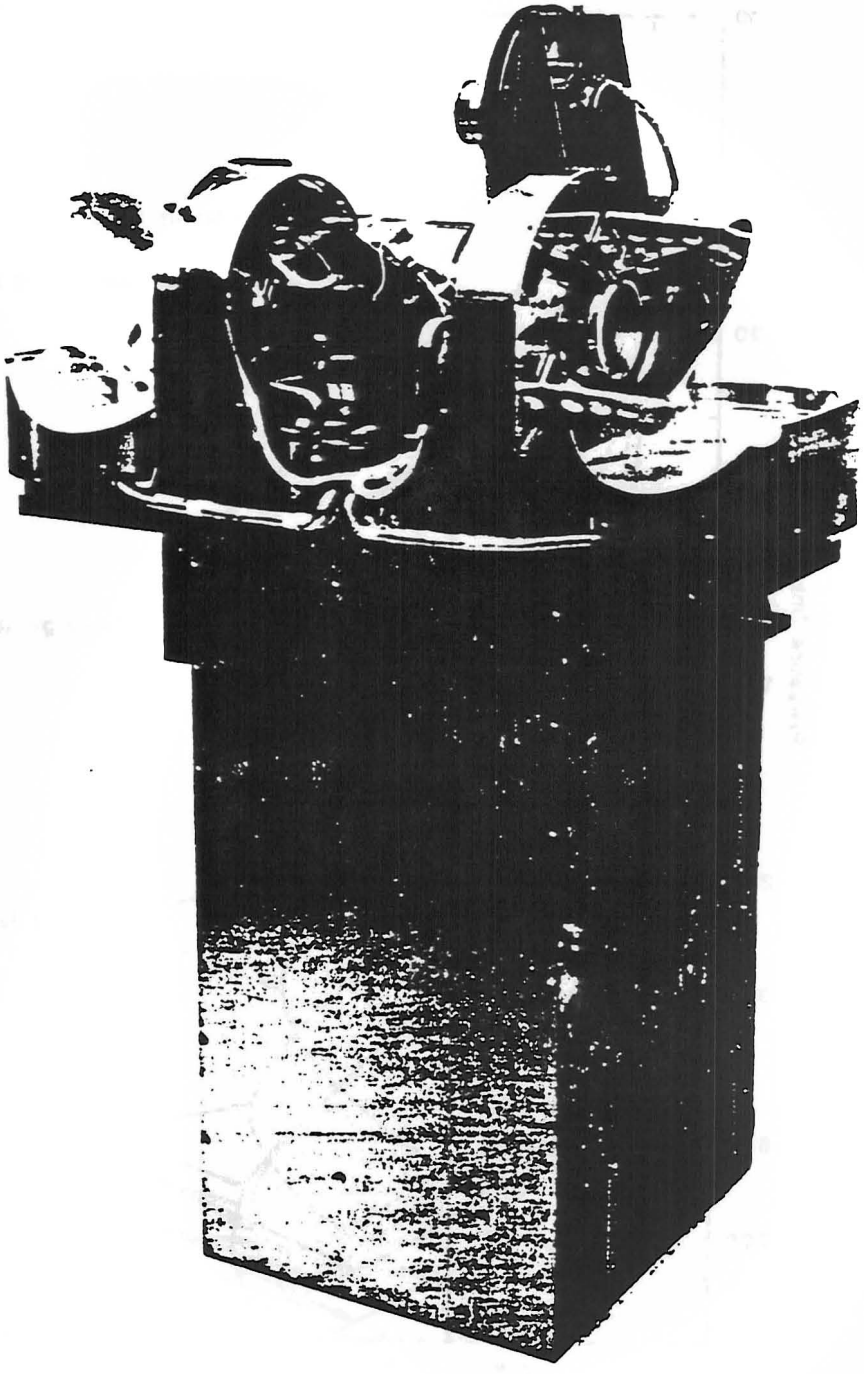

Figure 4.8: MSU instrument apart from satellite (from Schwalb, 1978).

step scanned every 1.84 seconds by 9.47°. At the end of each scan, two additional steps are taken to allow calibration views of cold space and a view of a calibration target with an embedded temperature monitor. The incoming radiation enters the feedhorn, is separated into vertical and horizontal components, and travels to a radiometer. The radiometer is modulated at a 1 KHz rate between an internal source and the incoming signal by a Dicke switch. The radiometer output signal is detected by a receiver, whose output voltage is proportional to the brightness temperature difference between the scene and the internal source. Calibration is accomplished using the nearly linear response between output voltage and calibration target voltages (Kidwell, 1988; Werbowetzki, 1981). The sensitivity of the MSU channels is estimated at 0.3 K and the absolute accuracy is estimated at 1 K (Westwater and Fedor, 1991).

The scan pattern for the MSU is shown in Figure 4.9. Note the underlap between scan spots and the increasingly large area from which scan spots away from nadir sense radiation. The instrument characteristics including the channel numbers which will be used in this report are listed in Table 4.2. A complete scan line, including viewing of the calibration targets, is accomplished every 25.6 seconds. The 3 dB (half power) resolution of the scan spots degrades from 110 km x 110 km at nadir to 178 km x 323 km at outer scan positions 1 and 11. Detailed descriptions of the MSU can be found in Spencer *et al.* (1990) and Kidwell (1988).

The horizontal resolution of the MSU is the greatest limitation in using this instrument to study polar lows. With a nadir resolution of the MSU of 110 km and a typical size of a polar low of 400 km or less in diameter, the MSU is not capable of resolving much thermal structure within a polar low. Figure 4.10 shows what the MSU scan pattern may look like superimposed on a polar low. In most cases, the resolution will be worse than the nadir resolution due to the greater likelihood that a polar low will be imaged on one of the outer scan spots, which cover a greater area.

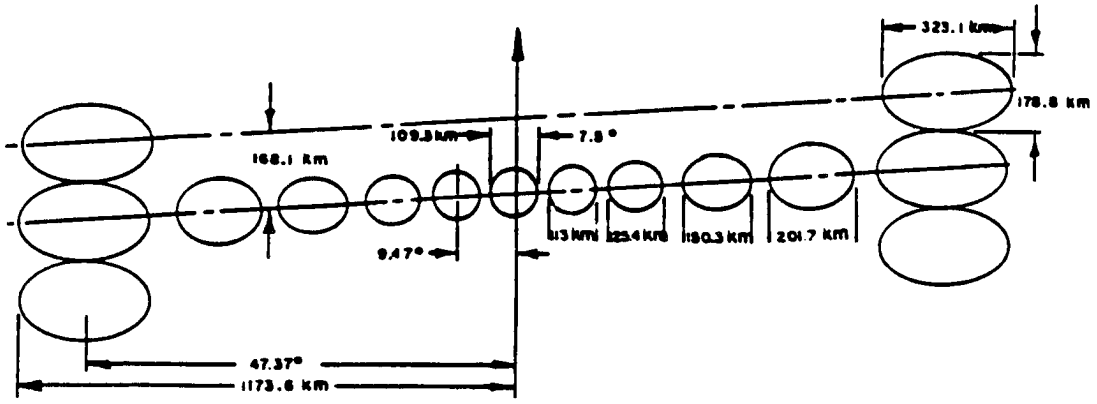

MICROWAVE SOUNDING UNIT

SCAN PATTERN PROJECTED ON EARTH

(833.4 km CIRCULAR ORBIT)

Figure 4.9: MSU scan pattern and half power field of view projected on earth (from Grody and Shen, 1982).

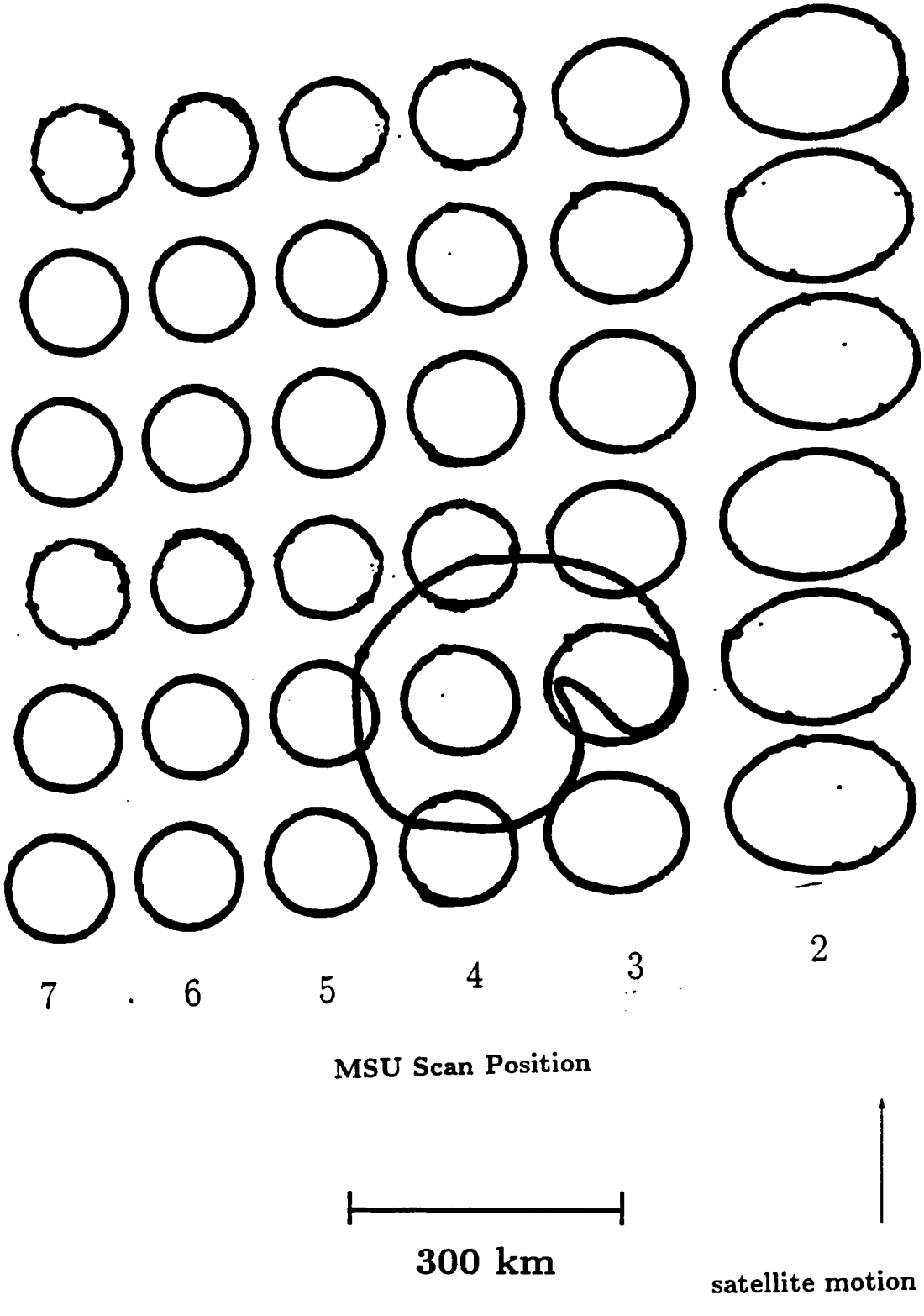

Figure 4.10: Schematic diagram of a portion of the scan pattern of the MSU superimposed on a typical size (about 300 km diameter) polar low, illustrating the resolution limitations of the MSU. Only two scan spots almost entirely cover the polar low.

Parameter	Value
Instrument type:	Dicke radiometer
Channel Frequencies:	
Channel 1:	50.30 GHz
Channel 2:	53.74 GHz
Channel 3:	54.96 GHz
Channel 4:	57.95 GHz
RF bandwidth:	220 MHz
Noise equivalent Δ T_B:	0.3 K
Angular resolution:	7.5° (3 dB)
Ground field of view:	109 x 109 km at nadir
Cross track scan angle:	±47.35°
Cross track scan distance:	±1015 km
Time per scan:	25.6 sec.
Number of earth views per scan:	11
Scan step angle:	9.47°
Time between scan steps:	1.84 sec.

Table 4.2: Microwave Sounding Unit instrument characteristics (adapted from Vroman, 1989)

Since the MSU does not have a constant viewing angle, a process known as limb correction is performed on the data. The limb correction process removes variations in the data due to changes in viewing angle. The limb correction also normalizes the MSU brightness temperatures to a nadir viewing angle and a surface with unit emissivity. Data which have been limb corrected are more closely a measure of the physical temperature of O_2 emission in the viewing area as opposed to a measure of the effect of changing viewing angle. The varying viewing angle of the MSU causes the level where the weighting functions peak to change. The approximate change with zenith angle θ of the pressure level P where the weighting function peaks is given by (Grody, 1983)

$$P(\theta) = P(0°)\sqrt{cos\theta} \tag{4.1}$$

where $P(0°)$ is the level where the weighting function peaks at nadir. For MSU channel 2 , the weighting function peaks at 700 mb at nadir while it peaks at about 520 mb for the maximum zenith angle of 56.6 degrees.

The coefficients used for the limb correction in this study are from the TOVS data base of 1987. These coefficients are occasionally regenerated using either collocated satellite and rawinsonde data or simulated MSU soundings. The limb correction uses the method of Smith *et al.* (1974). The coefficients are obtained from simulated brightness temperature measurements using a set of climatological atmospheres. Koehler (1989) has shown that there is a left to right asymmetry in the MSU limb correction due to an asymmetrical antenna gain function.

4.3 Surface Wind Speed Algorithm

The surface wind speeds used in this study were computed by using the global D-matrix algorithm of Goodberlet *et al.* (1989), with the accuracy flagging and moving average revisions suggested by Petty and Katsaros (1990). The algorithm is statistically derived and is based on a linear regression of four SSM/I channels (1,3,4,5) against coincident buoy observations. The "D" in D-Matrix comes about from the general equation

$$\mathbf{X} = D\mathbf{Y} \tag{4.2}$$

where $\mathbf{X}$ is the matrix of desired quantities, $\mathbf{Y}$ is the matrix of measurements, and D is a matrix relating the observations to the desired quantity.

The global D-matrix is designed to be used at all latitudes and in all seasons over the ocean. Its predecessor, the Hughes Aircraft D-matrix algorithm Goodberlet *et al.* (1989), relied on similar regression techniques but was divided into nine climate and season codes, each having a different set of regression coefficients. The original D-matrix algorithm performed within the 2 m/s rain-free standard deviation prelaunch accuracy specification near the global mean wind speed of 7 m/s but showed scaling and bias errors at higher wind speeds, with the algorithm winds biased low with respect to the buoy winds. The original D-matrix algorithm also had discontinuities in the wind speed field across the climate code boundaries.

Several criteria were used to determine suitable matches between buoy and satellite measurements for D-matrix algorithm development. Only buoys further than 100 km from land were chosen for the comparison in order to ensure that seas were fully developed and also to insure that contamination from land did not enter the antenna side lobes and affect the microwave radiances. The 100 km distance is greater than the half power effective field of view of the lowest resolution 19 GHz SSM/I channels (Table 4.1). SSM/I observations and buoy observations were used in the regression occurred when the SSM/I overpass was within 25 km and 30 minutes of the buoy measurement. Buoy wind speeds, which are actually an 8.5 minute average, are measured at 5 or 10 m above the surface. In order to standardize the elevation of the buoy measurements, the buoy speeds are adjusted to a 19.5 m elevation with insignificant error (Goodberlet *et al.*, 1989) before the regression was performed.

In order to address the problems of the original D-matrix algorithm, the global D-matrix algorithm was developed. The global D-matrix was created from a subset of the data used in the creation of the original D-matrix, with 100 randomly selected observations from each of the 9 climate codes. Only matches with no rain or very light rain were selected, leaving a total of 708 coincident buoy and SSM/I observations to develop the global D-matrix algorithm, with wind speeds ranging up to 20 m/s. A key difference between the development of the global D-matrix and the previous D-matrix algorithm was the use of a regression which was weighted over the global wind speed distribution, which is shown in Figure 4.11 . This had the effect of making all wind speeds equally important in the regression instead of emphasizing those speeds with the greatest natural occurrence. The global D-matrix wind speed regression in meters per second is given by

$$U(m/s) = 1.0969T_{19v} - 0.4555T_{22v} - 1.760T_{37v} + 0.7680T_{37h} + 147.9 \qquad (4.3)$$

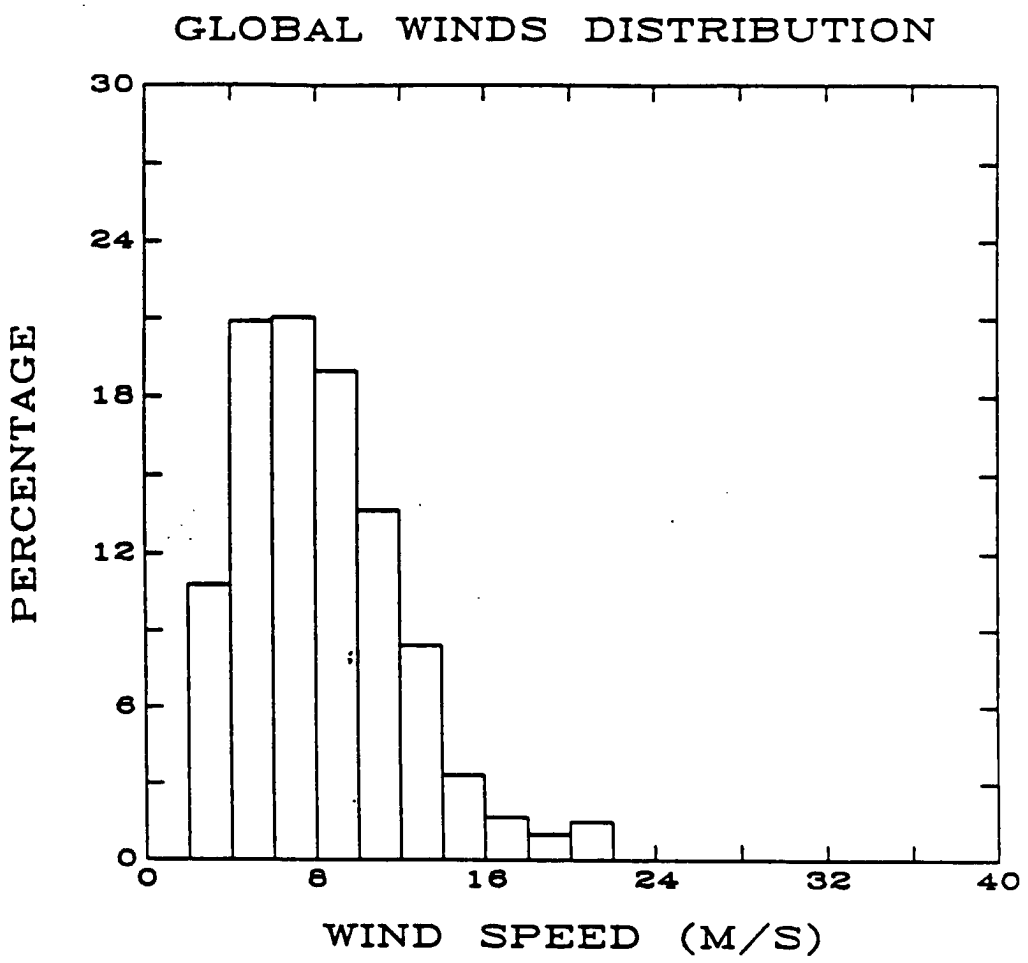

Figure 4.11: The global distribution of ocean surface wind speeds (from Hollinger, 1991).

Accuracy flag	Criteria	Accuracy
0	$T_{37v} - T_{37h} > 50$ and $T_{19h} < 165$	< 2 m/s
1	$T_{37v} - T_{37h} < 50$ or $T_{19h} > 165$ or $T_{19v} > 215$ or $T_{37v} > 221$	2 -5 m/s
2	$T_{37v} - T_{37h} < 37$	5 - 10 m/s
3	$T_{37v} - T_{37h} < 30$	> 10 m/s

Table 4.3: Accuracy flags used for the SSM/I wind speeds.

where the subscripts indicate the frequencies of the SSM/I channels in GHz and their polarization. The observations used in developing the global D-matrix and the regression line are shown in Figure 4.12. The standard deviation and bias of the global D-matrix as a function of buoy wind speed are shown in Figure 4.13. Note that each of these measures are not strong functions of the buoy wind speed.

In order to assess the effect of precipitation on the satellite wind speed retrievals, different rain flags are used. These could also be referred to as accuracy flags since they measure any factor which was statistically shown in the development of the algorithm to degrade the accuracy of the wind speed retrieval beyond the desired 2 m/s standard deviation. The accuracy flags used in this study are shown in Table 4.3. Rain is a major cause of poor global D-matrix performance. The accuracy flags were determined by comparing plots of the standard deviation of global D-matrix wind speeds against some parameter sensitive to precipitation. An example is shown in Figure 4.14, which shows how the standard deviation of global D-matrix winds increases as the difference in brightness temperature between two polarizations at 37 GHz decreases. This makes sense since microwave radiation from precipitation is unpolarized or weakly polarized while radiation from the sea surface is highly polarized. Similar plots can be made for other accuracy flagging criteria , such as absolute brightness temperature at 19 GHz, which increases in the presence of liquid precipitation The accuracy flags have the useful feature that they discriminate between open water and land or ice surfaces, so retrievals are not performed over these surfaces without the need for a land mask.

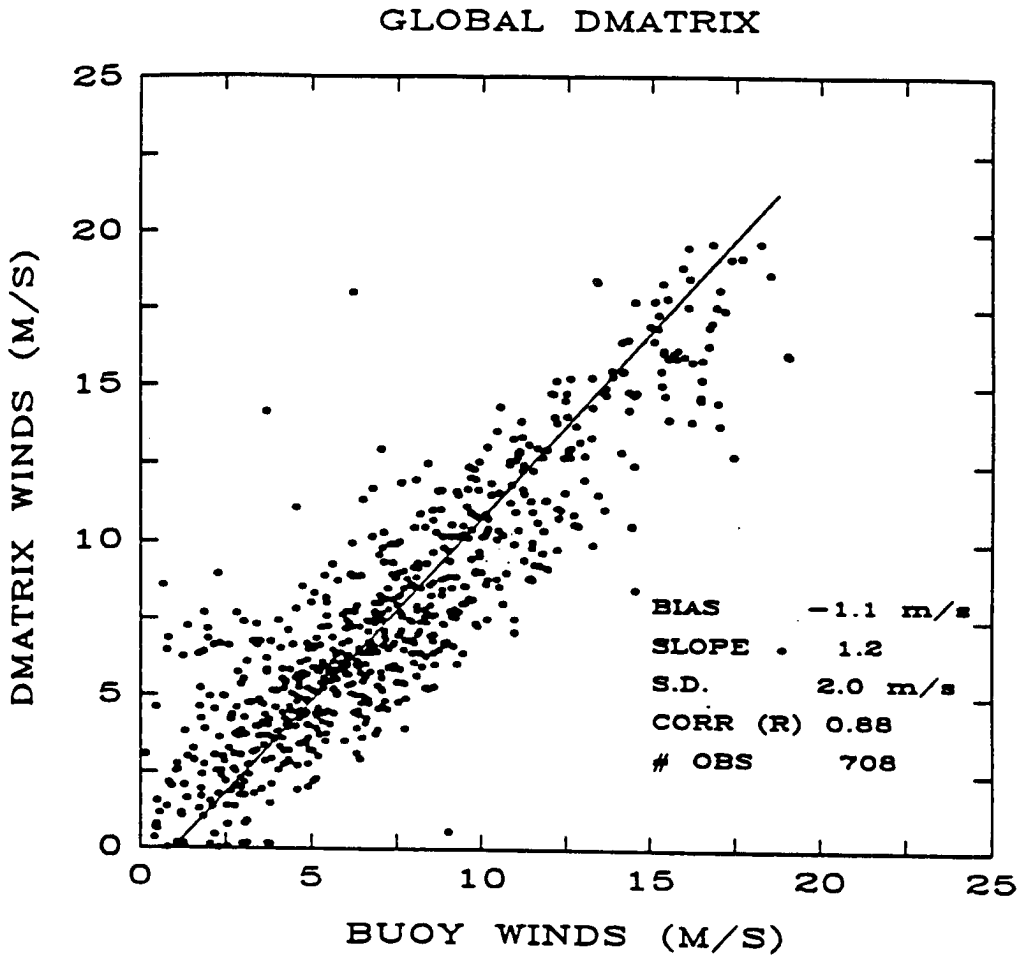

Figure 4.12: Observations used in compiling the global D-matrix algorithm and statistics of the regression (from Hollinger, 1991).

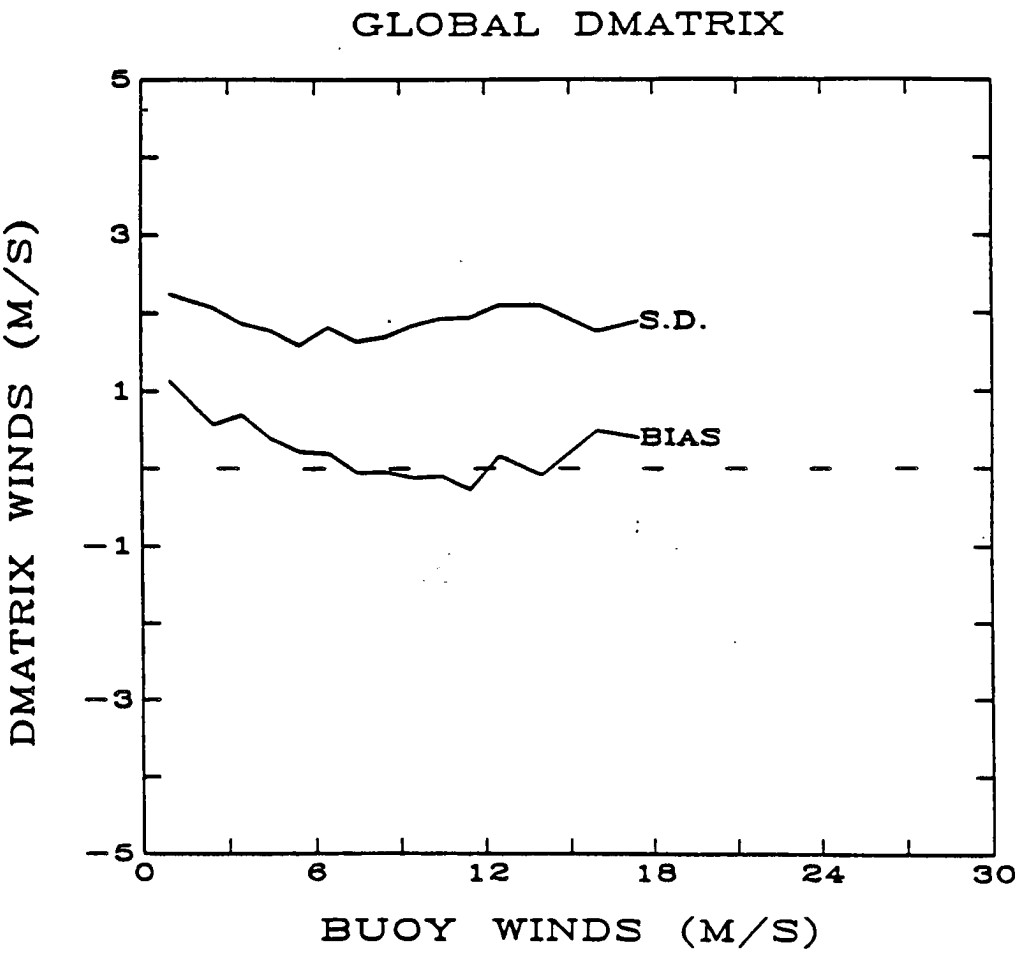

Figure 4.13: Standard deviation and bias of the global D-matrix winds as a function of buoy wind speeds (from Hollinger, 1991).

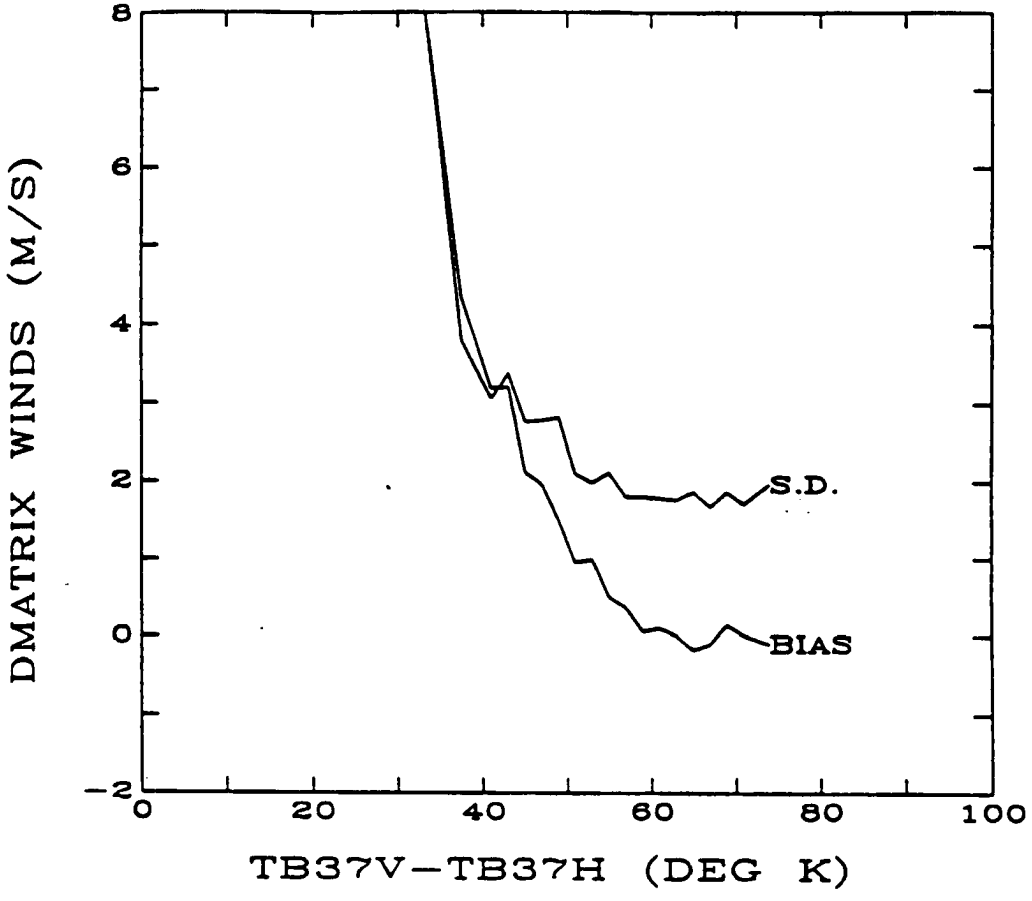

Figure 4.14: Standard deviation and bias of the global D-matrix as a function of the accuracy flag $T_{B37V} - T_{B37H}$ (from Hollinger, 1991).

The wind speeds are computed at 25 km intervals along and across track, corresponding to the sampling rate of the low frequency SSM/I channels. The actual resolution of the wind speeds from the global D-matrix algorithm is less than the 25 km sampling rate since the algorithm makes use of the low resolution 19 GHz channels. Resolution of SSM/I winds is not sufficient for resolving the inner areas of tropical cyclones and polar lows, since it is likely that gradients in the wind speed exist on a smaller scale than instrument resolution (Goodberlet *et al.*, 1989). Alternative surface wind speed algorithms for the SSM/I based on a physical model, one of which uses only the higher resolution 37 GHz channels, have been proposed by Schluessel and Luthardt (1991). Algorithms using other channels from the SSM/I were also developed at the same time as the global D-matrix, but the global D-matrix had the lowest standard deviation of 2 m/s (Goodberlet *et al.*, 1989). These alternate algorithms could be useful if a channel fails on the SSM/I.

Wind speed is not returned in pixels along and cross track from any accuracy flagged pixels, in accordance with Petty and Katsaros (1990). A 3 x 3 moving average is used to smooth the retrieved values, except for pixels along the edge of the scan and those bordering flagged areas, where the raw value is returned. With the deletion of pixels bordering flagged areas and 3 x 3 averaging, the values returned should be reliable.

4.3.1 Validation

A few recent studies have verified the global D-matrix wind speeds against surface wind speed observations or other satellite wind speed observations.

Schluessel and Luthardt (1991) worked on developing a regression type wind speed algorithm for the SSM/I. They used simulated radiances, which were derived from simulated atmospheric conditions and wind speeds. Their results were then compared to over 30,000 surface wind speed observations from the dense observing network over the North Sea. Their algorithm had a 1.4 m/s standard deviation.

They also compared wind speeds retrieved from the global D-matrix used in this study and determined a 2 m/s standard deviation and negligible bias. This reinforces the original accuracy specification of the global D-matrix algorithm.

Mognard and Katsaros (1992) compared global D-matrix wind speeds to those obtained from the GEOSAT satellite altimeter. The GEOSAT wind speeds are reported to have a 0.5 m/s low bias and a standard deviation of 1.6 m/s compared to buoy winds. The GEOSAT winds were averaged over 4 seconds to make the footprint size comparable to that of the SSM/I, and only those observations less than two hours apart were used in the comparison. The results of their global data set are shown in Figure 4.15. Note that the standard deviation between SSM/I and GEOSAT is almost the same as that between the SSM/I and the buoy data set. In fact, in precipitation free conditions the agreement between the sensors is better than the agreement of either of the satellite derived wind speeds with the buoy data, a reflection of the difference between point measurements and areally averaged measurements.

Holliday and North (1992) have reported a negative bias of 0.9 to 1.5 m/s in the global D-matrix algorithm winds at wind speeds above 16 m/s , with the satellite winds possibly 20% less than winds measured from ships. They attribute the bias to the lack of precipitation free high wind speeds in the development of the global D-matrix algorithm.

4.4 Processing of Satellite Data

Polar low cases were selected from 1989 in the Labrador Sea and Davis Strait area. The dates and locations of the cases were obtained from Erik Rasmussen while he was a visiting scientist at the Cooperative Institute for Research in the Atmosphere (CIRA), and from the climatology in Parker and Hudson (1991). SSM/I and MSU data were acquired through CIRA under a cooperative agreement with the National Environmental Satellite, Data, and Information Service (NESDIS). The

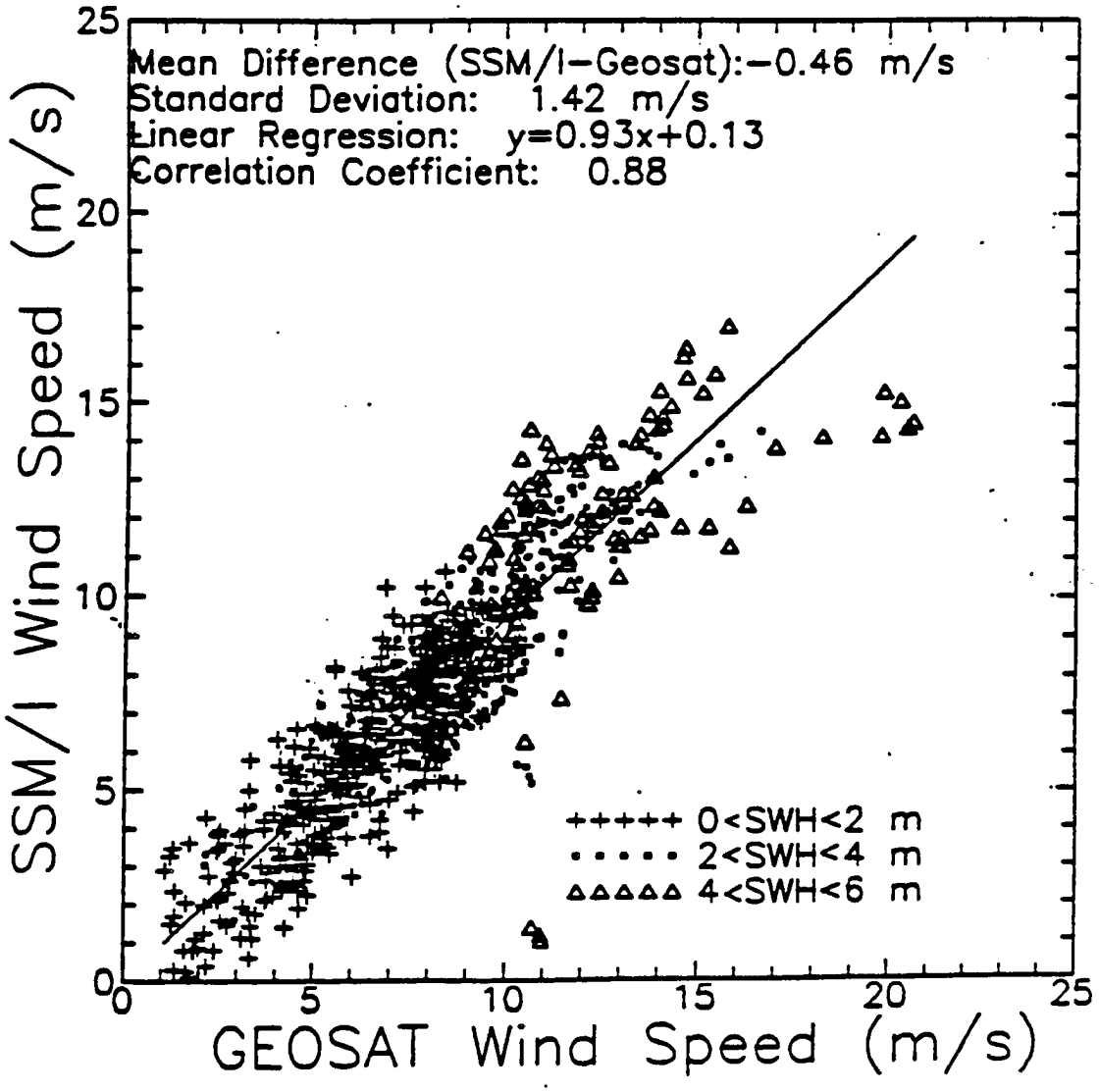

Figure 4.15: Scatter diagram of SSM/I wind speeds from the global D-matrix algorithm versus wind speeds from the GEOSAT altimeter. Statistics of the regression are also shown. Points are plotted for three significant wave heights (from Mognard and Katsaros, 1992).

SSM/I data was on 9-track 6250 BPI tapes produced for NESDIS by Remote Sensing Systems with data from up to 56 orbits on each tape. Antenna temperatures were converted to brightness temperatures with software supplied by Remote Sensing Systems. MSU level 1B data was on 9-track 6250 BPI tapes in a format described by Kidwell (1988). Surface and upper air maps for the cases were obtained from the National Center for Atmospheric Research (NCAR).

The SSM/I and MSU data were reformatted into the generalized data format described in Jones and Vonder Haar (1992). Data from the generalized data format for both sensors were remapped into images in a stereographic projection with the PORTAL software described in Jones and Vonder Haar (1992). The generalized data format greatly simplified manipulation and display of data from two different sensors through the use of common remapping programs. Data processing was performed on CIRA's Local Area Network. A VAX 4000 was used for reformatting and remapping operations, with display on a DEC X-Windows workstation.

Infrared data was obtained from the National Snow and Ice Data Center as 5.4 km resolution composite imagery on plastic sheets. This data was useful for determining the location of the polar lows and tracking their movement through time. Data in this form has been used previously for polar low climatologies (*e.g.* Carleton and Carpenter (1989)).

4.4.1 Navigation of Satellite Data

There have been some minor navigation problems with the SSM/I data (Hollinger, 1991). The data from 1989 used in this study had a spacecraft yaw correction of +0.5° applied (Remote Sensing Systems, 1989). The accuracy of the navigation is about 15 km or one 85 GHz pixel. This was verified for the cases studied by comparing gridded coastline data to the the 85 GHz horizontally polarized channel, which due to the large emissivity contrast between open water and land or ice has a large brightness temperature response across coastlines. In all of the

cases used in this study, the navigation appeared to be consistently within the error budget.

The MSU data was navigated with latitudes and longitudes supplied with the level 1B data. Due to the low resolution of the MSU data, navigation accuracy can only be crudely determined. A crude check of the navigation over the case study area was possible due to the depressed brightness temperatures in Channels 1 and 2 observed over the elevated ice cap of Greenland, which matched up well with the map overlay.

4.5 Temperature Anomaly and Averaged Wind Speed Computations

4.5.1 Wind Speed

In order to determine the radial distribution of wind speeds around the polar lows, SSM/I wind speeds were averaged around each polar low at approximately 50 km intervals, as measured outward from the center of the polar low. Four observations at a common distance from the center were averaged to determine an average value of wind speed and remove motion effects. This averaged wind speed assumes a symmetric wind field for the case of no storm motion. As most accuracy flagged regions were located over the polar lows, the closest distance to the center at which a radially averaged wind speed could be determined was variable. The center of the polar low was determined either with the infrared imagery when the time agreement was within two hours or with the SSM/I channel 7 data, which responded to the deep cloud bands around some of the polar lows.

4.5.2 MSU Brightness Temperature

Following the approach of Kidder *et al.* (1978) and Velden and Smith (1983) for tropical cyclones, it was desirable to determine the temperature difference of the satellite sounding over the polar low versus the ambient environmental temperature. In previous tropical cyclone studies, ambient temperature was defined as the average

temperature at 4° to 10° of latitude radius from the center or that at a 6° of latitude radius. Due to the frequent occurrence occurrence of polar lows near ice or land areas, some of which were significantly elevated like Greenland, and the need to use MSU channel 2, soundings which were not over water were not used to determine the radial average. The location of the polar low was determined from infrared imagery or 85 GHz imagery. An infrared image at the time of the MSU observation from the Advanced Very High Resolution Radiometer, which is aboard the same NOAA satellite as the MSU, would have made this task more precise but due to the low resolution of the MSU precise centering was not required. Two anomalies were determined over each polar low, ΔT_2 and ΔT_2. ΔT_1 was defined as the difference in limb corrected MSU 2 brightness temperature over the center versus the up to eight adjacent MSU temperatures which were over water. ΔT_2 was defined as the difference in limb corrected MSU 2 brightness temperature over the center versus the up to 16 MSU temperatures in the next closest ring of soundings to the storm center. An exception was that brightness temperatures from the extreme ends of the scan, at scan position 1 and 11, were not used due to large limb correction effects and poor resolution. A schematic example of the method used to compute the ΔT_1 and ΔT_2 brightness temperature anomalies is given in Figure 4.16. Due to the variable resolution of the MSU scan spots and the variable position of the polar low in the scan pattern, the distance from the temperature sounding nearest to the polar low to that defined as the environmental temperature varied.

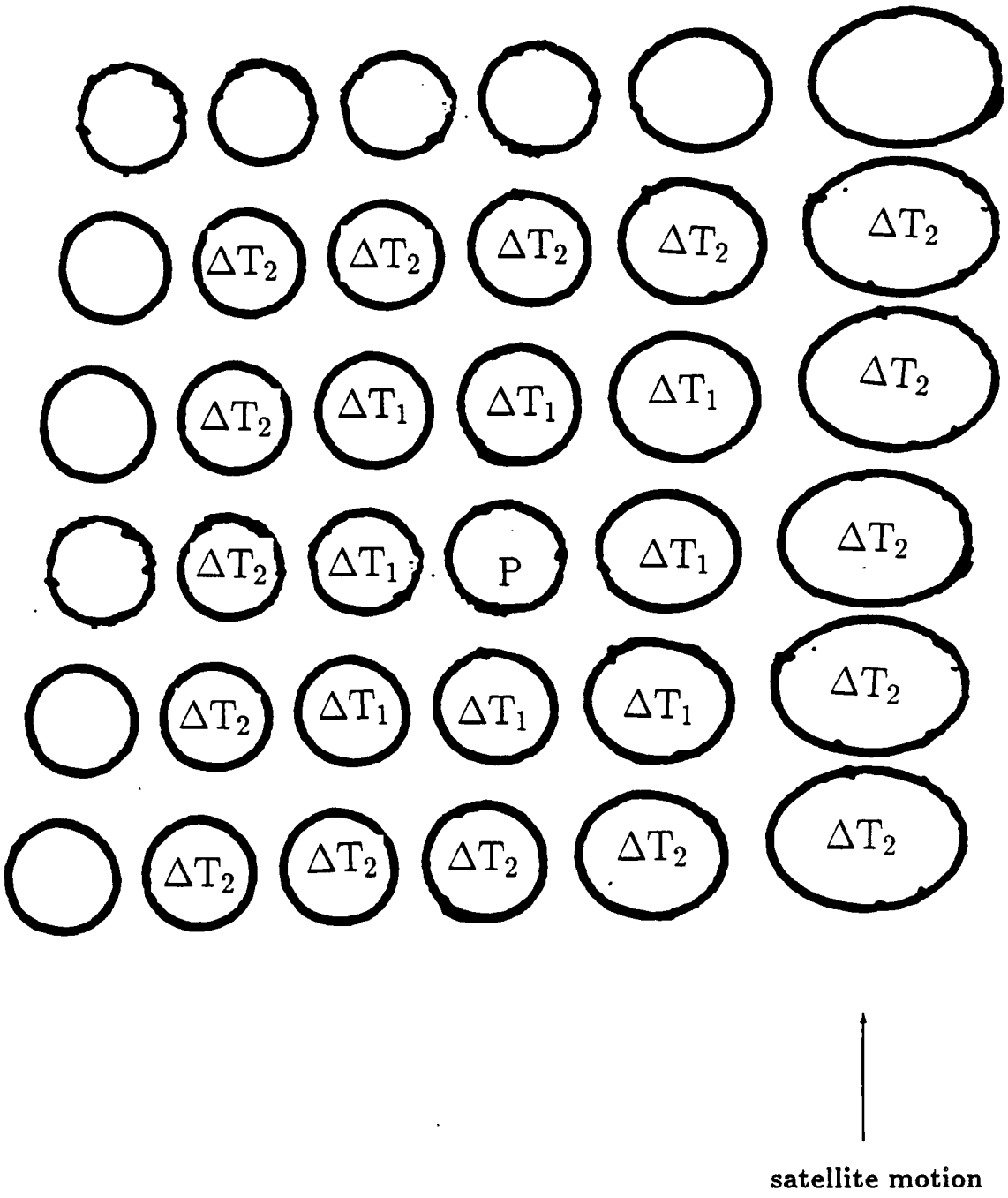

Figure 4.16: Schematic diagram showing the MSU scan spots used to calculate the ΔT_1 and ΔT_2 temperature anomalies.

Chapter 5

DATA ANALYSIS

A total of four cases were studied through the use of SSM/I and MSU measurements. The cases were from the Labrador Sea from the winter of 1989. This area was chosen due to a recent listing of polar low occurrence for the area from Parker and Hudson (1991) as well as personal communication from Erik Rasmussen while he was a visiting scientist at CIRA in 1991. The dates of the cases are:

January 2, 1989

January 11, 1989

January 17 - 18, 1989

March 20, 1989

Each case will be presented with an infrared satellite image, surface wind speed image from the SSM/I, and MSU channel 2 brightness temperature image. Sources of error in the microwave data will be discussed. The wind speed and brightness temperature anomalies will then be compared. Finally, the data will be interpreted in terms of polar low theory and its applicability to analysis of polar lows.

5.1 Data Presentation

5.1.1 Infrared Imagery and Synoptic Data

The four cases can be broken into two groups: spiraliform polar lows (January 2 and January 18) and comma clouds (January 11 and March 20) . This follows the satellite imagery classification scheme developed by Forbes and Lottes (1985).

Infrared satellite images are presented in Figures 5.1 to 5.4 for the January 2, January 11, January 18, and March 20 cases of 1989, respectively. The January 11 and March 20 cases are similar in appearance and position of occurrence.

Sample surface and 500 mb analyses for the two polar lows shown in Figures 5.3 and 5.4 are given in Figure 5.5 and Figure 5.6. The time of the surface observation was chosen to be close to the overpass time of the DMSP satellite, which passes over the Labrador Sea area at approximately 2300 and 0900 UTC. Note the lack of observations over the Labrador Sea. Satellite data appears to be the only way to determine if a polar low exists in this region.

5.1.2 Surface Wind Speed

Surface wind speeds for the cases are shown in Figures 5.7 through 5.10. All images are contoured at 2 m/s intervals, the value of the standard deviation of the algorithm used to compute the wind speeds. The black areas indicate regions in which no values were returned due to accuracy flagging. These flags detect the ice boundary as well, as verified by a comparison to infrared imagery. Although there is no surface wind data with which to compare the SSM/I wind speeds, the structure of the fields looks reasonable. Each case shows the expected stronger wind speeds on the right hand side of the storm, as viewed looking in the direction of storm motion. The direction of movement of each polar low was generally towards the southeast, as determined by comparing several times of infrared satellite images.

The March 20 case indicates an advantage of wind speeds retrieved from the SSM/I in the polar regions. In this case, wind speeds over the entire storm can be determined without missing areas due to accuracy flagging. This is in contrast to studies using this instrument for tropical cyclone research, which have reported poor results due to heavy liquid precipitation (Rappaport and Black, 1989).

An indication that the fields returned as surface wind speed around polar lows are really a measure of surface wind speed can be seen from a case from October,

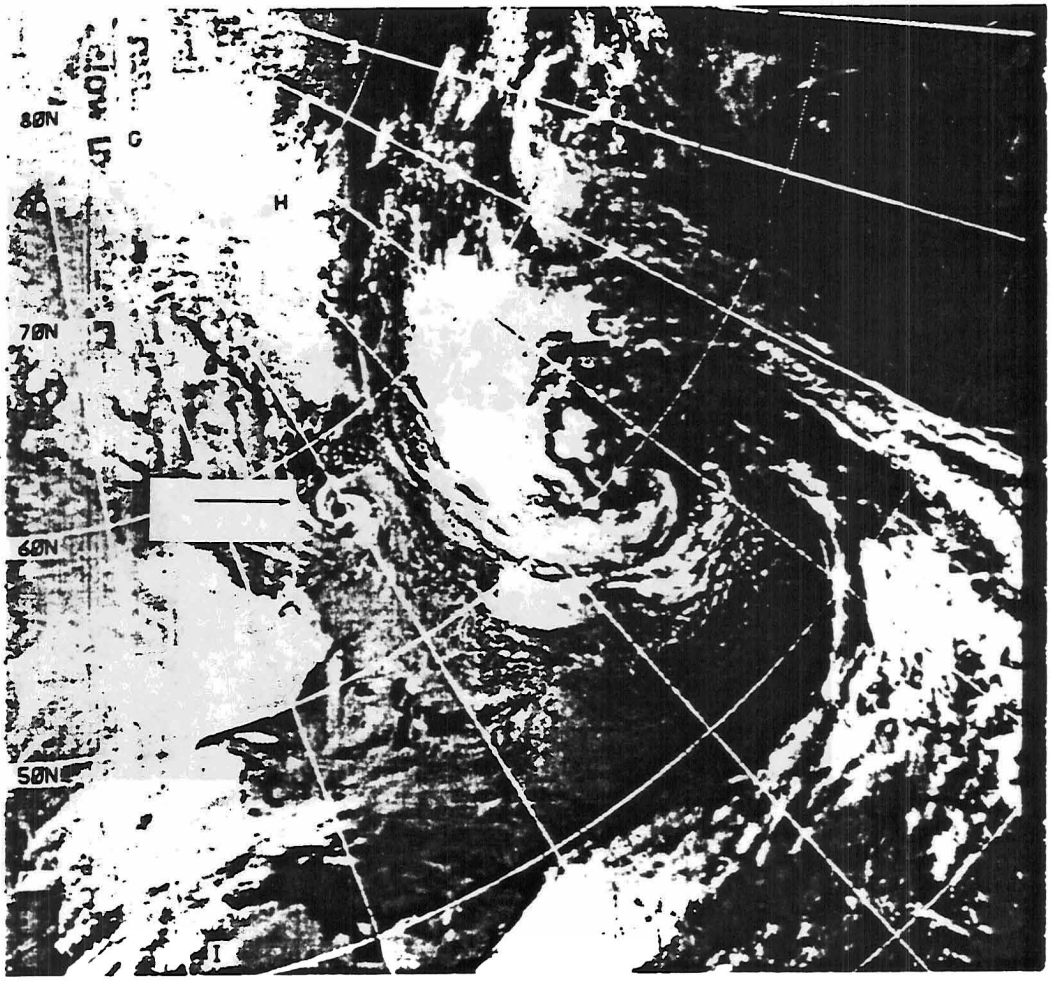

Figure 5.1: DMSP infrared composite image for Jan. 2, 1989 at 1145 UTC. Note the polar low with the well developed "eye" near 57°N and 50°W, poleward of the cyclone to the east.

Figure 5.2: GOES infrared image for Jan. 11, 1989 at 2200 UTC of polar low between Greenland and Labrador (from Rasmussen and Purdom, 1992).

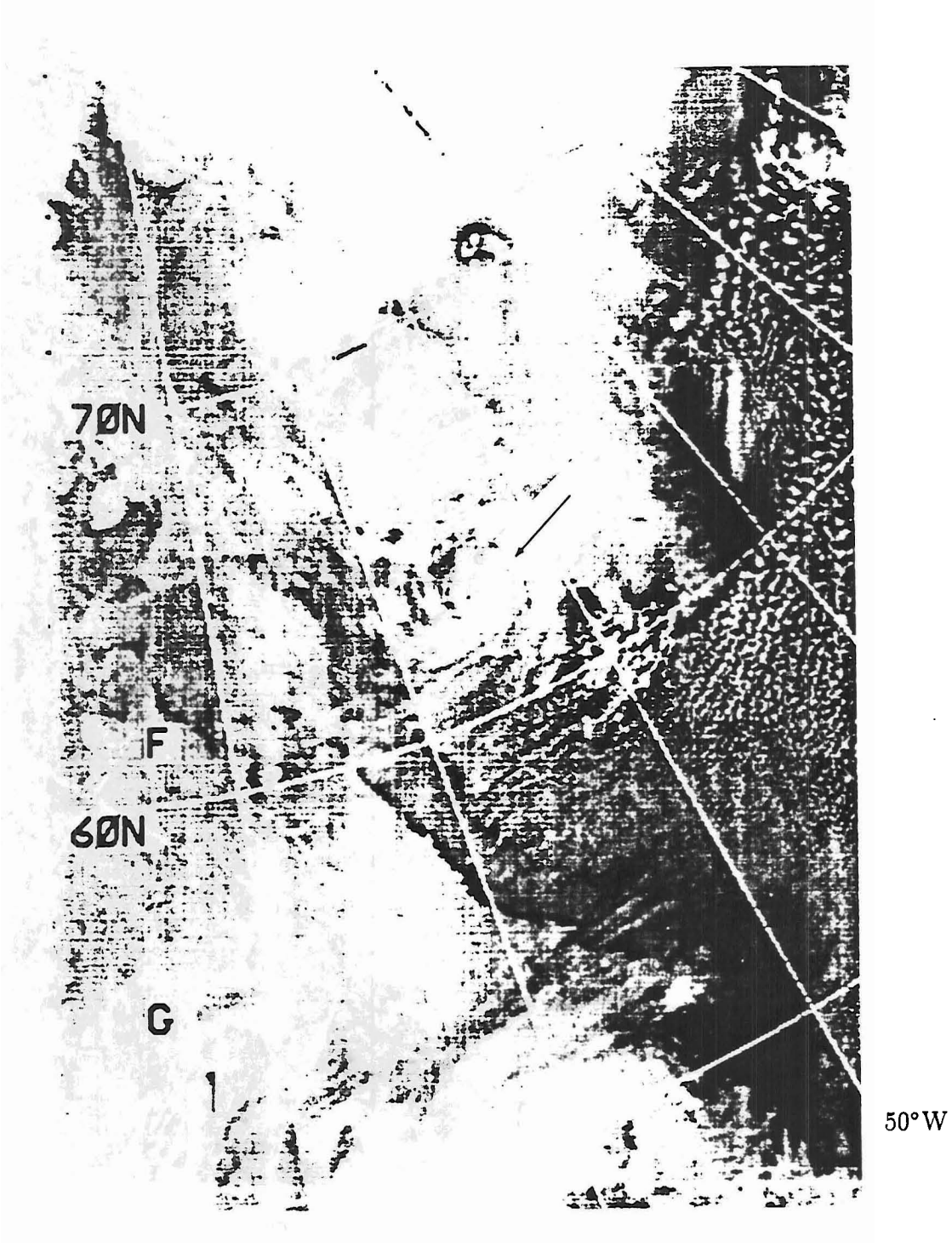

Figure 5.3: DMSP infrared composite image for Jan. 18, 1989 at 1145 UTC. The polar low is near 63°N and 55°W with an "eye" and distinct spiral shape.

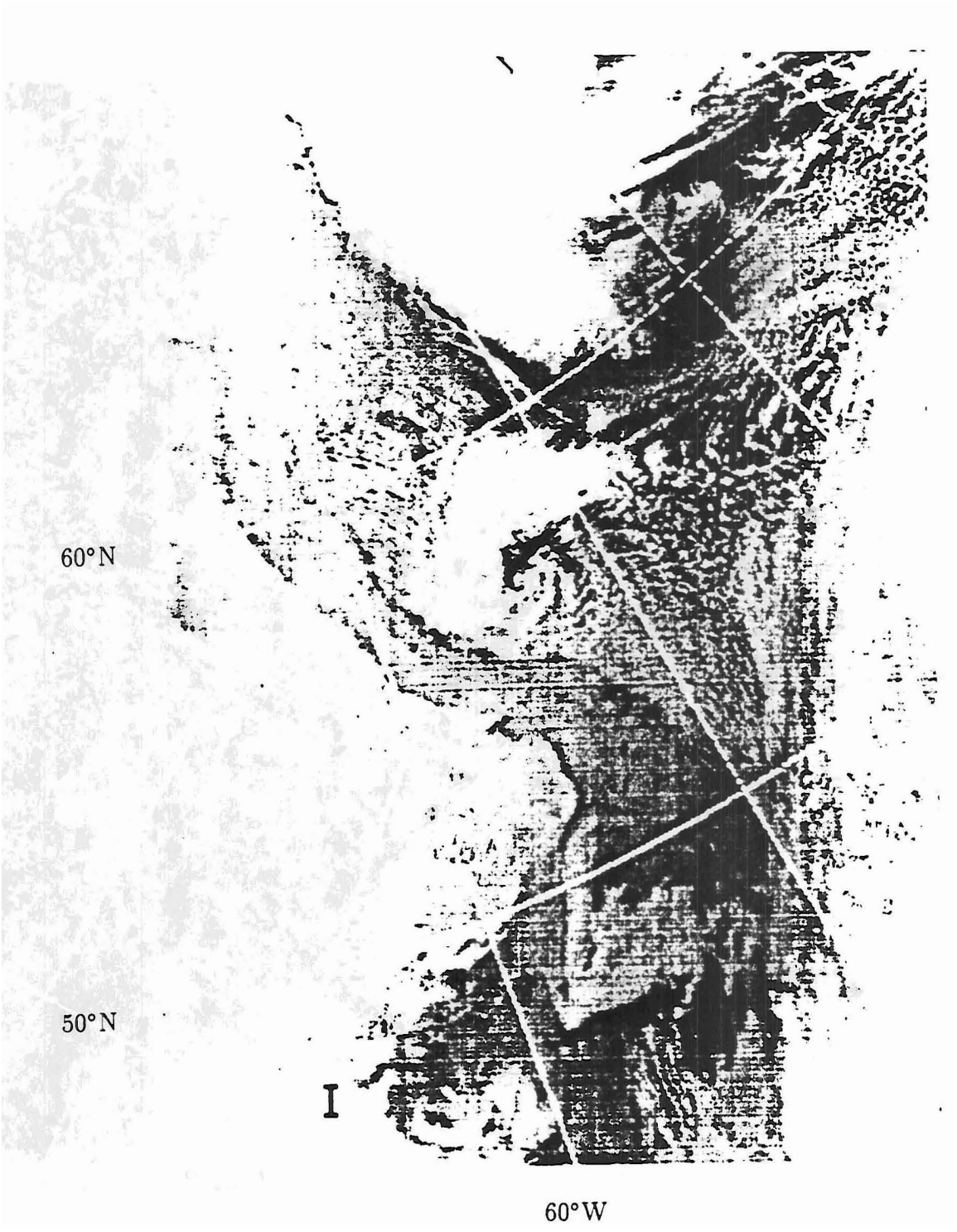

Figure 5.4: DMSP infrared composite for Mar. 20, 1989 at 1145 UTC. Note the similarity in position and appearance between this polar low and the January 11 case.

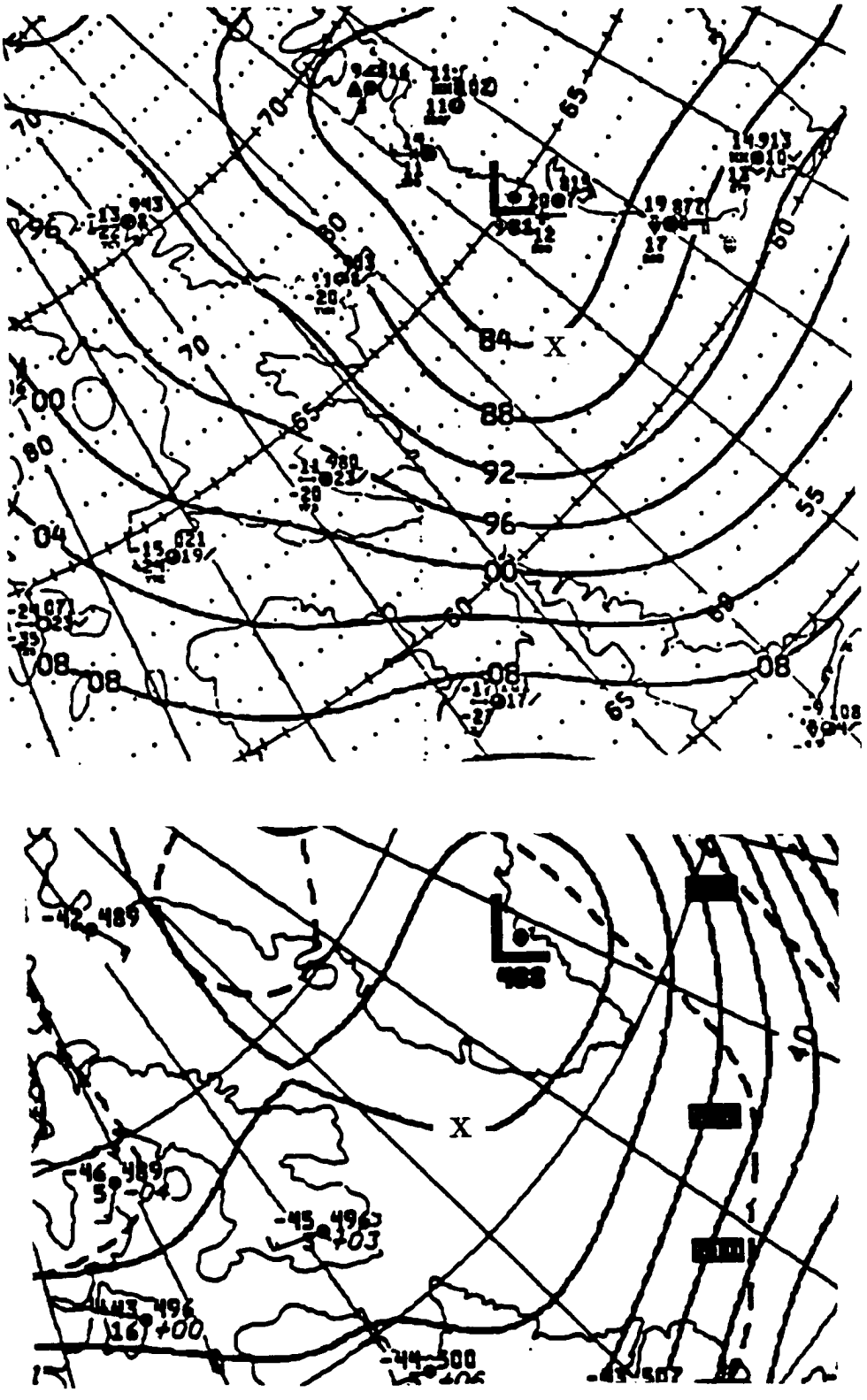

Figure 5.5: Top: Surface analysis on January 18, 1989 at 0900 UTC. Bottom: 500 mb analysis on January 18, 1989 at 1200 UTC. Center of the polar low for each time as determined from satellite imagery is shown by an 'X'.

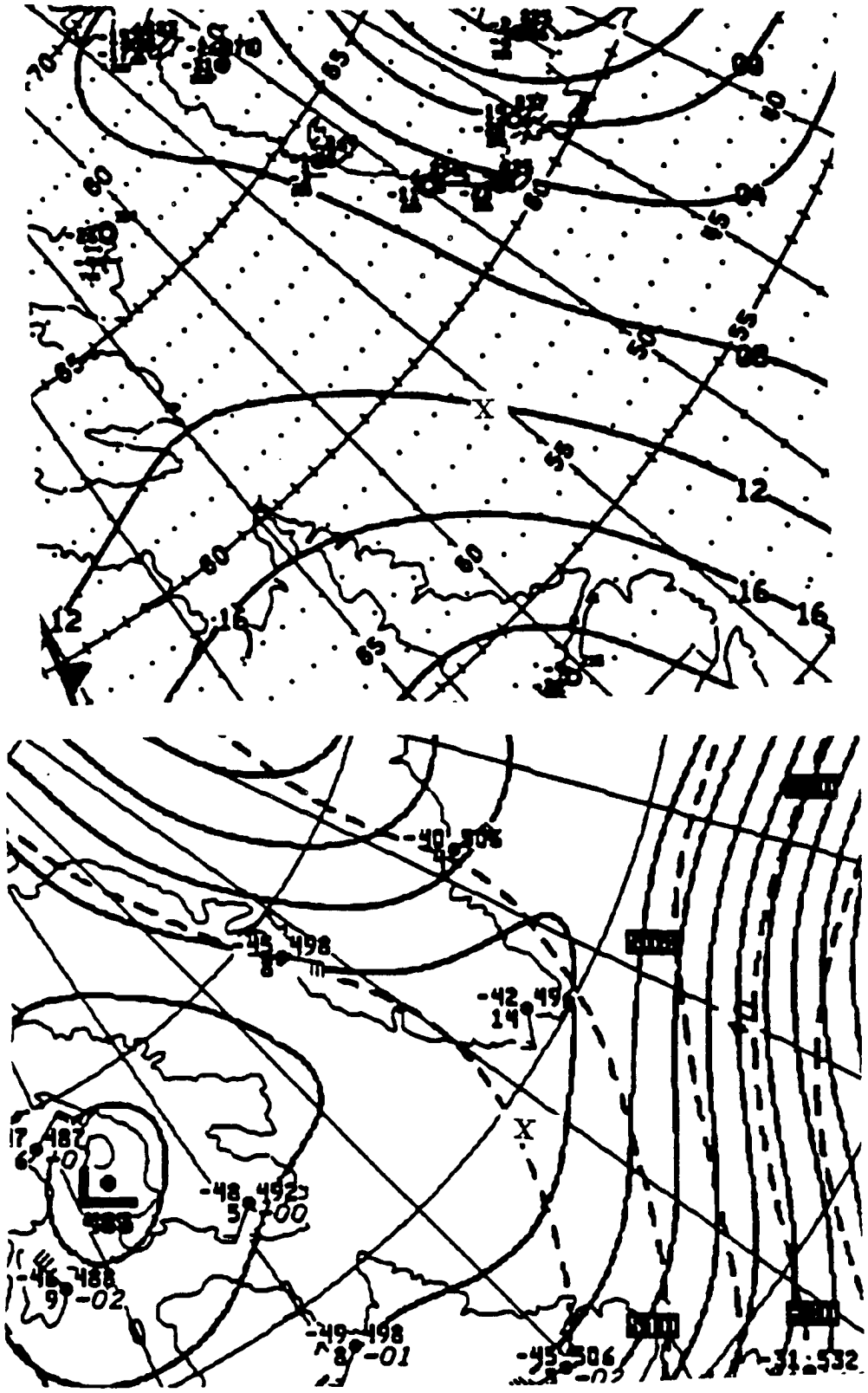

Figure 5.6: Top: Surface analysis on March 20, 1989 at 0900 UTC. Bottom: 500 mb analysis on March 20, 1989 at 1200 UTC. Center of the polar low for each time as determined from satellite imagery is shown by an 'X'.

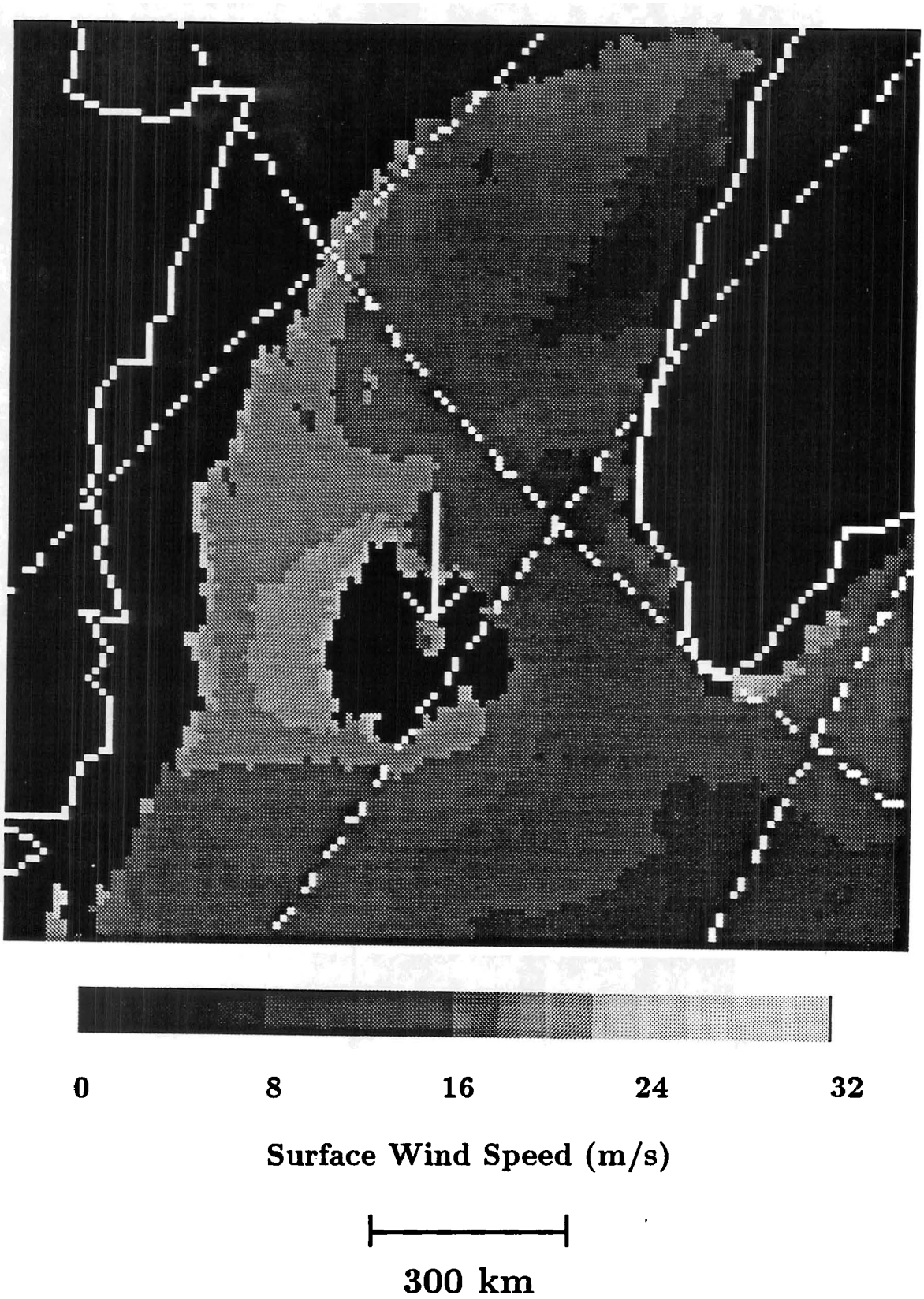

Figure 5.7: SSM/I surface wind speeds for January 2, 1989 at 0824 UTC. Polar low position is indicated by an arrow. Note the precipitation flagged area around the polar low and the area of wind speeds retrieved in the large eye of the storm.

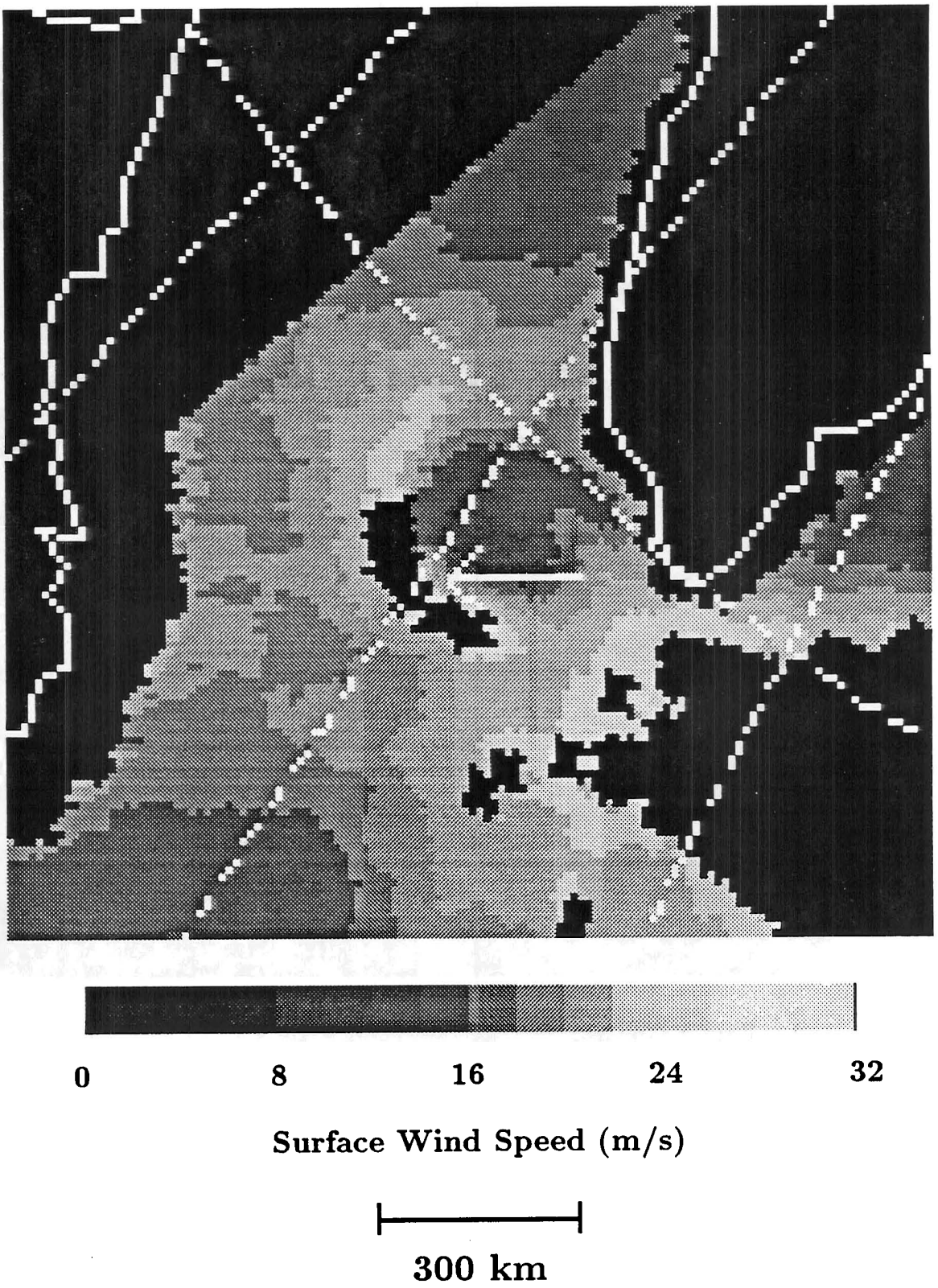

Figure 5.8: SSM/I surface wind speeds for January 11, 1989 at 2204 UTC. Polar low position is indicated by an arrow. Note the strong wind speed gradient across the polar low due to the effect of storm motion.

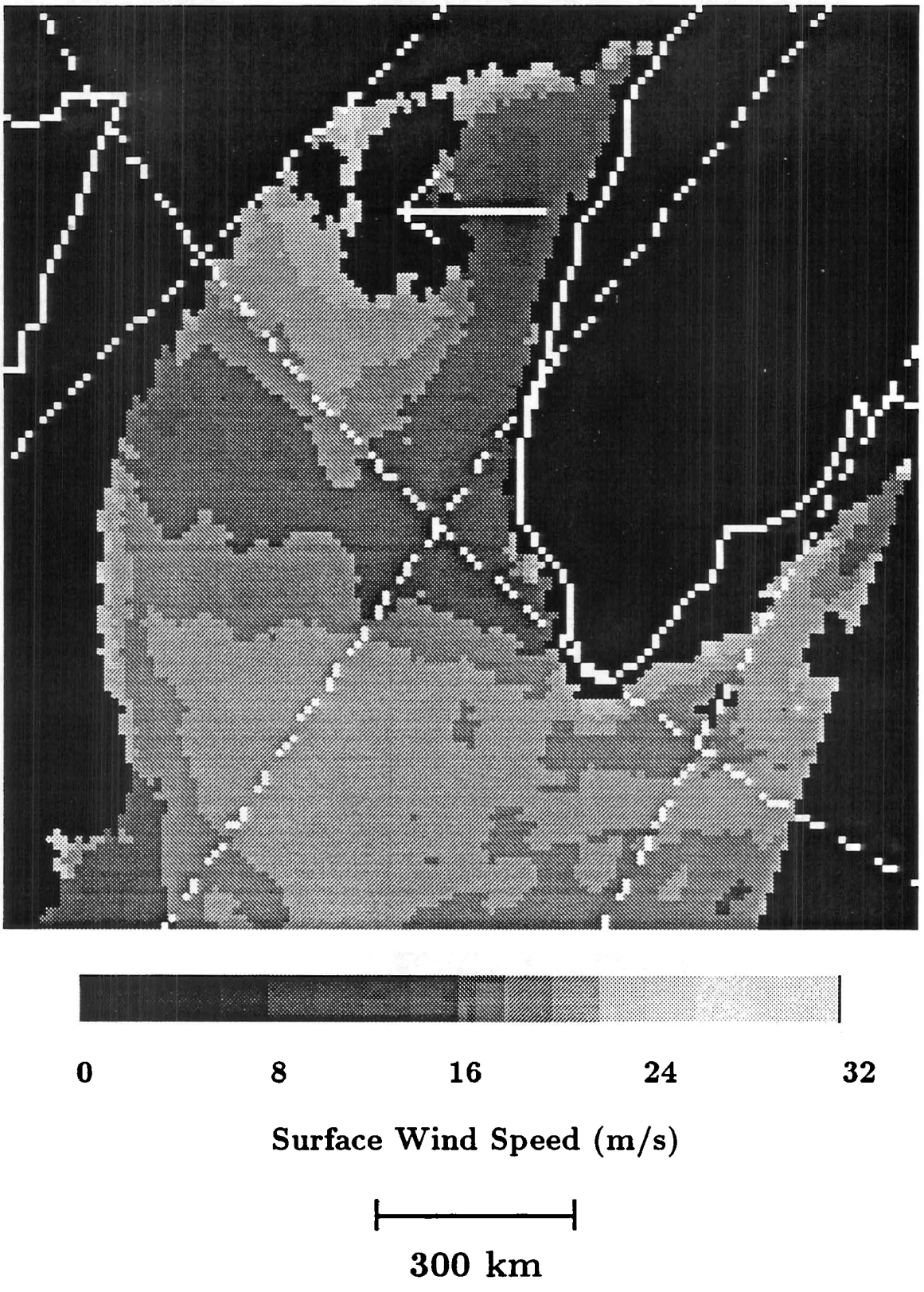

Figure 5.9: SSM/I surface wind speeds for January 18, 1989 at 0829 UTC. Polar low position is indicated by an arrow. The crescent shaped black area is precipitation flagged.

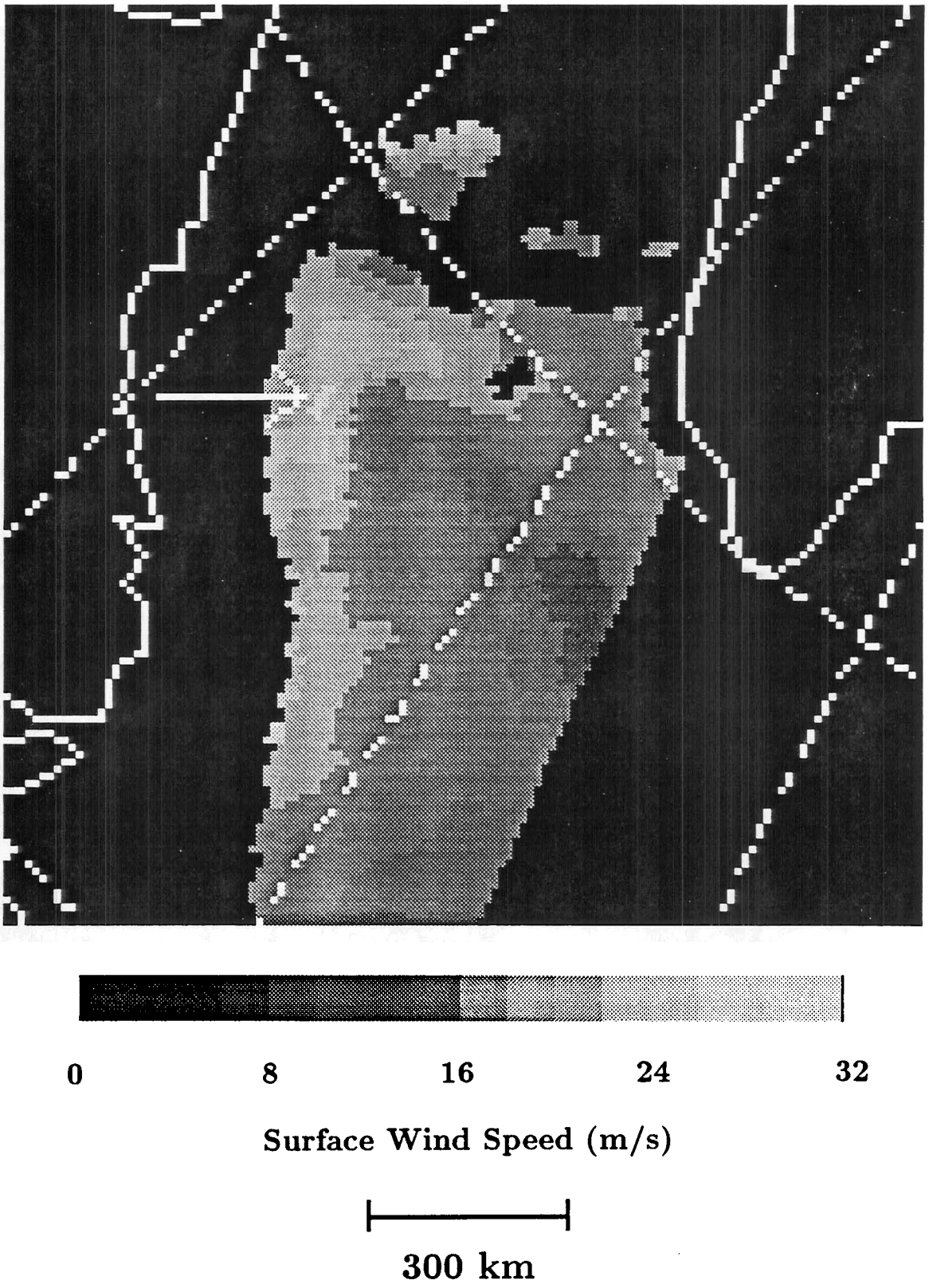

Figure 5.10: SSM/I surface wind speeds for March 20, 1989 at 0911 UTC. Polar low position is indicated by an arrow. Note the asymmetry in the wind field and the lack of precipitation flagging.

1987. There was a ship report of 45 knot winds at 0900 UTC in the Hudson Strait (Hudson and Parker, 1991) . SSM/I wind speeds from the same time show an area of 18 to 20 m/s wind speeds in the same area, in good accordance with the 45 knot value considering the low bias of SSM/I winds at speeds greater than 16 m/s (Holliday and North, 1992).

5.1.3 MSU 53.74 GHz Data

Limb corrected MSU channel 2 53.74 GHz data from the *NOAA-10* and *NOAA-11* satellites for the four polar low cases is presented in this section. MSU channel 1 and channel 3 imagery was examined as well. While these channels would be useful in a retrieval of temperature profiles, only channel 2 is considered here. Channel 3 imagery was rather homogeneous and in polar regions receives much of its signal from the stratosphere, making interpretation of tropospheric features difficult. Channel 1 does have some lower tropospheric temperature signal but is affected by hydrometeors and surface variations to a greater extent than channel 2. The presence of ice in close proximity to the polar low location makes channel 1 especially difficult to use in polar low research. For instance, an attempt was made to compute channel 1 brightness temperature anomalies as a way of obtaining information on possible cloud warming effects around the polar lows. The presence of ice contamination made it very difficult to obtain an environmental temperature value and compute any kind of anomaly with channel 1.

Selected limb corrected MSU 2 brightness temperature fields for three of the four cases listed previously are shown in Figures 5.11 through 5.13. An important feature of the MSU 2 data for this study is the presence of isolated warming over two of the four polar lows, January 2 and January 18. It is worthwhile to note that isolated warming was also seen in the non limb corrected fields for these cases as well. An example of the warming over the January 18 polar low is seen in Figure 5.14. The limb corrected and and raw data are shown for a cross section along MSU scan

position 8. All soundings were over a water surface, so the difference between the raw and the limb corrected data is just a constant offset. The fact that the warming is present over in the raw as well as the limb corrected data shows that the isolated warm soundings in this study are not caused by effects from the other MSU channels which enter through the limb correction process.

The presence of an isolated warm core over a polar low has previously been detected with TOVS observations (Steffensen and Rasmussen, 1986). For the other two cases, a strong temperature gradient exists across the polar low. This is in agreement with the conceptual model of a type of polar low given in Figure 2.4.

Figure 5.15 illustrates the correspondence of the polar low position and the isolated warm core indicated by MSU 2. The time difference between these two observations is less than 2 hours. The deep convection associated with the polar low is clearly indicated by the curved feature in the 85 GHz horizontally polarized imagery. The warmest sounding in MSU 2 corresponds to the center of the polar low as determined from 85 GHz data.

An additional example of the appearance of the warm areas in MSU 53.74 GHz is given in Figure 5.16, where contoured limb corrected brightness temperatures are presented. A polar low with an isolated warm core persisted along the ice edge in the Labrador Sea for over 24 hours. The low is indicated by the arrow in each panel of Figure 5.16.

While the microwave imagery presented in this section does not give an exhaustive look at its use for monitoring polar lows, it does suggest several possibilities. The ability to detect the outer circulation around a polar low with the SSM/I and get some idea of the storms pressure deficit through temperature sounding would be a useful new source of information about these storms. The remainder of this chapter will examine results from this data in more detail along with some sources of error.

227 230 233 236

MSU 53.74 GHz Brightness Temperature (K)

300 km

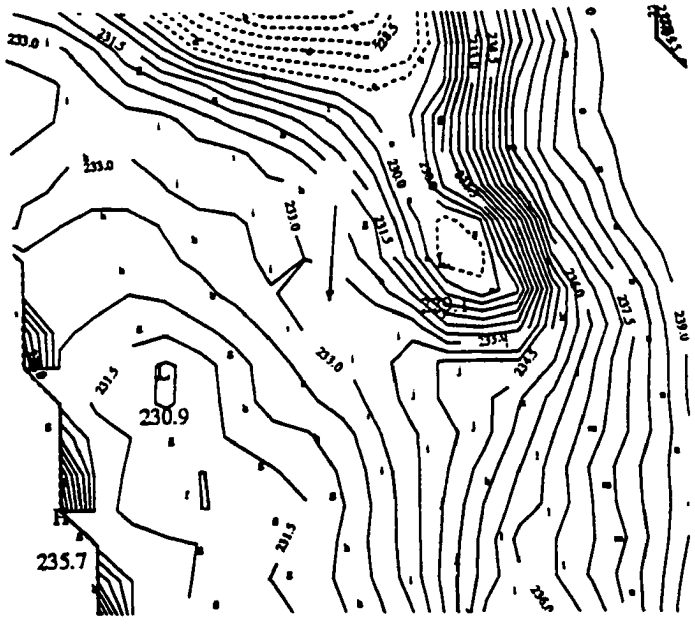

Figure 5.11: MSU 53.74 GHz limb corrected brightness temperatures for January 11, 1989 at 2155 UTC, shown in imagery (top) and contour plot (bottom) form. Polar low position is indicated by an arrow in each. Contours less than 230 K dashed. MSU scan spots shown by small letters. The polar low lies poleward of the main baroclinic zone.

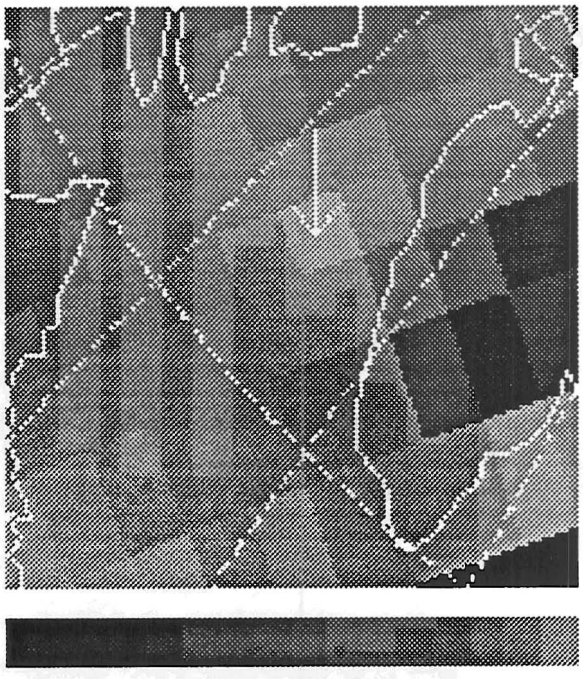

227 230 233 236

MSU 53.74 GHz Brightness Temperature (K)

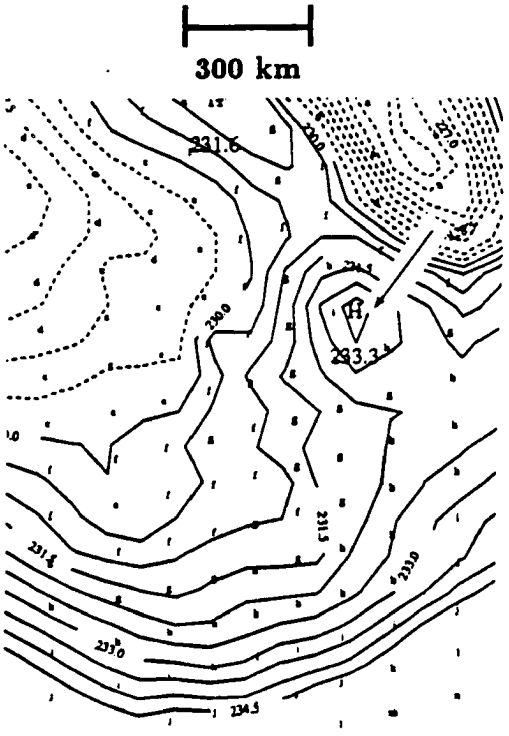

Figure 5.12: MSU 53.74 GHz limb corrected brightness temperatures for January 18, 1989 at 1250 UTC, shown in imagery (top) and contour plot (bottom) form. Polar low position is indicated by an arrow in each. Contours less than 230 K dashed. MSU scan spots shown by small letters. Note the isolated warmer area over the polar low.

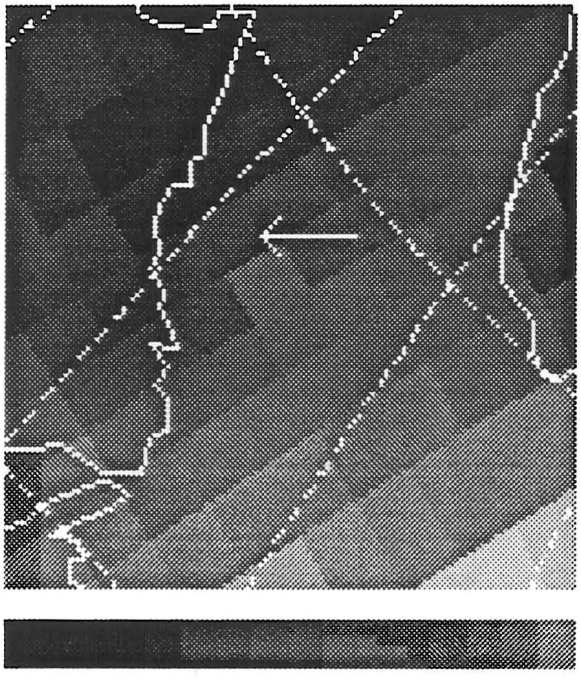

227 230 233 236

MSU 53.74 GHz Brightness Temperature (K)

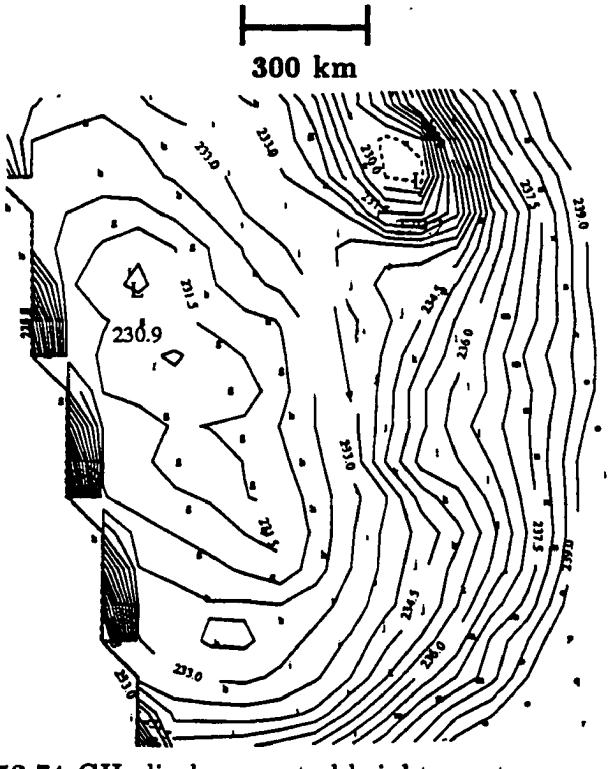

Figure 5.13: MSU 53.74 GHz limb corrected brightness temperatures for March 20, 1989 at 1207 UTC, shown in imagery (top) and contour plot (bottom) form. Polar low position is indicated by an arrow in each. Contours less than 230 K dashed. MSU scan spots shown by small letters. Note the temperature gradient near the polar low.

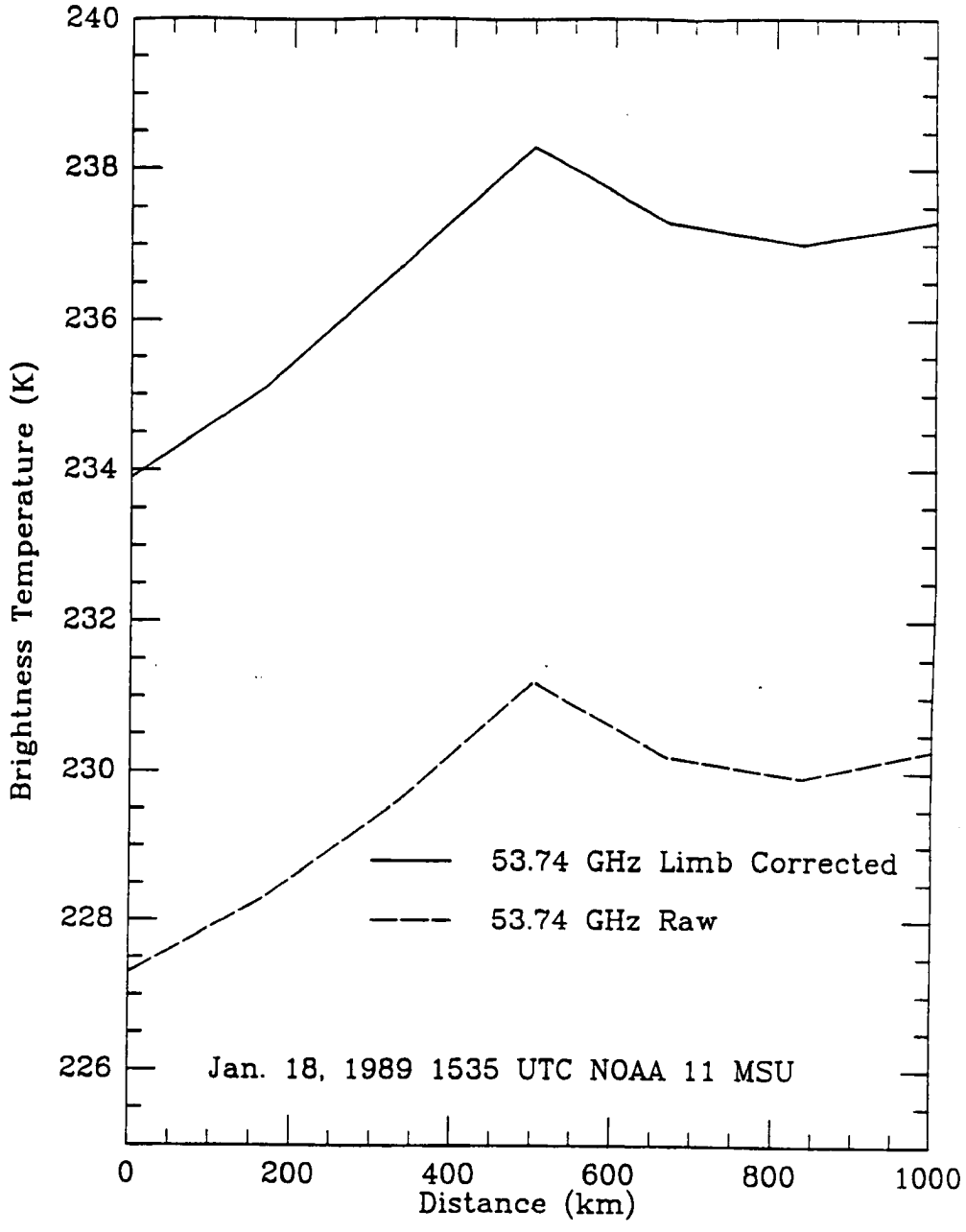

Figure 5.14: Cross section along the satellite track at MSU scan position 8 showing the warming over a polar low centered at the 500 km position. Raw and limb corrected values are shown. The soundings are over a water surface.

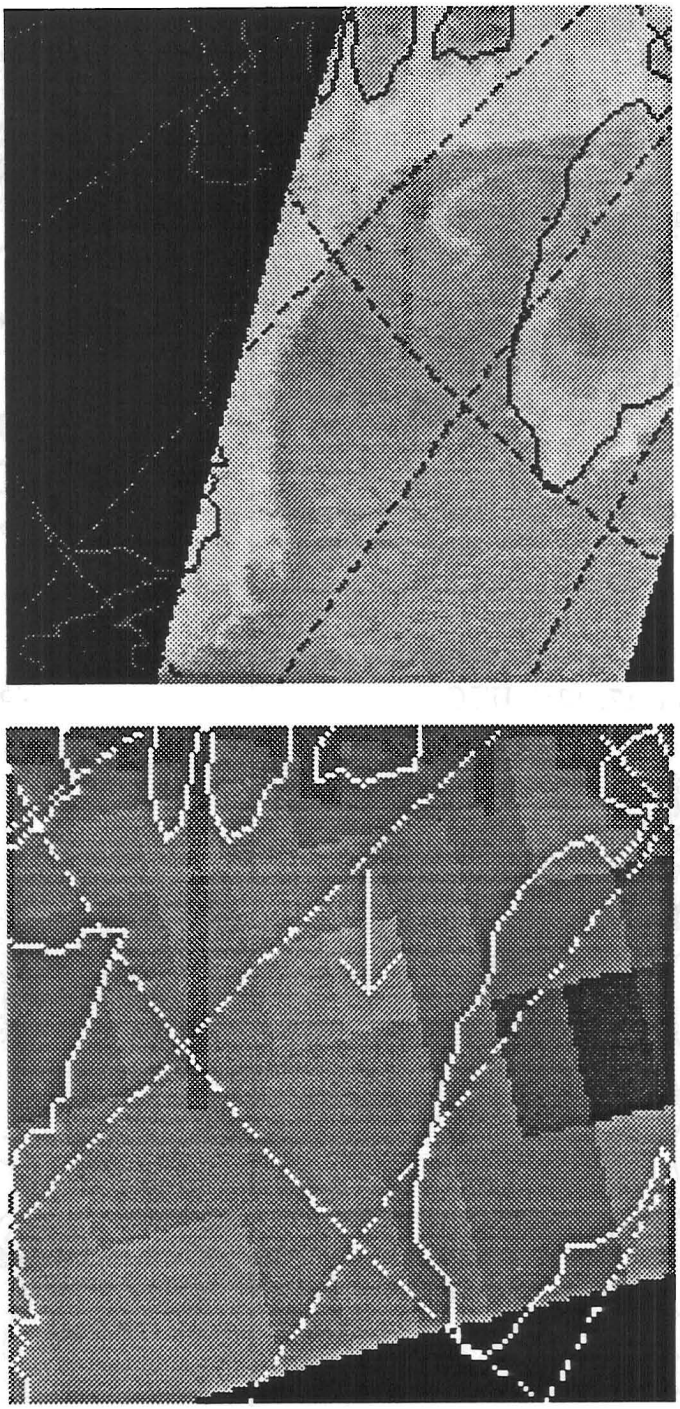

Figure 5.15: Top: SSM/I channel 7 imagery, Jan. 18, 1989 at 0829 UTC. Bottom: MSU 2 imagery Jan. 18, 1989 at 0720 UTC. The polar low center is shown by an arrow.

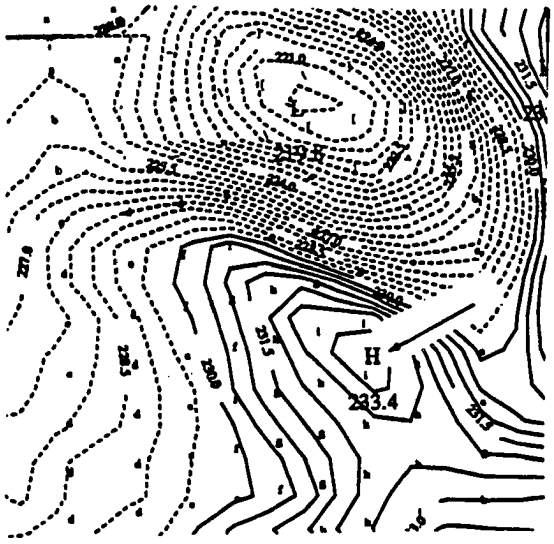

Jan. 17, 1312 UTC

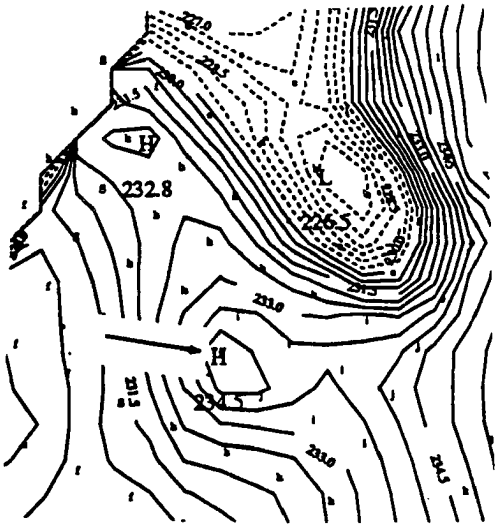

Jan. 17, 1545 UTC

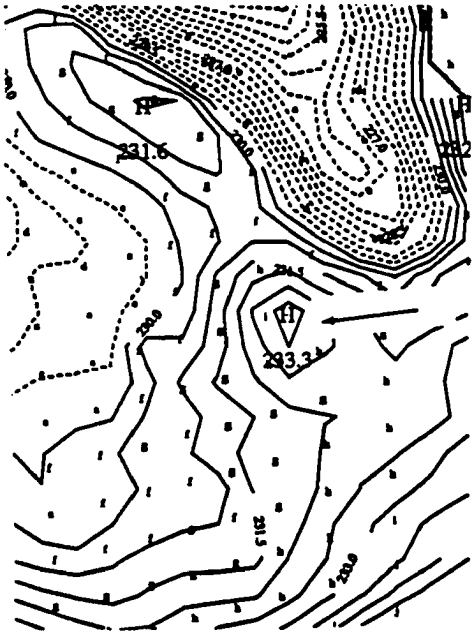

Jan. 18, 1250 UTC

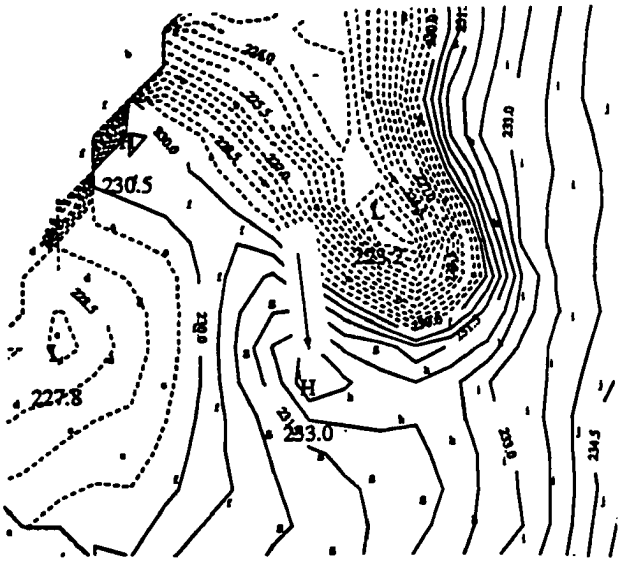

Jan. 18, 1535 UTC

Figure 5.16: MSU Channel 2 limb corrected brightness temperature for four times on January 17 - 18 over a slow moving polar low, indicated by the arrow. Note the persistence of the isolated warm core over the 24 hour time period.

5.2 Analysis of MSU 53.74 GHz Temperature Anomalies

There are several sources of error in the radial averaging of the MSU brightness temperatures to determine the warm anomaly of the polar low which are not as important in tropical cyclone applications. The first is that the polar low is usually found near an ice boundary, as opposed to the tropical cyclone which exists over open water. A source of error in using radial averaging around the polar low is that elevated land or ice masses may interfere with MSU channel 2. This fact is clearly demonstrated by cold brightness temperatures observed over Greenland. In this study, MSU observations over land were not used to compute the radially averaged temperature anomaly.

A second source of error in using radial averaging in polar regions is the presence of strong tropospheric temperature gradients. Strong brightness temperature gradients are apparent in Figure 5.13 near the polar low. This is a serious problem, since cold air outbreaks favor the occurrence of polar lows. Such cold air, if included in the radial temperature averaging, would lead to an overestimate of the warm temperature anomaly of the polar low.

Velden (1989) lists nine sources of error in applying satellite derived temperature anomalies to estimate tropical cyclone intensity. These sources of error also apply to polar low research and arise from the limited resolution of the instrument, variations in storm and environmental structure, and instrument noise.

The results for the warm temperature anomaly for the 1989 storms presented above are given in Table 5.1. Recall (see section 4.5.2) that Δ_{T1} is the difference in brightness temperature between the scan spot over the polar low and the averaged brightness temperature of the adjacent ring of up to 8 scan spots. Δ_{T1} is the difference in brightness temperature between the scan spot over the polar low and the averaged brightness temperature of the next most adjacent ring of up to 16 scan spots. The positive ΔT_1 and ΔT_2 figures indicate that radial averaging can

Δ_{T1}	Δ_{T2}	Time (UTC)	Satellite
0.5	1.0	Jan. 2, 1989 0639	*NOAA 11*
0.9	1.2	Jan. 2, 1989 1635	*NOAA 11*
0.8	0.6	Jan. 11, 1989 1203	*NOAA 10*
0.7	0.7	Jan. 11, 1989 2155	*NOAA 10*
1.5	2.8	Jan. 17, 1989 1312	*NOAA 10*
1.9	3.0	Jan. 17, 1989 1545	*NOAA 11*
1.4	—	Jan. 17, 1989 2122	*NOAA 10*
1.3	—	Jan. 18, 1989 0720	*NOAA 11*
1.4	2.5	Jan. 18, 1989 1250	*NOAA 10*
1.8	2.4	Jan. 18, 1989 1535	*NOAA 11*
0.3	0.4	Mar. 20, 1989 1207	*NOAA 10*

Table 5.1: MSU 2 brightness temperature anomalies. See text for details of computing Δ_{T1} and Δ_{T2}.

detect warm brightness temperatures over a polar low. The validity of the results is reinforced by the fact that the Microwave Sounding Units on the *NOAA 10* and *NOAA 11* satellites gave similar results. Note that all of the ΔT_2 values are positive, indicating a warm anomaly for each polar low. The ΔT_2 value was not determined for two of the cases because the outermost scan positions of the MSU would have had to be used. In the January 11 and March 20 cases, at least some of the warm anomaly is likely due to very cold air moving in from the north and west of the storms. Note that the ΔT_2 values are usually greater than the ΔT_1 values. There are at least two reasons for this. The first is that if a warm area of sufficient size did exist over a polar low, it could have been imaged in two or more scan spots so the ring around the storm center would have been biased too warm. A second reason is the presence of a brightness temperature gradient which is greater on the cold side of the storm than on the warm side. An example of this is shown in Figure 5.13.

The MSU 2 observations for the January 2 and January 17 - 18 storms each had a scan spot over them which was warmer than than any of the up to eight adjacent scan spots. Whether each storm had an adjacent scan spot warmer than the spot determined to be over the storm is indicated by a yes or no answer in Table 5.2 , with the next warmest adjacent value indicated for those cases with an

isolated warm spot. The warming of the sounding centered over the polar low as compared to adjacent soundings is quite striking, in most cases greater than the MSU instrument noise of 0.3 K.

Warmer scan spot adjacent ?	Difference of next warmest scene (K)	Time (UTC)	Satellite
NO	0.4	Jan. 2, 1989 0639	*NOAA 11*
NO	0.2	Jan. 2, 1989 1635	*NOAA 11*
YES	—	Jan. 11, 1989 1203	*NOAA 10*
YES	—	Jan. 11, 1989 2155	*NOAA 10*
NO	0.7	Jan. 17, 1989 1312	*NOAA 10*
NO	0.8	Jan. 17, 1989 1545	*NOAA 11*
NO	0.8	Jan. 17, 1989 2122	*NOAA 10*
NO	0.8	Jan. 18, 1989 0720	*NOAA 11*
NO	0.7	Jan. 18, 1989 1250	*NOAA 10*
NO	1.0	Jan. 18, 1989 1535	*NOAA 11*
YES	—	Mar. 20, 1989 1207	*NOAA 10*

Table 5.2: Listing of whether the MSU 2 scan spots over the polar lows had adjacent warmer scan spots. If so, the difference in K between the two warmest scan spots is indicated.

5.2.1 Possible Warming Effects on MSU Channel 2

A difficulty arises in using MSU measurements to determine warming in a polar low which is much less important when using the same instrument to observe tropical cyclones. This is the possible change in brightness temperature anomaly due to factors other than warming in the air column. Tropical cyclone studies with microwave sounding instruments use frequencies whose weighting functions peak in the upper troposphere, near the 250 mb peak amplitude in the storm versus environment temperature anomaly (Velden, 1983). This is fortunate since hydrometeors at these levels will be frozen and will have little effect on microwave radiances (Kidder *et al.*, (1978); Grody and Shen, (1982)). For polar lows, the level of maximum temperature anomaly has not been determined due to a shortage of *in situ* observations and the fact that polar lows have a range of structures. The polar low exists through a more shallow layer in the troposphere than the tropical cyclone. This fact was

confirmed in this study through examination of MSU 54.96 GHz imagery for the polar low cases , which showed much less structure than MSU 2 imagery. Regardless of the exact level of maximum temperature anomaly, the fact that polar lows are rather shallow necessitates the use of temperature sounding channels which peak deeper in the troposphere and are more sensitive to the effects of hydrometeors. The possibility of factors contributing to positive MSU 2 derived temperature anomalies over polar lows other than warming of the air column will now be considered.

Spencer *et al.* (1990) examined the sensitivity of MSU 2 to various geophysical parameters. Some of their results are listed in Table 5.3. They conclude that cumuliform clouds extending from 950 to 650 mb will have no effect on MSU 2, while clouds above about 650 mb will have a cooling effect. These sensitivities

Geophysical parameter	MSU 2 T_B sensitivity (K)
Oxygen emission by the atmosphere:	0.92° per +1° (land)
	0.96° per +1° (ocean)
Sea surface temperature	0.036° per +1°
Sea surface emissivity	0.01° per 1 m/s incr. in wind speed
Water vapor (ocean)	+0.02° per 20% in polar air mass
Cirrus clouds	0°(thin cirrus), −1° (thunderstorm)
Cloud water (ocean):	100% increase in coverage or amount
Low clouds (900-950mb)	+0.1° to +0.2°
Middle clouds (600-700mb)	−0.1°

Table 5.3: Sensitivity of MSU 2 to various geophysical parameters (after Spencer *et al.*, (1990)).

have been used to construct Table 5.4, which shows some possible upper bounds to warming observed in MSU 2. The doubling in water vapor content is assumed to be reasonable based on the measurements of Shapiro *et al.* (1987). It is likely that some of these effects are likely to be correlated, for instance over the ocean strong winds are likely to occur in a cloudy area in a storm. Table 5.5 shows that two of the polar lows, January 2, 1989 and January 17 - 18, 1989, still have a temperature anomaly after possible warming effects of 1.0 K are subtracted out. These are cases which had isolated warm cores (Table 5.2). For the cases studied here, cloud top heights

Parameter	Polar low vs. ambient	MSU 2 T_B increase (K)
Sea surface temperature	3 K higher	0.1
Sea surface emissivity	30 m/s higher	0.3
Water vapor	100% increase	0.1
Cloud liquid water	100% increase	0.2
Instrument noise		0.3
Total possible increase:		1.0

Table 5.4: Possible increases in MSU 2 brightness temperature over a polar low due to non - O_2 effects using the sensitivities in Table 5.3.

Time	Δ_{T2}	Δ_{T1}
Jan. 2, 1989 0639 UTC	0.0	-0.5
Jan. 2, 1989 1635 UTC	0.3	-0.9
Jan. 11, 1989 2155 UTC	-0.2	-0.3
Jan. 17, 1989 2122 UTC	1.8	0.4
Jan. 18, 1989 1250 UTC	1.5	0.4
Mar. 20, 1989 1207 UTC	-0.6	-0.7

Table 5.5: MSU 2 Δ_{T1} and Δ_{T2} temperature anomalies after subtracting the possible increases due to non - O_2 effects .

were not analyzed but it is likely that cloud tops extended at least to 650 mb, the level where clouds will cool MSU 2 (Spencer *et al.* (1990)), based on previous polar low studies (Rabbe, (1987); Turner *et al.*, (1992)).

Legleau (1989) modelled the effect of clouds at the Advanced Microwave Sounding Unit (AMSU) frequencies. Their results at 53.6 GHz, very close to the MSU 2 frequency , showed a maximum possible warming due to clouds over the ocean of +0.4 K. This is for a pure water cloud. When an ice cloud is considered, cooling of -0.3 K is found. Since the temperature anomalies listed in Table 5.1 are equal to or larger than this value, it appears that a portion of the warming observed in MSU 2 data is due to warmer temperatures in the polar low.

Westwater (1972) modelled the effects of clouds at several microwave frequencies, including 53.5 GHz. Results for a nadir view of a subarctic atmosphere with a surface emissivity of 0.5 and various cloud types are shown in Figure 5.17. The important feature to note from this modelling is that at frequencies above 50

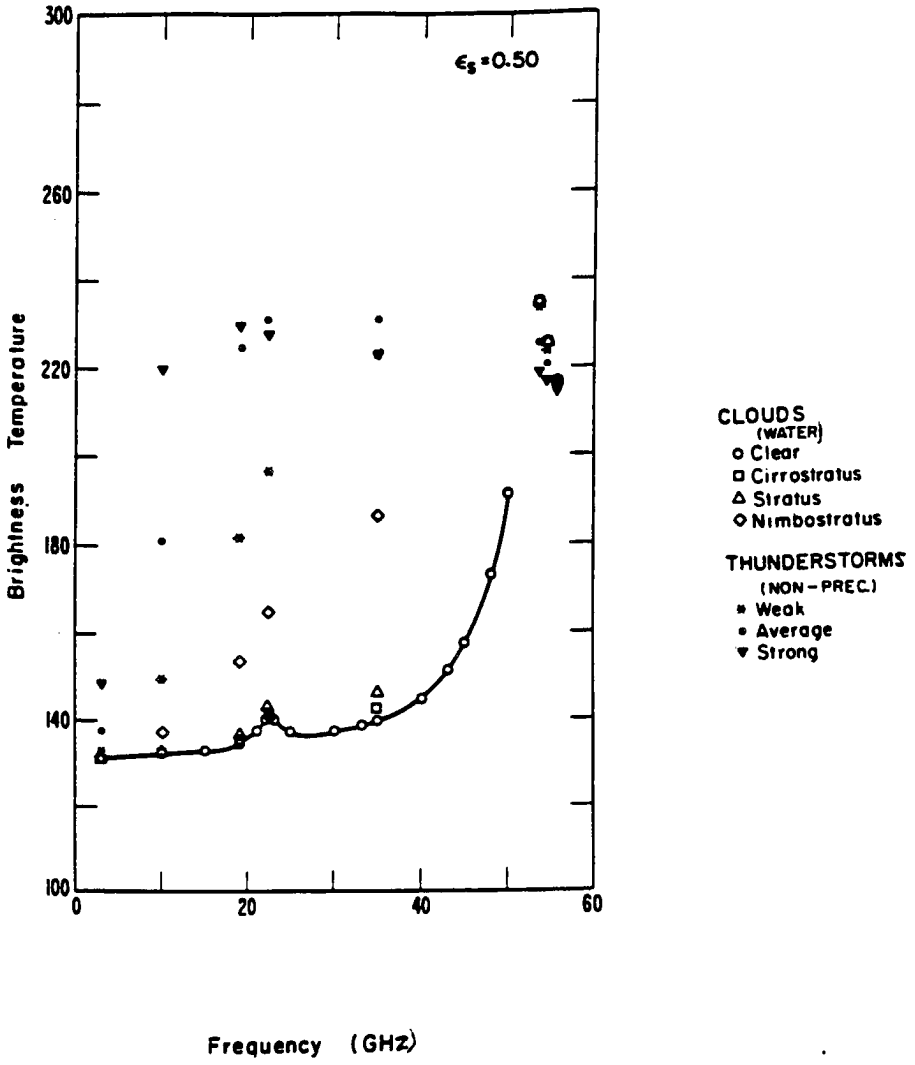

Figure 5.17: Nadir brightness temperature for several cloud models for a subarctic atmosphere. Note that clouds decrease the brightness temperatures at frequencies above 50 GHz (from Westwater, 1972).

GHz, clouds and thunderstorms have very little effect and what effect they have is to reduce brightness temperatures.

In work with the Special Sensor Microwave/Temperature Sounder (SSM/T), Fleming *et al.* (1991) examined the effects of clouds at several temperature sounding frequencies, including 53.20 GHz. They developed a parabolic fit of brightness temperature change caused by clouds as a function of integrated cloud liquid water. Brightness temperature increases of 0.8 K are possible for an integrated cloud liquid water amount of 0.2 mm. Claud *et al.* (1991) measured this liquid water content over a polar low using the SSM/I. This warming of 0.8 K at 53.20 GHz can be considered a strong upper bound to possible warming due to clouds because this frequency is more sensitive to cloud effects than the 53.74 GHz MSU channel.

An important point is that the radiative transfer studies mentioned do not include the resolution of the instrument. Precipitation areas are likely to exist on a smaller scale than the resolution of the MSU and this will minimize their effect on MSU measurements (Turner *et al.*, 1992).

The considerations given to the cause of the warm MSU scan spots over the polar lows indicate that while a portion of the warming can be attributed to non - air column warming, there remains for some cases warming which is attributed to temperature changes in the air column. The maximum warming which can be attributed to non-O_2 factors is about 1 K, but measured radially averaged temperature anomalies ranged up to 3 K.

5.3 Relationship Between Temperature Anomalies and Surface Wind Speed

Previous work which established a relationship between microwave measurements of warm cores and tropical cyclone intensity (see Section 1.2) had several advantages which polar low research does not have. Unlike tropical cyclones, polar lows are lacking in composites of storm structure and extensive *in situ* observations.

In an exploratory effort to look at these relationships for polar lows, the MSU temperature anomalies were compared to a parameter they are closely related to, storm pressure deficit.

The analytic model for hurricanes developed by Holland (1980) was used to indirectly infer the storm pressure deficit through SSM/I wind speed observations. Whether this model of the wind and pressure profiles for an axisymmetric vortex is applicable to polar lows has not been thoroughly investigated but has been suggested (Van Delden, 1989b). With sufficient radial observations of wind speed or pressure, the model can be optimally solved for the two curve fitting parameters it requires (*e.g.* Weatherford, 1987). Wind and pressure profiles as well as the radius of maximum winds and maximum wind speed can then be derived from the model. The resolution of SSM/I derived wind speeds as compared to the size of a polar low do not yield enough observations to optimally solve for curve fitting parameters, so a value was chosen for one of the parameters and the other was determined through the wind speed observations.

A parameter in the model, hereafter referred to as 'B', ranges from 1.0 to 2.5 for tropical cyclones (Holland, 1980). Increasing the value of B causes more of the pressure drop to occur near the radius of maximum winds, leading to an increase in maximum wind speed. In order to see if the same range of B applies to polar lows, B was determined for previous polar lows which had measurements of maximum wind speeds and pressure deficit. This was performed through the relation (Holland, 1980)

$$B = \frac{V_m{}^2 \Delta_P}{2.718\, \rho_{air}} \tag{5.1}$$

where ρ_{air} is the air density at sea level (set equal to 1.15 kg/m^2), V_m is the maximum wind speed, and Δ_P is the storm pressure deficit. Results of this calculation for four well documented polar lows are given in Table 5.6. It can be seen that the values lie in the 1.0 to 2.5 range given by Holland (1980) for tropical cyclones. This indicates

Polar Low	Calculated Value of B
Rasmussen (1985)	1.20
Shapiro *et al.* (1987)	1.80
Businger and Baik (1991)	1.63
Nordeng and Rasmussen (1992)	1.53

Mean:	1.54

Table 5.6: Values of Holland's parameter B determined for four polar lows with sufficient observations. Range of B for tropical cyclones is 1.0 to 2.5.

that the model may be applicable to polar lows. The sensitivity of storm pressure deficit to the value of B is shown in Figure 5.18 for four maximum wind speeds. Errors in determining the pressure deficit with different values of B increase as the maximum wind speed of the storm increases, with errors of up to 15 mb for a 30 m/s maximum wind speed.

In order to compute storm pressure deficit through the use of radially averaged SSM/I wind speeds, a value of 1.5 for the parameter B was chosen for all cases. This value was chosen since it lies near the mean shown in Table 5.6.

With a value of 1.5 for B chosen, the pressure deficit for the four cases listed was determined through the use of the gradient wind equation in Holland (1980). A set of six SSM/I wind speed determinations was used. Wind speeds derived from the SSM/I were input for two radii from the storm center, which were variable depending on the amount of precipitation flagging around the polar low. The minimum radii used was 88 km and the maximum was 187 km.

An example of the type of wind profile which is generated with the model is shown in Figure 5.19. This profile for the polar low which occurred at January 18, 1989 at 0829 UTC was generated from two radially averaged SSM/I wind speed observations at 110 and 165 km distance from the storm center.

A plot of pressure deficit as deduced from the SSM/I versus ΔT_2 is given in Figure 5.20. A linear regression of the data was performed with a poor correlation coefficient of 0.37. This is not surprising in view of the many sources of error in the calculation. Undoubtedly choosing one value of B is a source of error, the

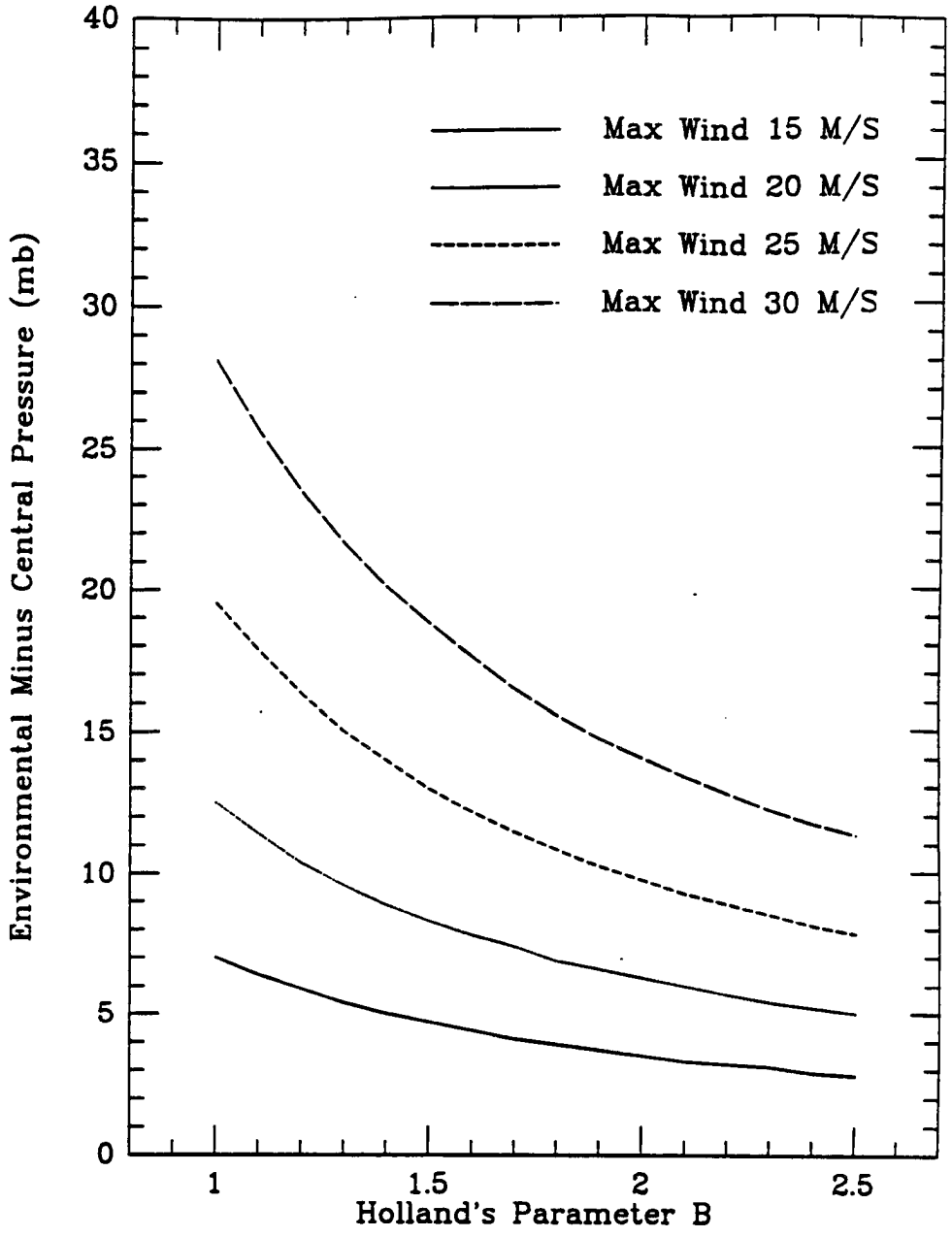

Figure 5.18: Storm pressure deficit for four maximum wind speeds as a function of the parameter B.

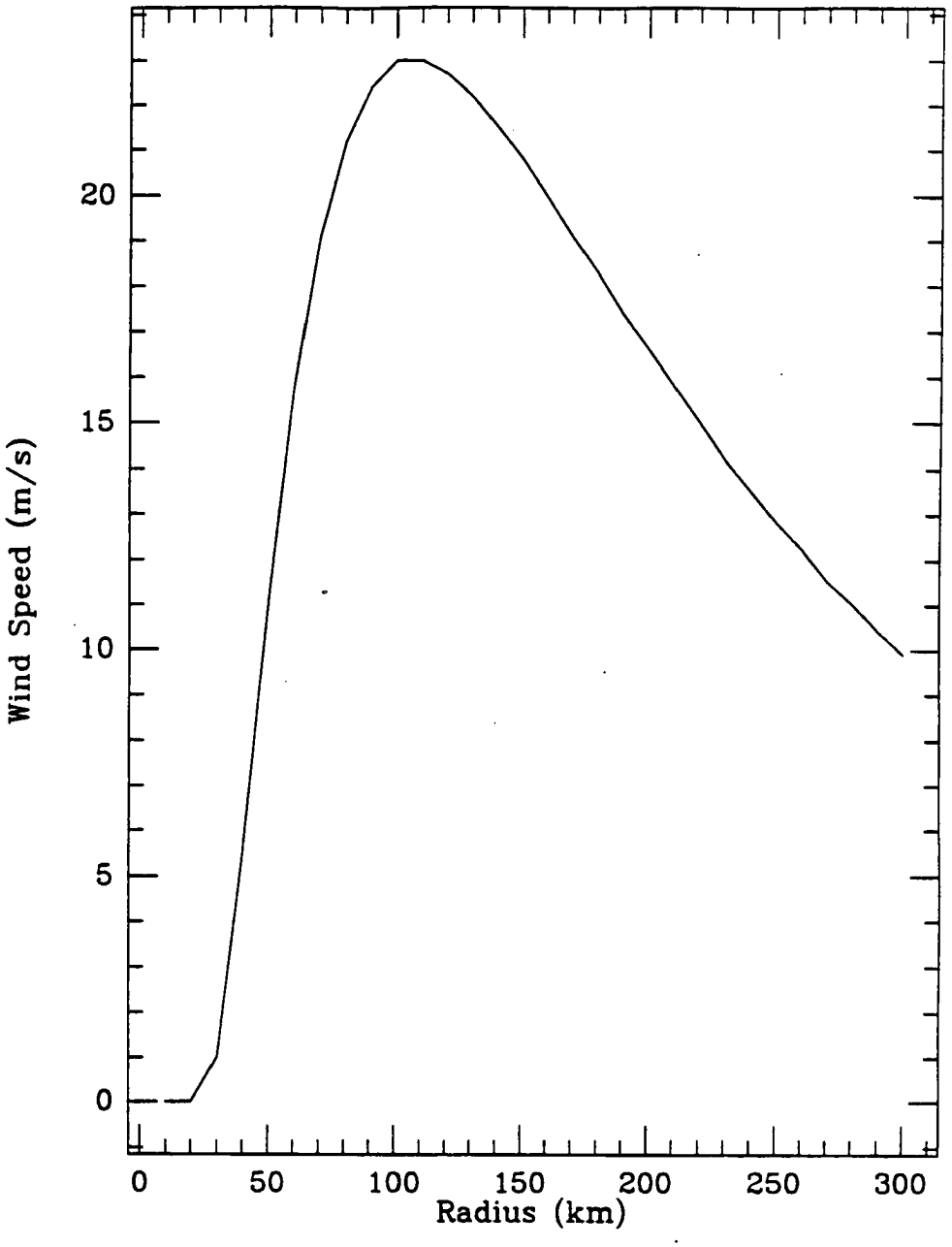

Figure 5.19: Wind speed profile from the model for January 18, 1989 at 0829 UTC. SSM/I wind speeds were input in order to interpolate into the storm center.

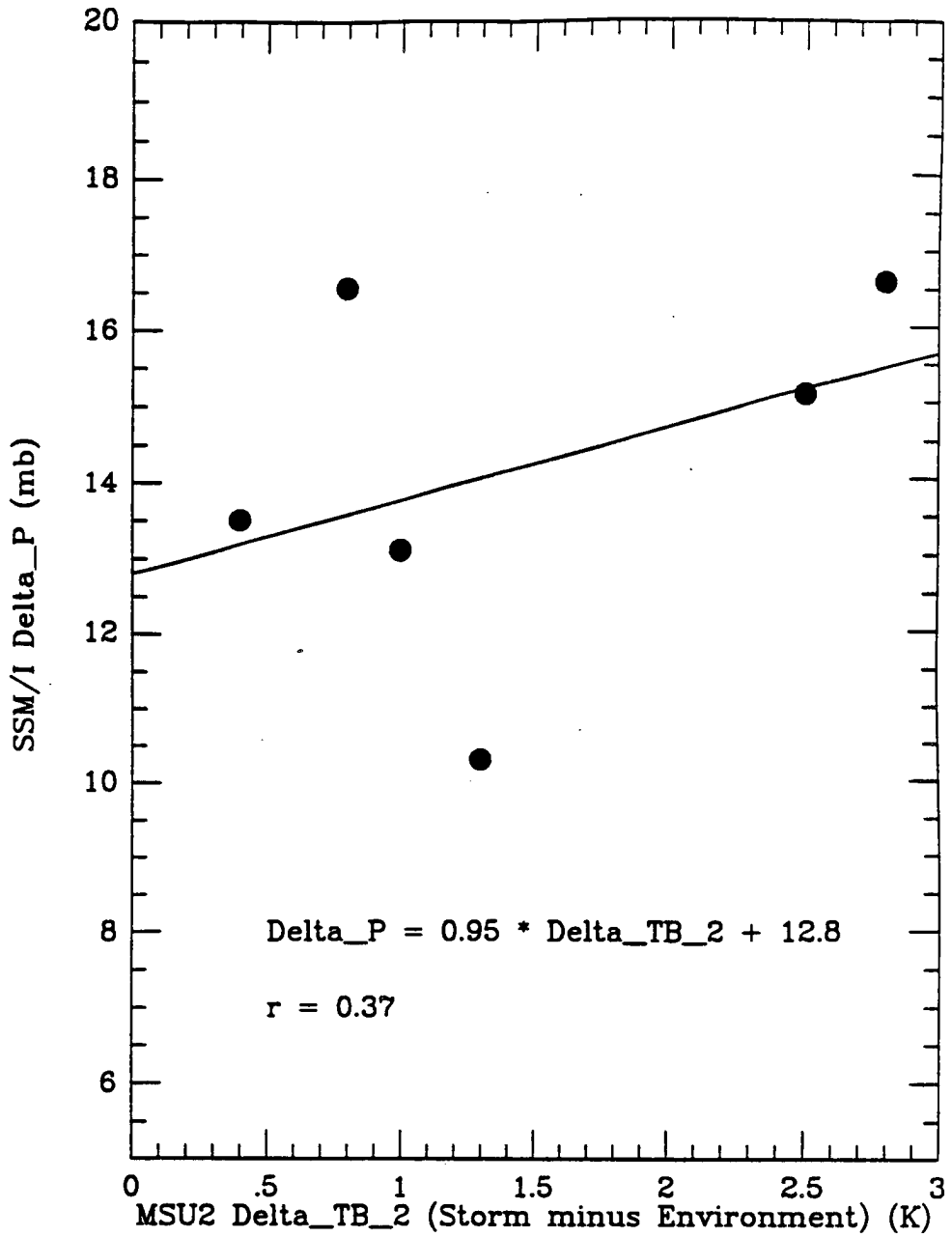

Figure 5.20: Storm pressure deficit from SSM/I wind speeds versus MSU ΔT_2. A linear regression of the values is also shown.

magnitude of which can be estimated from Figure 5.18, although the maximum wind speed of the storm is unknown. Other sources of error include the validity of the axisymmetric assumption, noise and biases in the wind speed values, and the fact that SSM/I wind speeds are referenced to a 19.5 m height while the determination of pressure deficit requires the input of a gradient wind speed.

Another source of error which may arise in estimating storm central pressure from wind speed observations at outer radii is mentioned in Weatherford and Gray (1988) for tropical cyclones. This is the finding that outer core strength and central pressure may be unrelated. Polar low case studies (Rasmussen and Lystad, 1986; Rasmussen *et al.*, 1992) have suggested that a polar low can have a small scale inner core inside a broader circulation. This points to a difficulty in using wind speeds from the SSM/I to estimate the intensity of a polar low. The resolution of the SSM/I only allows wind speed at outer radii to be estimated. If decoupling of the inner and outer circulation of a polar low occurs, then intensity estimates based on outer radii wind speeds could be misleading. Perhaps microwave temperature sounding at a higher spatial resolution than available for this study could be used to estimate the intensity of the inner portion of a polar low. Such measurements will be available when the Advanced Microwave Sounding Unit is launched in the mid 1990's. This could then be used with outer radii wind speeds for a two parameter estimate of storm intensity.

5.4 Comparison of Cases

Considering the cases with isolated warm cores (all adjacent scan spots of lower brightness temperature) in MSU 2 versus those without isolated warm cores, several interesting observations can be made. The first is that the cases with isolated warm cores, January 2, 1989 and January 17 - 18, 1989, consist of spiraliform cloud signatures versus the comma clouds of January 11, 1989 and March 20, 1989. A relationship has been noted based on limited surface observations between the

amount cloud bands wrap around the center of a polar low and the pressure deficit of the storm (Forbes and Lottes, 1985), with greater pressure deficits for a more spiraliform appearance. Such behavior has also been noted for oceanic cyclones (Junker and Haller, 1980). Since a pressure deficit should be associated with the measured temperature anomalies hydrostatically, the warm cores found in these cases add indirect support to this finding.

Another difference between the spiraliform and non-spiraliform cases is involves their appearance on 85 GHz horizontally polarized imagery. The spiraliform storms had a distinct appearance on this imagery (for example, see Figure 5.15) while the comma shaped storms were barely detectable. The cloud bands indicated in this imagery are indicative of plentiful liquid water in the clouds. Unfortunately, the 85 GHz vertically polarized channel of the SSM/I, which would have allowed a more quantitative estimate of cloud water, was not functioning in 1989. This liquid water could be responsible for some of the warming observed in MSU 2 but it could also indicate deep precipitating convection. The formation of a warm core through the CISK process and associated deep precipitating convection was discussed in Section 2.5.

The isolated warming detected in MSU data over two of the four polar low cases does not reveal the mechanism responsible for the warming. This could include some combination of the mechanisms discussed in Chapter 2. In the January 17 - 18 case, the presence of the isolated warming 500 km distant from areas of the same brightness temperature suggests that the warming is occurring *in situ*. This would seem to rule out the seclusion process in this case. The microwave measurements from this study are unable to determine the cause for the observed warming.

Chapter 6

SUMMARY AND CONCLUSIONS

In this study, passive satellite microwave measurements of four polar lows from 1989 have been shown to be quite useful for determining several characteristics of these storms. Satellite derived surface wind speeds from the SSM/I and brightness temperature anomalies from MSU channel 2 were examined. These instruments have been used to estimate the intensity of tropical cyclones. This exploratory study reveals that polar lows are also candidates for these types of analysis techniques. There are advantages and disadvantages in using microwave techniques to analyze polar lows as compared to tropical cyclones. An advantages is low interference from liquid water in the polar regions. Disadvantages include much less knowledge about polar low structure, more ambiguity in interpreting warm core temperature anomalies, and a lack of observations to validate the measurements. Satellite observations will no doubt continue to play a vital role in polar low research due to the lack of other data sources in the polar low regions.

The main new finding from this study is that the low resolution measurements of the MSU can detect an isolated warm core over some polar lows. Possible warming effects at 53.74 GHz from clouds and precipitation were considered. Based on previous modelling work, the maximum warming from these effects was tentatively determined to be about 1 K. Radially averaged brightness temperature anomalies ranged up to 3 K. This indicates that for some polar lows warming of the tropospheric air column occurs. The warm cores were most pronounced in polar lows which exhibited significant convection and a spiral cloud shield, in accordance with

theory. The detection of such a warm core after sources of error are removed could possible provide a means to estimate polar low pressure deficit and maximum wind speeds. Crude methods exist to estimate polar low pressure deficit from infrared satellite imagery (Forbes and Lottes, 1985), but a method based on measurements of the warm core of the storm would be a valuable addition.

Surface wind speeds from SSM/I measurements revealed the presence of a circulation around each storm, often without great precipitation interference. This is important since a cloud feature which resembles a polar lows may not have any associated circulation. The SSM/I wind speeds could be a valuable tool for a forecaster faced with a suspicious cloud feature in a data free region. Microwave measurements of surface wind speed around polar lows are especially useful due to low liquid water contents in the polar regions, leading to reduced areas of accuracy flagging.

An attempt was made to relate temperature anomalies to the inferred central pressure of several polar lows. An analytic model for pressure and wind profiles which was developed for tropical cyclones was shown to be applicable to polar lows. This model was used to infer storm central pressure based on wind speed measurements. The relationship between measured temperature and computed pressure anomalies was poor. Perhaps *in situ* measurements of central pressure are needed to better examine this relationship. There is also some doubt as to whether outer winds are related to features in the inner portion of the polar low. Further complications in developing a relationship between outer wind speeds and storm pressure deficit arise due to strong background flow and lack of symmetry of the polar low.

Polar lows are a fairly recent discovery in the atmosphere and there is great potential for further work. Polar low research lags far behind tropical cyclone research in terms of observations of the storms and composite studies from observations within the storm. This type of data is crucial to the development of satellite remote sensing techniques in two ways. The first is to validate remotely sensed

parameters. The second is to provide data for modelling of these storms. Kidder *et al.* (1980) were able to determine a relationship between satellite measured temperature anomalies and surface pressure deficits through considering the composite temperature structure of a tropical cyclone. Such work is not currently possible for polar lows. Measurements of cloud properties of polar lows could be used to assess their effect on satellite temperature soundings.

Polar low research will also benefit from improvements in satellite technology. In particular, the Advanced Microwave Sounding Unit, scheduled for launch in the mid - 1990's, will have improvements in horizontal resolution and number of channels as compared to the MSU. Several sounding channels could be used in a retrieval scheme to better define the existence of a warm core in polar lows. Such a scheme could also minimize cloud and precipitation effects on storm temperature anomaly determination. A satellite in Molniya orbit (Kidder and Vonder Haar, 1990), which allows good coverage of the polar regions, would allow much better coverage of the polar regions.

In summary, this study has shown that present satellite microwave instruments can detect warm cores in some polar lows and also define the outer wind field of these storms. Much work remains to be done to quantify the relationship between satellite measurements and physical parameters in polar lows. This type of work will lead to better understanding, analysis and prediction of these storms of the polar regions.

REFERENCES

Anthes, R. A., 1982: *Tropical Cyclones. Their Evolution, Structure, and Effects.* Amer. Met. Soc. Boston, Massachusetts, 208 pp.

Bond, N.A., and M.A. Shapiro, 1991: Polar lows over the Gulf of Alaska in conditions of reverse shear. *Mon. Wea. Rev.*, **119**, 551-572.

Businger, S., 1985: The synoptic climatology of polar low outbreaks. *Tellus*, **37A**, 419-432.

Businger, S., and P.V. Hobbs, 1987: Mesoscale structures of two comma cloud systems over the Pacific Ocean. *Mon. Wea. Rev.*, **115**, 1908-1928.

Businger, S., and B. Walter, 1988: Comma cloud development and associated rapid rapid cyclogenesis over the Gulf of Alaska: A case study using aircraft and operational data. *Mon. Wea. Rev.*, **116**, 1103-1123.

Businger, S., and R.J. Reed, 1989a: Cyclogenesis in cold air masses. *Wea. Forecasting.*, **4**, 133-156.

Businger, S., and R.J. Reed, 1989b: Polar lows. In P.F. Twitchell, E.A. Rasmussen and K.L. Davidson (Eds.), *Polar and Arctic Lows.* A. Deepak Publishing, Hampton, Virginia, 3-45.

Businger, S., and J.-J. Baik, 1991: An arctic hurricane over the Bering Sea. *Mon. Wea. Rev.*, **119**, 2293-2322.

Carleton, A.M., and D.A. Carpenter, 1989: Satellite climatology of "polar air vortices" for the Southern Hemisphere winter. In P.F. Twitchell, E.A. Rasmussen and K.L. Davidson (Eds.), *Polar and Arctic Lows.* A. Deepak Publishing, Hampton, Virginia, 401-413.

Chenggang, Y., and A. Timchalk, 1988: Precipitation detection with satellite microwave data. *NOAA Tech. Memo.* NESDIS 32, 27 pp.

Claud, C., N.M. Mognard, K.B. Katsaros, A. Chedin, and N.A. Scott, 1991: Satellite observations of polar lows by SSM/I, GEOSAT, and TOVS. *International Geoscience and Remote Sensing Symposium.* Helsinki, Finland.

Claud, C., K.B. Katsaros, G.W. Petty, A. Chedin, and N.A. Scott, 1992a: A cold air outbreak over the Norwegian Sea observed with the TIROS-N Operational Vertical Sounder (TOVS) and the Special Sensor Microwave/Imager (SSM/). *Tellus*, **44A**, 100-118.

Claud, C, N.A. Scott, and A. Chedin, 1992b: Use of TOVS observations for the study of polar and arctic lows. *Intl. J. Remote Sensing*, **13**, 129-139.

Cox, C., and W. Munk, 1954: Measurements of the roughness of the sea surface from photographs of the sun's glitter. *J. Opt. Soc. Amer.*, **44**, 838-850.

Craig, G., and H.-R. Cho, 1989: Baroclinic instability and CISK as the driving mechanisms for polar lows and comma clouds. In P.F. Twitchell, E.A. Rasmussen and K.L. Davidson (Eds.), *Polar and Arctic Lows.* A. Deepak Publishing, Hampton, Virginia, 131-140.

Craig, J., and H.-R. Cho, 1988: Cumulus convection and CISK in the extratropical atmosphere, Part I: Polar lows and comma clouds. *J. Atmos. Sci.*, **45**, 2622-2640.

Douglas, M.W., and M.A. Shapiro, 1989: A comparison of the structure of two polar lows observed by research aircraft. In P.F. Twitchell, E.A. Rasmussen and K.L. Davidson (Eds.), *Polar and Arctic Lows.* A. Deepak Publishing, Hampton, Virginia, 291-312.

Douglas, M.W., M.A. Shapiro, L.S. Fedor, and L. Saukkonen, 1990: Research aircraft observations of a polar low at the East-Greenland ice-edge. Extended Abstracts, *Fourth Conf. on Mesoscale Processes*, Boulder, Colorado. Amer. Meteor. Soc., Boston, 22-23.

Douglas, M.W., L.S. Fedor, and M.A. Shapiro, 1991: Polar low structure over the Northern Gulf of Alaska based on research aircraft observations. *Mon. Wea. Rev.*, **119**, 32-54.

Elachi, C., 1987: *Introduction to the Physics and Techniques of Remote Sensing.* John Wiley and Sons, Inc., New York, 413 pp.

Emanuel, K.A., and R. Rotunno, 1989: Polar lows as arctic hurricanes. *Tellus*, **41A**, 1-17.

Fitch, M., and A.M. Carleton, 1992: Antarctic mesocyclone regimes from satellite and conventional data. *Tellus.*, **44A**, 180-196.

Fleming, H.E., Grody, N.C., and E.J. Kratz, 1991: The forward problem and corrections for the SSM/T satellite microwave temperature sounder. *IEEE Trans. Geosci. and Remote Sensing.*, **29**, 571-583.

Forbes, G.S, and W.D. Lottes, 1985: Classification of mesoscale vortices in polar airstreams and the influence of the large-scale environment on their evolutions. *Tellus*, **37A**, 132-155.

Glazman, R.E., 1991: Statistical problems of wind-generated gravity waves arising in microwave remote sensing of surface winds. *IEEE Trans. Geosci. and Remote Sensing.*, **29**, 135-142.

Gloersen, P., and E. Mollo-Christensen, 1989: Observations of Arctic polar lows with the Nimbus-7 Scanning Multichannel Microwave Radiometer. In P.F. Twitchell, E.A. Rasmussen and K.L. Davidson (Eds.), *Polar and Arctic Lows.* A. Deepak Publishing, Hampton, Virginia, 359-371.

Goodberlet, M.A., C.T. Swift, and J.C Wilkerson, 1989: Remote sensing of ocean surface winds with the Special Sensor Microwave/ Imager. *J. Geophys. Res.*, **94**, 14547-14555.

Grody, N.C., 1976: Remote sensing of atmospheric water content from satellites using microwave radiometry. *IEEE Trans. Antennas and Propag.*, **AP-24**, 155-162.

Grody, N.C., C.M. Hayden, W.C.C. Shen, P.W. Rosenkranz, and D.H. Staelin, 1979: Typhoon June winds estimated from Scanning Microwave Spectrometer measurements at 55.45 GHz. *J. Geophys. Res.*, **84**, 3689-3695.

Grody, N.C., and W.C. Shen, 1982: Observations of Hurricane David (1979) using the Microwave Sounding Unit. *NOAA Tech. Rep.* NESS 88, 52 pp.

Grody, N.C., 1983: Severe storm observations using the Microwave Sounding Unit. *J. Climate and Applied Meteor.*, **22**, 609-625.

Guissard, A., and P. Sobieski, 1987: An approximate model for the microwave brightness temperature of the sea. *Intl. J. Remote Sensing*, **8**, 1607-1627.

Harrold, T.W., and K.A. Browning, 1969: The polar low as a baroclinic disturbance. *Quart. J. Roy. Met. Soc.*, **95**, 710-723.

Holland, G.J., 1980: An analytic model of the wind and pressure profiles in hurricanes. *Mon. Wea. Rev.*, **108**, 1212-1218.

Holliday, C.R., and K.H. North, 1992: SSM/I gale wind intercomparisons with ship and buoy observations. Preprints, *Sixth Conf. on Satellite Meteorology and Oceanography*, Atlanta, Georgia. Amer. Meteor. Soc., Boston, Mass. 212-214.

Hollinger, J.P., 1971: Passive microwave measurements of sea surface roughness. *IEEE Trans. Geosci. Electron.*, **GE-9**, 165-169.

Hollinger, J. (ed.), 1989: *DMSP Special Sensor Microwave/Imager Calibration / Validation, Vol I.* Naval Research Laboratory, Washington, D.C., 175 pp.

Hollinger, J. (ed.), 1991: *DMSP Special Sensor Microwave/Imager Calibration / Validation, Vol II.* Naval Research Laboratory, Washington, D.C., 277 pp.

Jones, A.S., and T.H. Vonder Haar, 1989: Microwave remote sensing of cloud liquid water and surface emittance over land regions. Cooperative Institute for Research in the Atmosphere, Colorado State University, Fort Collins, Colo.

Jones, A.S., and T.H. Vonder Haar, 1992: PORTAL - A satellite remap/fusion system Preprints, *Sixth Conf. on Satellite Meteorology and Oceanography*, Atlanta, Georgia. Amer. Meteor. Soc., Boston, J98-J101.

Junker N.W., and D.J. Haller ,1980: Estimation of surface pressures by satellite cloud pattern recognition. Preprints, *Eight Conf. on Wea. Forecasting and Analysis*, Denver, Colorado. Amer. Meteor. Soc., Boston, 119-122.

Kidder, S.Q., W.M. Gray, and T.H. Vonder Haar, 1978: Estimating tropical cyclone central pressure and outer winds from satellite microwave data. *Mon. Wea. Rev.*, **106**, 1458-1464.

Kidder, S.Q., W.M. Gray, and T.H. Vonder Haar, 1980: Tropical cyclone outer winds derived from satellite microwave sounder data. *Mon. Wea. Rev.*, **108**, 144-152.

Kidder, S.Q., and T.H. Vonder Haar, 1990: On the use of satellites in Molniya orbits for meteorological observations of middle and high latitudes. *J. Atmos. and Oceanic Tech.*, **7**, 517-522.

Kidwell, K.B. (ed.), 1988: NOAA Polar Orbiter Data Users Guide. . *National Environmental Satellite, Data, and Information Service*, Washington, D.C. 178 pp.

Koehler, T.L., 1989: Limb correction effects on TIROS-N Microwave Sounding Unit observations. *J. Applied. Meteor.*, **28**, 807-817.

Kuo,Y.-H., R.J. Reed, and S. Low-Nam, 1991: Effects of surface energy fluxes during the early development and rapid intensification stages of seven explosive cyclones in the Western Atlantic. *Mon. Wea. Rev.*,**119**, 457-475.

Kuo,Y.-H., R.J. Reed, and S. Low-Nam, 1992: Thermal structure and airflow in a model simulation of an occluded marine cyclone. *Mon. Wea. Rev.*, **120**, 2280-2297.

Legleau, H., 1989: Simulation of the effect of a realistic cloud field on the AMSU measurements. In A. Chedin (ed.) *Microwave Remote Sensing of the Earth System.* A. Deepak Publishing, Hampton, Virginia, 33-49.

Liebe, H.J., G.G. Gimmestad, and J.D. Hopponen, 1977: Atmospheric oxygen microwave spectrum - experiment versus theory. *IEEE Trans. Antennas and Propag.*, **AP-25**, 327-335.

Midtbø, K.H., 1986: Polar low forecasting. In *Proceedings of the International Conference on Polar Lows.* The Norwegian Meteorological Institute. Oslo, Norway, pp. 257-271.

Milman, A.S., 1987: How wind affects passive microwave measurements of sea surface temperature. *IEEE Trans. Geosci. and Remote Sensing.*, **GE-25**, 22-27.

Mognard, N.M., and K.B. Katsaros, 1992: Comparison of wind speed measurements over the oceans with the Special Sensor Microwave/Imager and the GEOSAT altimeter. Preprints, *Sixth Conf. on Satellite Meteorology and Oceanography*, Atlanta, Georgia. Amer. Meteor. Soc., Boston, 406-410.

Monaghan, E.C., and I. Ó Muircheartaigh, 1980: Optimal power law description of oceanic whitecap coverage dependence on wind speed. *J. Phys. Oceanogr.*, **10**, 2094-2099.

Moore, R.K., Y.S. Yu, A.K. Fung, D. Kaneko, G.J. Dome, and R.E. Werp, 1979: Preliminary study of rain effects on radar scattering from water surfaces. *IEEE J. Oceanic Engineering*, **OE-4**, 31-32.

Nordberg, W., J. Conaway, D.B. Ross, and T. Wilheit, 1971: Measurements of microwave emission from a foam-covered, wind-driven sea. *J. Atmos. Sci.*, **28**, 429-435.

Nordeng, T.E., and E.A. Rasmussen, 1992: A most beautiful polar low. A case study of a polar low in the Bear Island region. *Tellus*, **44A**, 81-99.

Økland, H., 1987: Heating by organized convection as a source of polar low intensification. *Tellus*, **39A**, 397-407.

Økland, H., and H. Schyberg, 1987: On the contrasting influence of organized moist convection and surface heat flux on a barotropic vortex. *Tellus*, **39A**, 385-389.

Økland, H., 1989: Genesis of polar lows. In P.F. Twitchell, E.A. Rasmussen and K.L. Davidson (Eds.), *Polar and Arctic Lows.* A. Deepak Publishing, Hampton, Virginia, 179-190.

Olson, W.S., 1987: Estimation of rainfall rates in tropical cyclones by passive microwave radiometry Ph.D. Dissertation. University of Wisconsin-Madison. Madison, Wisconsin.

Parker, N., and E. Hudson, 1991: *Polar Low Handbook for Canadian Meteorologists.* Atmospheric Environment Service, Edmonton, Alberta, Canada, 173 pp.

Petty, G.W., 1990: Observing the marine atmosphere with the Special Sensor Microwave Imager. Ph.D. Dissertation. University of Washington. Seattle, Washington.

Petty, G.W., and K.B. Katsaros, 1990: New geophysical algorithms for the Special Sensor Microwave Imager. Preprints, *Fifth Conf. on Satellite Meteorology and Oceanography*, London, England. Amer. Meteor. Soc., Boston, Mass. 247-251.